

THESIS



This is to certify that the

dissertation entitled

"Rare Gas Atoms and Clusters of Atoms
Inside Microporous Solids"

presented by

BOYONG CHEN

has been accepted towards fulfillment
of the requirements for

Ph.D. degree in Physics

Major professor
S.D. Mahanti

Date 5/22/96

LIBRARY
Michigan State
University

PLACE IN RETURN BOX to remove this checkout from your record.
TO AVOID FINES return on or before date due.

DATE DUE DATE DUE DATE DUE		
<u>OCT 28 1999</u>	_____	_____
_____	_____	_____
_____	_____	_____
_____	_____	_____
_____	_____	_____
_____	_____	_____
_____	_____	_____

RARE GAS ATOMS AND CLUSTER OF
ATOMS INSIDE MICROPOROUS SOLIDS

By

Boyong Chen

A DISSERTATION

Submitted to
Michigan State University
in partial fulfillment of the requirements
for the Degree of

DOCTOR OF PHILOSOPHY

Department of Physics and Astronomy

1996

ABSTRACT

Rare Gas Atoms and Cluster of Atoms Inside Microporous Solids

By

Boyong Chen

Physical properties of both quantum and classical rare gas atoms and cluster of atoms confined inside microporous solids have been studied in this thesis.

In microporous media characterized by pore size in the range $5 \sim 15 \text{ \AA}$, mass transport of *He* atoms at low temperatures is quantum mechanical in nature. By solving the one-particle Schrödinger equation, we investigate the effective mass m^*/m of *He* atoms (bare mass m) moving inside one-dimensional tubular channels consisting of cylindrical cages connected by necks of different diameters and lengths. We find that m/m^* is a highly nonlinear function of the geometrical parameters characterizing these channels. We also find that in the presence of an attractive potential produced by positive ions located on the channel wall, the atoms are trapped near the wall, resulting in a drastic reduction in m/m^* .

Low lying excitations of ^4He and ^3He atoms confined inside zeolite cages have been modelled by Bose-Hubbard and Mott-Hubbard rings with strong intrasite repulsion and finite intersite attraction. Calculated temperature and concentration dependence of the heat capacities agree well with the experiment except at very low temperatures. We argue that the discrepancy with experiment is due

to the disorder effects which exist in the system. After the inclusion of the effect of tunnelling disorder, we obtained theoretical results which in much better agreement with experiment. results.

Thermal properties and dynamic properties of Xe_{6c} cluster and Xe_{6CAM} – a cluster assembled material confined inside L-zeolite cages have been investigated using extensive Monte Carlo (MC) and molecular dynamics simulations. By monitoring the temperature (T) dependence of the average energy $\langle E \rangle$ and the bond length fluctuation (δ), we find that unlike a free Xe_6 cluster which starts to ‘melt’ at a reasonably well defined T, the confined Xe_{6c} cluster for similar lengths of MC runs shows a series of ‘melting’ temperatures. However, the average of many long MC runs gives a relatively smooth variation of $\langle E \rangle$ and δ with temperature. One can still identify a ‘melting’ transition but at a much higher temperature than that seen in the free cluster. On the other hand, Xe_{6CAM} system shows a well defined ‘melting’ transition. The molecular dynamics simulation demonstrates that Xe_{6CAM} has a much more stable structure than Xe_{6c} .

The percolation properties of *Ar* and *He* atoms in the mixed ion pillared layered silicate clay systems $[Cr(en)_3^{3+}]_x[Co(en)_2^{3+} - (en)]_{1-x}$ - fluorohectorite(*FHT*), where (*en*) is an ethylenediamine ligand, at room temperatures have been investigated using continuum MC simulation method. We find that the adsorptive and diffusive properties depend sensitively on the size of the diffusing species and the concentrations x and $(1 - x)$ of the intercalants. *Ar* adsorption studies in the above *FHT* system shows a percolative response when x reaches 0.79. Using simple geometrical models to describe these microporus media, along with computer simulation, we can understand the $x = 0.79$ percolation threshold.

ACKNOWLEDGEMENTS

I would like to express my sincere thanks to my thesis advisor Professor S. D. Mahanti for his careful and patient guidance. Without his constant support, understanding, encouragement, and physical insights, this work would not have been possible.

I also would like to thank Dr. M. Yussouff for his cooperation, helpful discussions and suggestions and his patience and concern. I thank Dr. Bhattacharya Aniket for allowing me to cooperate with him. I learned a lot from his work. I am also grateful to Professor M. F. Thorpe for his valuable lectures, support and discussions.

I would like to thank Professor B. Golding, Professor D. Stump and Professor T. J. Pinnavaia for serving on my Ph.D guidance committee and their valuable suggestions.

I want to thank Professor J. S. Kovacs, Ms. S. Holland, Ms. J. King, and Ms. K. Cords for their concern, help, and assistance, Professor T. Kaplan for his concern and encouragement. I also want to thank all my friends in this department for their valuable discussions and help in preparation of this thesis.

I would like to express my deepest thanks to my husband Shixi and my son Philip for their love, understanding and support. I also thank my parents and my family for their love and encouragement.

Financial support from the Natural Science Foundation and the Center for Fundamental Materials Research of MSU is also gratefully acknowledged.

Contents

Abstract	i
Acknowledgments	iii
1 Introduction	1
1.1 Characterization of porous media	2
1.1.1 Zeolites as examples of microporous (MP) solids	3
1.1.2 Pillared layered silicates (pillared clays)	7
1.2 Hubbard model	7
1.3 Contents of different chapters	10
2 Single Quantum Particle in 1D MP Channels	12
2.1 Introduction	12
2.2 System and method	20
2.3 Results for the ground state	22
2.3.1 Effect of geometry on the energy spectrum and m/m^*	22
2.3.2 Analytical fits to m/m^*	29

2.3.3	Effects of attractive potential due to adsorbed ions on the cage surface and silicate framework	34
2.4	Excited state	40
2.5	Summary	43
3	Low-Temperature Thermodynamic Properties of Helium Clusters in K-L Zeolite	44
3.1	Introduction	44
3.2	Physical system	46
3.3	Experimental results	48
3.4	Models of the system	50
3.5	Results for Bosons (B) and Spinless fermions (SF)	52
3.5.1	Difference between B and SF due to statistics	52
3.5.2	Difference between B and SF due to mass	54
3.5.3	Comparison with experiments	57
3.5.4	Spin effect	60
3.6	Conclusion	66
4	Effect of Tunneling Disorder on the Low Temperature Heat Capacity of ^3He and ^4He in Zeolite Channels	67
4.1	Introduction	67
4.2	Model with disorder	70
4.3	Results and discussions	71

4.4	Summary	75
5	Thermal Excitations of Xenon Clusters Inside a Model L-Zeolite	80
5.1	Introduction	80
5.2	Method and the physical system	82
5.3	Results	85
5.3.1	MC simulation	85
5.3.2	MD simulation	101
5.4	Discussion	105
6	Percolation and Diffusion in 2D Microporous Media: Pillared Clays	110
6.1	Introduction	110
6.2	Physical system and the geometrical model	112
6.3	Review of experimental situation	116
6.4	Results of computer simulation	119
6.4.1	Lattice model	119
6.4.2	Continuum diffusion	122
6.4.3	Comparison with experiment and discussion	128
6.5	Summary	132
7	Conclusion	134

A Estimation of nearest neighbor He-He interaction in K-L Zeolite 136

List of Figures

1.1	A [001] view of the framework of L-zeolite.	5
1.2	A unit cell of L-zeolite (also called cage) showing the main channel viewed along the channel axis.	6
1.3	An idealized 2:1 layered silicate.	8
2.1	A typical channel structure of $Cs^+(18Crown6)_2e^-$ electrone. The ring structures are $(18Crown6)_2$ and spheres are Cs ions, each Cs ion is sandwiched between two $(18Crown6)$ molecules.	15
2.2	The channels of $Cs^+(18Crown6)_2e^-$ electrone (It is the negative picture of the previous figure) at 0.54 Å from the molecular van der Waals surfaces. Major channels are about 1.9 Å by 4 Å in cross section and 2-3 Å long, with a pronounced "pinch" in the channel center caused by hydrogen atoms of the crown center. Those major channels are connected by narrow channels which are ≈ 1.5 Å in diameter and ≈ 4 Å long.	16
2.3	A channel structure of L-zeolite which is formed by silicate framework	17

2.4	The channels of L-zeolite (It is the negative picture of the previous figure) at 2.4 Å from the channel surfaces. The porosity is about 57 %	18
2.5	(a). Schematic picture of a one-dimensional tubular channel in K-L zeolite; (b). Geometrical parameters describing the one dimensional model channel	19
2.6	A typical energy band structure in the one-dimensional tubular MP channel	23
2.7	The c -dependence of m/m^* for three different neck diameters in the 2D case. Dashed lines are guide to the eyes.	25
2.8	The c -dependence of m/m^* for two different neck diameters in the 3D i.e. tubular channel case. Dashed lines are guide to the eyes.	26
2.9	The c -dependence of E_{min} for 2D and 3D case.	27
2.10	Square of the wave function in 2D case	28
2.11	Effective mass as a function of neck diameter d for 3D case	30
2.12	Effective mass as a function of neck diameter d for 2D case	31
2.13	Ground state energy as a function of a . The insert is a log-log plot which shows $E_{min} \sim a^{-2}$. Dashed lines are guide to the eyes.	32
2.14	m/m^* as a function of a which shows that the effective mass ratio does not depend on a (b/a and c/a are fixed). The observed variations with a represents the inaccuracies in our calculation of m/m^*	33

2.15 Comparison between fitted (varying α and fixing n) and calculated m/m^*	35
2.16 Comparison between fitted (varying n and fixing α) and calculated m/m^*	36
2.17 The azimuthal distribution of He - K-L zeolite potential with or without K^+ ions. (a) and (b) show the potential along the center of the channel wall. (c) shows the potential along the wall of neck. $0K^+$, $4K^+$ and $6K^+$ correspond to 0, 4 and 6 K^+ ions silicated on the cage wall, respectively.	37
2.18 Angular dependence of square of the wave function at $k = 0$ with (a). $p=2$, (b). $p=3$	39
2.19 Square of the wave function at $k = 0$ with (a). $V=0$, (b). $V = 2.0e_0$, (c). $V = 5.0e_0$	41
2.20 Energy bands for the ground state, first excited state and second excited state for 2D case with $a = b = 10 \text{ \AA}$, $c = 7.5 \text{ \AA}$ and $d = 5.0 \text{ \AA}$	42
3.1 Schematic picture of a cross section of K-L Zeolite channel showing the silicate framework and ring arrangement of He adsorption sites.	47
3.2 The experimental results of heat capacity of He atoms as a function of T for fixed He concentration.	49
3.3 Lowest 20 (out of 70) energy states of spinless fermions (SF) and bosons (B) for particles in a 8-site ring.	55

3.4	Temperature dependence of the molar heat capacity for 8-site n-particle spinless fermion and boson systems.	56
3.5	The molar heat capacity for the (8,4) system with bose statistics and different t , $V=-24K$	58
3.6	Heat capacity for the spinless fermions as a function of $\langle n \rangle$ (a) and as a function of T (b).	61
3.7	Heat capacity for the spinless fermions as a function of T (shows the discrepancies between experiment and theory).	62
3.8	Heat capacity for the bosons as a function of $\langle n \rangle$ (a) and as a function of T (b).	63
3.9	Comparison of the heat capacity between SF and F for (8,2) and (8,3) systems. $t=14K$, $V=-24K$	65
4.1	Comparison of the density of states with and without disorder for 4 site 2 particle case.	73
4.2	Comparison of the heat capacity with and without disorder for 4 site 2 particle system.	74
4.3	Heat capacity vs. temperature for fixed helium atom concentration for 3He with and without disorder.	76
4.4	Heat capacity vs. helium atom concentration $\langle n \rangle$ for fixed temperatures for 3He with and without disorder.	77
4.5	Heat capacity vs. temperature for fixed helium atom concentration for 4He with and without disorder.	78

5.1	Single-particle potential energy V_s for Xe as a function of Φ in a plane passing through the center of the L-zeolite cage in units of K, r is the radial distance from the cage axis.	87
5.2	Single-particle potential energy V_s for Xe as a function of Φ in a plane passing through the center of the L-zeolite cage in units of K, r is the radial distance from the cage axis.	88
5.3	Single-particle potential energy V_s as a function of z inside the L-zeolite cage in units of K, r is the radial distance from the cage axis. The azimuthal angle ϕ is chosen to be zero.	89
5.4	Average energy $\langle E \rangle$ vs T for a single Xe atom inside L-zeolite.	91
5.5	Positions of the six Xe atoms (large circles) in the ground state of Xe_{6c} and the framework Oxygen atoms (small circles) in the $z=0$ plane.	92
5.6	The ground state of a free Xe_6 cluster	93
5.7	Melting of a Xe_{6c} cluster inside the L-zeolite;	95
5.8	The same as in the previous figure excepting here each run consists of 10^6 MC steps and the number of MC run was 3.	96
5.9	Melting of a free Xe_6 cluster: the average energy $\langle E \rangle$ vs T	98
5.10	Melting of a free Xe_6 cluster: average bond length fluctuation δ vs. T	99
5.11	Average energy $\langle E \rangle$ vs T for Xe_{6CAM} , a cluster assembled material consisting of a periodic array of Xe_6 clusters inside L-zeolite	100
5.12	τ^2 vs. time for the Xe_{6c} system	102

5.13	r^2 vs. time for each Xe atom along with the result of the averaged one for the $Xe_{\delta c}$ system	103
5.14	r^2 vs. time for the $Xe_{\delta c}$ system at three different temperatures . .	104
5.15	r^2 vs. time for the $Xe_{\delta CAM}$ system	106
5.16	r^2 vs. time of run2 with x^2, y^2, z^2 also for the $Xe_{\delta CAM}$ system . .	107
5.17	Diffusion rate $D(t)$ vs. time for the $Xe_{\delta CAM}$ system	108
6.1	Argon atoms diffusing in the annealed pillared clay	117
6.2	The amount of Argon adsorbed by $(Co^{3+}(en)_3)_{1-x}(Cr^{3+}(en)_3)_x - FHT$ as a function of x	118
6.3	Lateral constraints on Argon atoms diffusing in the annealed system	120
6.4	The x dependence of the size of the largest cluster of A-A bonds obtained from simulation of $100 \times 100, 400 \times 400$ and 2000×2000 lattices.	123
6.5	Typical curves of R^2 and D/D_0 vs. time steps	126
6.6	D/D_0 vs. step length for $Ar(x=1)$ and $He(x=0,1)$	127
6.7	The relative diffusion constant of Argon atom ($d_{Ar} = 4.0 \text{ \AA}$) diffusing in FHTD as a function of x	129
6.8	The relative diffusion constant of Helium atom ($d_{He} = 2.6 \text{ \AA}$) diffusing in FHTD as a function of x	130
6.9	The ratio $D^{He}(x=0)/D^{He}(x=1)$ as a function of the diameter of Helium atom when Helium gas diffuses in $[Cr^{3+}(en)_3]_x[Co^{3+}(en)_2+(en)]_{1-x} - FHT$ system.	131

A.1	A view of the geometrical arrangement of Helium atoms and K^+ ions of K-L zeolite cage.	137
A.2	(a) Shows the interaction between one Helium atom and K^+ ion.	
	(b) shows the interaction between two Helium atoms and K^+ ion.	137

Chapter 1

Introduction

Physical properties of molecular or atomic systems are known to be dramatically modified by confinement in restricted geometry. However, making explicit and unambiguous connections between the geometry of the confining space and the molecular properties have proven to be difficult in general, and the connections, when made, are frequently controversial [1]. Nevertheless, behavior of these confined systems is of considerable fundamental and practical interest. From a fundamental point of view, confinement reduces the phase space accessible to the system. For example, the system of molecules/atoms can behave as a d -dimensional system with $d < 3$ and we know that physical properties such as phase transitions, transport and electronic properties are profoundly affected by the dimension d . In addition, confinement can introduce inhomogeneities and disorder produced by the confining medium which can also modify the physical properties of the imbibed system. From a practical point of view, a wide class of porous confining media such as zeolites, vycors, aerogels etc. are used commercially in such diverse fields as chromatography, oil recovery, catalysis and membrane separation technology.

Many experimental and theoretical studies have been carried out to investigate

adsorption, diffusion and thermodynamic and dynamic properties of molecules trapped inside porous media [1]-[11]. In addition, computer simulations have been extremely useful in elucidating the behaviour of molecules confined in different types of porous media [12]-[23]. One of the major tasks of theoretical condensed matter physics is to model the physical system possible and to explain the observed electronic, magnetic, structural, and dynamical properties of the confined system and furthermore, to predict the properties of new but related systems.

During the years of my research in condensed matter theory in the group of Prof. Mahanti, I have been focusing my attention on understanding the general physical properties of rare gases trapped inside microporous materials, such as pillared clays and zeolites. I have studied the behavior of He systems which behave quantum mechanically at low temperatures and classically at room temperature and Xe, Ar which are of practical interest. Because of their heavy mass, Xe and Ar can be treated classically. In this chapter, I will give a general introduction to the confining media of interest to me, namely zeolites and pillared layered silicates. In addition, I will give a brief description of the Hubbard model which I have used to represent the quantum mechanical behaviour of He atoms trapped inside zeolites. I also give a brief description of the contents of each following chapter.

1.1 Characterization of porous media

Systems characterized by spatial restrictions and low dimensions, such as zeolites, membranes, polymers, and porous glasses and minerals, are called porous media. According to their pore size, porous media can be divided into three classes [24]. The first class includes macroporous media, where the length scale of the pore

is greater than 500\AA . Mesoporous media constitute a second class in which the pores are larger than $\sim 20\text{\AA}$ and smaller than 500\AA . A third class, with which we are concerned in the thesis, embraces microporous (MP) media, with pore sizes less than 20\AA . Zeolites are the most common examples of the MP media [25]. Furthermore, depending on the pore structure, the effective dimensionality of the physical system can be different. For example, parallel-walled slit pores, such as those thought to occur in some partially graphitized carbon blacks [26], graphite intercalation compounds [27] and pillared clays [28], restrain the particles to move in two-dimensions, i.e., the system has one finite dimension out of 3D. An example of restrictions in two finite dimensions is provided by the cylindrical pores in porous vycor [29, 30]. Zeolites are mostly 3D constriction but with periodic structures [25]. Aerogels and vycor glasses have much more complicated pore structures which make the effective dimensionality of the system become a non-integer number, namely their geometry is fractal [31].

1.1.1 Zeolites as examples of microporous (MP) solids

Zeolites are microporous inorganic compounds [25, 32]. Their crystal structure contains large pores and voids which are usually regular and the effective pore sizes are in the range from 3\AA to over 10\AA which are sufficient to permit the diffusion of small organic molecules – a feature which gives rise to many of the important applications of these materials, such as heterogenous catalysts and molecular sieves. Most zeolite networks are aluminosilicates.

There are many kinds of zeolites. One of the simplest zeolites with which we are interested in our research is L-zeolite. Fig. 1.1 is a view along the [001] direction of the aluminosilicate framework of L-zeolite [33, 34]. The idealized

composition per unit cell of L- zeolite is $K_6Na_3[(AlO_2)_9(SiO_2)_{27}]21H_2O$. The structure of the Linde type L-zeolite[34, 35] consists of a series of one-dimensional channels which form hexagonal crystal structure and the c axis is along the channel direction. The main channel has twelve framework oxygen atoms bounding the aperture which is a nearly regular dodecagon. Six atoms form a ring of radius of 4.92Å and the other six form a ring of radius 5.25Å. The main channel opens up to a diameter of 14.43Å and then narrows back down in a unit cell length of 7.5Å. Fig. 1.2 gives another view of the main channel seen along the c-axis. As can be seen in fig. 1.1 the main channel is surrounded by six symmetrically spaced secondary channels that connect the main channels of adjacent unit cells. We will refer to these secondary channels as 8-channels because of the elongated octagon shape of the channel when viewed along an axis parallel to the main channel. According to this same viewpoint, there are six 4-channels which surround the main channel and separate the 8-channels, and adjacent to each 4-channel on the opposite side from the main channel is a 6-channel. A unit cell of this zeolite contains one main channel, two 6-channels, three 8-channels, and six 4-channels. The shape of the unit cell is that of a rhomboid with side length 18.4Å, an interior angle of 60 degrees, and a depth of 7.52Å. The symmetry of the crystal is P6/mmm as described in "The International Table for X-ray Crystallography"[36]. The total number of framework atoms in this unit cell is 108, with 72 Oxygen and 36 T-atoms (Si or Al).

K-L zeolite has the same overall structure as L-zeolite but with nearly nine K^+ ions in each cage, for example there are 8.94 K^+ ions and 0.61 Na^+ ions/unit cell. There are four of these nearly nine K^+ ions sitting near the wall of the cages while the rest of them are distributed in the aluminosilicate framework. The presence

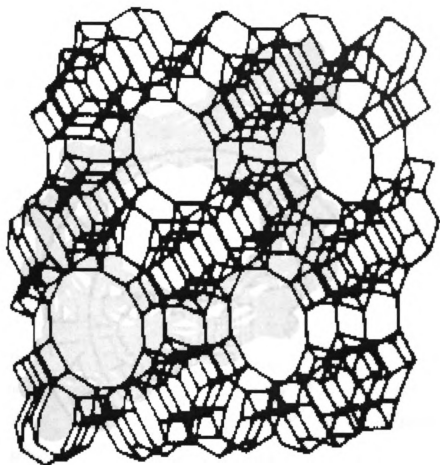


Figure 1.1: A [001] view of the framework of L-zeolite.

Active



Figure 1.2: A unit cell of L-zeolite (also called cage) showing the main channel viewed along the channel axis. Only oxygen atoms of the framework are shown.

of K^+ ions near the wall of the cage and inside the silicate frame in K-L zeolite provide additional attractive potential on the adsorbed atoms and also introduce disorder in the system.

1.1.2 Pillared layered silicates (pillared clays)

Pillared clays are intercalation compounds in which stable pillaring ions of various sizes are intercalated into the galleries of layered silicates. The layered silicates are usually aluminosilicate minerals or clay minerals such as vermiculite, fluorohectorite, and montmorillonite. Fig. 1.3 is a schematic illustration of an idealized 2:1 layered silicate which has two tetrahedral sheets fused to a central octahedral sheet [37, 38]. In ideal case, the layers are neutralized. But in most cases, there are net negative charges in the layers because of the random replacement of Si^{4+} by Al^{3+} . Usually, these charges are neutralized by small positive ions, such as Na^+ , in between the layers. Using special techniques, one can replace these small ions by some large cations (called pillars) into the galleries of the layers to obtain a new material which has large voids or inter lamellar microporous space accessible to guest molecules.

Because of the nature of the layers and large pores (about 20\AA), pillared clays are excellent two-dimensional microporous materials inside which large molecular species can diffuse into active surface sites [33] and undergo catalytic reaction.

1.2 Hubbard model

Hubbard model [39, 40], one of the simplest models describing an interacting many-body system, was proposed by Gutzwiller, Hubbard and Kanamori in early

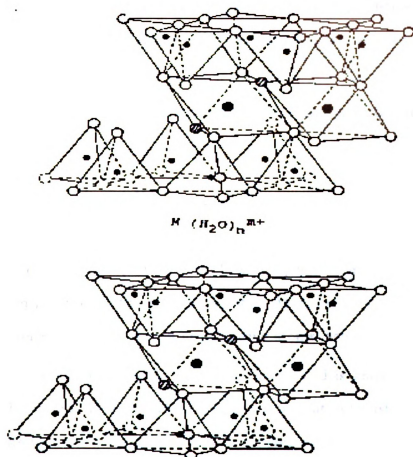


Figure 1.3: An idealized 2:1 layered silicate. Open circles are oxygens, small closed circles are tetrahedral site cation Si, Al. Large closed circles are octahedral site cation Al, Mg, Fe, Li, vacancy.

sixties. This model has been applied to study a great variety of physical systems, electrons in solid [39], liquid ^3He [41], Bose condensation of ^4He in disordered media [42] etc. Recently, this model and its generalizations have been found to be quite promising to study the strong correlation physics in pristine and doped Mott insulators, the latter showing high temperature superconductivity, colossal magneto-resistance etc.

The simplest Hubbard model for fermions with spin is usually written as follows:

$$H = -t \sum_{\langle ij \rangle \sigma} c_{i\sigma}^\dagger c_{j\sigma} + U \sum_i n_{i\uparrow} n_{i\downarrow} \quad (1.1)$$

where $c_{i\sigma}^\dagger$ ($c_{i\sigma}$) are creation (annihilation) fermion operators associated with site i and spin σ ; $n_{i\sigma} = c_{i\sigma}^\dagger c_{i\sigma}$ is the number operator. Attention is normally restricted to hopping (or tunnelling) between neighbouring atoms, denoted by $\langle ij \rangle$.

The first term corresponds to chemical bonding and is known as ‘hopping’ [39, 40]. This term is a single particle term and represents a transfer of a particle from one site to a nearest neighbor site with hopping matrix element t . This contribution favours itinerancy or delocalization by reducing the one particle energy (also referred to as the kinetic energy).

The second term corresponds to the Coulomb repulsion between two particles when they occupy the same localized site and is therefore a two particle interaction term. The long range contributions to the electron-electron interaction is assumed to be screened and only the interaction when both the particles are on the same site is retained, yielding a repulsive energy of U . The model can be extended to take care of both longer-range hopping ($t \rightarrow t_{ij}$) and longer-range interaction.

For fermions (electrons or ^3He) the Hubbard model is also referred to as the Mott-Hubbard model because Mott realized the significance of the repulsive U term in the problem of metal-insulator transition. If we apply the model to Bosons (such as ^4He), then c 's become Boson operators and the model is called Bose-Hubbard model.

There are some basic properties of the Hubbard model. Two of them are important in the current study, namely (i) $n_\sigma = \sum_{i\sigma} c_{i\sigma}^\dagger c_{i\sigma}$ commutes with H , therefore n is a good quantum number, and (ii) there is particle-hole symmetry.

1.3 Contents of different chapters

We will next briefly describe the contents of each chapter.

In chapter 2, we investigate the effective mass m^*/m of He atoms (bare mass m) moving inside one-dimensional tubular microporous channels consisting of cylindrical cages connected by necks of different diameters and lengths by solving the one-particle Schrödinger equation numerically. These channels are simplified models of L-zeolite channels. From the relation between the effective mass, wave function and the geometrical parameters, we can get some insight into the single particle transport property. Most of the contents in this chapter were published in Phys. Rev. B. [43]. In chapter 3, we discuss the low-lying excitations of He clusters inside K-L zeolite using extended Mott-Hubbard and Bose-Hubbard models. The results of the heat capacities are compared with experiments. The content of this chapter was published in Phys. Rev. Lett. [44]. In chapter 4, we extend our Mott-Hubbard and Bose-Hubbard models introduced in chapter 3 by including disorder effect into the models. We study in detail the effects of disorder in the

tunnelling on the low temperature thermal properties. This modification has led to a much better agreement with experiments especially at very low temperatures.

In chapter 5, thermodynamic and dynamic properties of an isolated Xenon cluster confined inside L-zeolite (denoted as Xe_{nc} , $2 \leq n \leq 6$) and Xenon clusters confined inside L-zeolite as a cluster assembled material (denoted as Xe_{nCAM} , $n = 6$) are studied by Monte Carlo and molecular dynamic simulation methods. The differences between free Xe_6 cluster, Xe_{6c} and Xe_{6CAM} are explored. A manuscript based on the contents in this chapter is going to be published [21]. In chapter 6, we use continuum diffusion simulation to probe the percolative properties of Argon and Helium atoms in the heteroionic pillared clay $[Cr^{3+}(en)_3]_x[Co^{3+}(en)_2 + (en)]_{1-x}$ -fluorohectorite(FHT), respectively. The contents of this chapter was published in J. Chem. Phys [45]. Finally, we give a brief conclusion in chapter 7.

CH

Si

M

2.1

I

ing

at h

and

ca

sub

me

lia

mi

ne

pe

ce

et

Chapter 2

Single Quantum Particle in 1D MP Channels

2.1 Introduction

It is known that the physical properties of helium atoms (3He , 4He), when moving in restricted geometry, differ dramatically from those in the bulk, particularly at low temperatures, due to the influence of the topology of the confining medium and the adsorption potentials exerted by the medium on the *He* atoms. Typical examples are: helium adsorbed on graphite [46, 47] and alkali metal [48, 49] substrates, inside porous glass such as vycor [50, 51], aerogel [31] or microporous media such as zeolites [52]-[60]. In fact, recent sorption measurements [61] of helium in fullerite crystals and films show that helium atoms are mobile within the microporous space of these crystals, thus opening up the possibility of realizing a new type of three-dimensional quantum fluid.

One of the fundamental quantities that not only controls the mobility (transport), but also other physical properties such as heat capacity and magnetic susceptibility (through density of states and interaction effects) in a confining geometry is the effective mass (m^*/m) of *He* atoms. Depending upon the strength of

the substrate potential and the nature of the microporous geometry, m^*/m can vary enormously. In particular, if this effective mass ratio is much larger than 1, any small perturbation such as coupling to the vibrational degrees of freedom of the confining medium, inter-particle interaction or static disorder will tend to localize the particles, thus strongly affecting their transport and thermodynamic properties. Therefore, before one attempts to understand the effects of disorder (both structural and thermal) and inter-particle interaction, one must understand the effect of periodic geometry on the motion of a single helium atom.

In this chapter, we address the question of the effective mass of a single helium atom moving in one-dimensional microporous channels found in K-L zeolite [57, 58], imogolite [62] and similar one dimensional zeolites. We focus on K-L zeolite for which we will construct simple geometric models. Our results are however quite general. We also present some results about a few low-lying excited states. We study these systems primarily for two reasons. First, one-dimensional systems are relatively simple and second, extensive studies of low-T thermodynamic properties of ^3He and ^4He atoms in K-L zeolite have been made [57] which we can address theoretically. As discussed in chapter 1, K-L zeolite consists of one-dimensional channels of about 14.43 Å diameter modulated by constrictions (necks) of about 7.5 Å in diameter. Other one-dimensional zeolites in which helium adsorption studies have also been made are ZSM-23 [59, 60], whose diameter is ~ 5.5 Å.

Before going to the zeolite, we would like to point out that such physical systems for which our calculations of m/m^* are also relevant are electrons moving inside the narrow channels of electrified [63] where the channels are formed in the space between large organic cage-like molecules encapsulating positive alkali

ions. Channels in a typical electrider are shown in fig. 2.1 and fig. 2.2 [64]. Electriders are an exciting new class of systems which exhibit a wide variety of electronic properties governed by the channel geometry. We also show in fig.2.3 and fig.2.4 [64] the channels in L-zeolite for comparison. Also recently electronic energy band structures have been obtained by Lent et.al. [65] for electrons moving inside periodically modulated channels, but these authors have not focussed on the question of the effective mass which is of major interest here.

The atomic structure of an actual K-L zeolite as we have discussed before is quite complicated. However we can analyze the essential physics of quantum transport along the channel axis by using a simple model of the microporous geometry. In a later chapter where we deal with classical systems such as Xe, we will use a realistic atomic model of zeolite. Fig. 2.5a gives a schematic picture of K-L zeolite, whose channels consist of cages connected by neck regions. The boundary walls are formed by *Si-O-Si* networks. In K-L zeolite, some of the Si^{4+} ions are replaced by Al^{3+} ions and in addition there are charge compensating K^+ ions. Some of these K^+ ions are attached to the interior walls of the cage and the rest are embedded in the silicate framework. The K^+ ions on the wall provide an attractive potential on the helium atoms. Thus in addition to the geometrical confinement effects, the attractive potential produced by the K^+ ions and the silicate framework can also affect m/m^* dramatically, particularly when the neck becomes narrow.

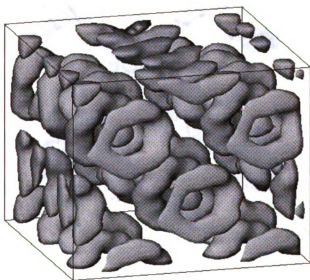


Figure 2.1: A typical channel structure of $Cs^+(18Crown6)_2e^-$ electride. The ring structures are $(18Crown6)_2$ and spheres are Cs ions, each Cs ion is sandwiched between two $(18Crown6)$ molecules.

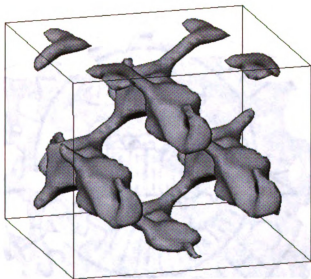


Figure 2.2: The channels of $Cs^+(18Crown6)_2e^-$ electride (It is the negative picture of the previous figure) at 0.54 \AA from the molecular van der Waals surfaces. Major channels are about 1.9 \AA by 4 \AA in cross section and $2\text{-}3 \text{ \AA}$ long, with a pronounced "pinch" in the channel center caused by hydrogen atoms of the crown center. Those major channels are connected by narrow channels which are $\approx 1.5 \text{ \AA}$ in diameter and $\approx 4 \text{ \AA}$ long.

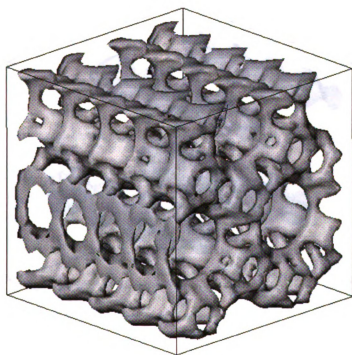


Figure 2.3: A channel structure of L-zeolite which is formed by silicate framework

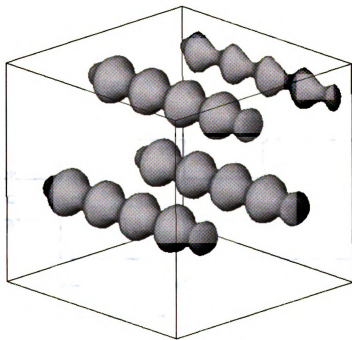


Figure 2.4: The channels of L-zeolite (It is the negative picture of the previous figure) at 2.4 Å from the channel surfaces. The porosity is about 57 %.

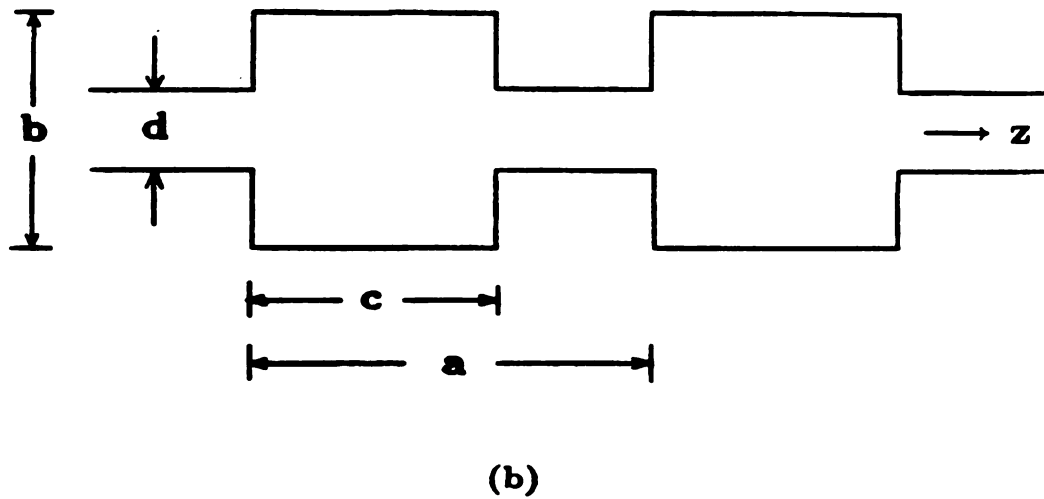
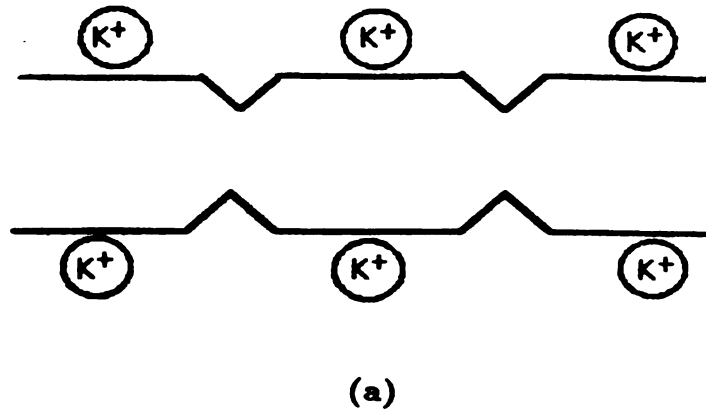


Figure 2.5: (a). Schematic picture of a one-dimensional tubular channel in K-L zeolite; (b). Geometrical parameters describing the one dimensional model channel

2.2 System and method

Fig. 2.5b describes the geometrical parameters used in our simple one-dimensional model of the channels in K-L zeolite: A given channel is assumed to be cylindrical and periodic along the z -axis with periodicity a . The channel consists of cages (chambers) of diameter b and length $0 \leq c \leq a$, connected by necks of diameter d and length $a - c$. Transport properties of a quantum particle in such a channel are influenced both by the geometry and the potential. For simplicity, we assume that the boundary is a hard wall where the wave function vanishes.

The single particle Schrödinger equation inside the cages is:

$$-\frac{\hbar^2}{2m} \nabla^2 \psi + V\psi = E\psi \quad (2.1)$$

We solve the single particle Schrödinger equation by setting the eigenfunctions as Bloch functions, $\psi_{n,l,k}(r, \phi, z) = u_{n,l,k}(r, \phi, z)e^{ikz}$. We then solve the equation for the cell periodic part $u_{n,l,k}$ and eigenvalues $\varepsilon_{nl}(k)$. The numerical method used is the optimized iterative method for eigenvalue problems [66] for the '1D' case, i.e. $\psi(r, \phi, z) \rightarrow \psi(z)$, with appropriate generalization to our problem. It includes the following steps

1. Divide the unit cell into $n_z \times n_r \times n_\phi$ mesh.
2. Give an initial guess of the wave function ψ^0 which is normalized properly.
3. The energy of the system is then given by

$$E = \langle \psi | H | \psi \rangle = \int (\psi^* \nabla^2 \psi + V\psi^* \psi) d\tau \quad (2.2)$$

where $\psi = \psi^0$, $V = V/e_0$ and e_0 is the energy unit we have used in this chapter ($e_0 = \hbar^2/(2m\text{\AA}^2)$, m is the mass of the particle).

4. Modify the wave function as following:

$$\psi^1 = (1 - Hdt)\psi^0$$

where dt is a fake time interval. Then, normalize ψ^1 .

5. Repeat step 3 and 4 until $|\Delta E| = |E^{t+1} - E^t| \leq \epsilon$, where ϵ is an appropriately chosen convergence parameter. Thus, we get the ground state energy and the wave function for a fixed wave number k .

To get the first excited state, the only thing we have to do is, after step 4, not only normalize the wave function but also orthogonalize it to the previously obtained ground state wave function.

Using the above method we can get the eigenvalues and corresponding eigenvectors for the ground state and several low lying excited states. To probe the effect of the dimensionality of the lateral (perpendicular to the tube axis) confinement, we have also studied the two dimensional case where $\psi(x, y, z) = \psi(x, z)$.

Although we have obtained excited states in some case, here we discuss only the lowest energy band for a fixed overall size of the channel i.e. fixed a, b shown in fig. 2.5b, but with different cage size c and neck diameter d . Fig. 2.6 shows the typical ground state energy band structure. Using this band structure and the effective mass concept, i.e. assuming that $E = \hbar^2 k^2 / (2m^*) = (m/m^*)k^2(\hbar^2/2m)$ near the bottom of the energy band, we have calculated m/m^* . The unit of energy is $\hbar^2/(2m \text{ \AA}^2)$. For ${}^3\text{He}$ this turns out to be 8K. One can easily see that $m/m^* = 1$ when $c = 0$ and/or $d = b$ which correspond to the propagation of a free particle along the z-axis. Thus, if $m/m^* \simeq 1$, the particle can move freely along the channel axis and if $m/m^* < 1$, the effective mass of the particle becomes large, i.e. the particle becomes heavier so that it is harder to move along the channel.

As $m/m^* \rightarrow 0$, the particle has a tendency to get localized in the presence of structural or thermal disorder and/or interparticle interaction. In addition to m/m^* , we have obtained the wave function densities (u^2) for the $k = 0$ state to show what happens to the unit cell wave functions as $m/m^* \rightarrow 0$. Finally, to see the effect of the K^+ ions, we have compared the difference between m/m^* for two cases, i.e. with and without the attractive potential produced by the K^+ ions.

2.3 Results for the ground state

2.3.1 Effect of geometry on the energy spectrum and m/m^*

To examine exclusively the dependence of the m/m^* on the geometry, we assume that the potential inside the channel is zero (i.e. $V=0$ in eqn. 2.2). The mesh for the results we present in this section is 40×40 for the 3D case and 80×80 for the 2D case (in 3D case, we can integrate out the angular dependence analytically when there is no extra potential).

We will first present our results for fixed values of a and b and different values of cage length (c) and neck diameter (d). For simplicity, in this paper we choose $a = b = 10 \text{ \AA}$, we do not expect much qualitative change from our present results when we take $a \neq b$. We will discuss the a dependence later. We find that the effective mass has a very complex geometry-dependence.

In fig. 2.7 we give the c -dependence of m/m^* for three different values of d ($= 3.5 \text{ \AA}$, 5.0 \AA and 6.5 \AA) for the 2D case, and in fig. 2.8, similar results are given for the tubular channel (3D case) for two different values of d ($= 3.66 \text{ \AA}$,

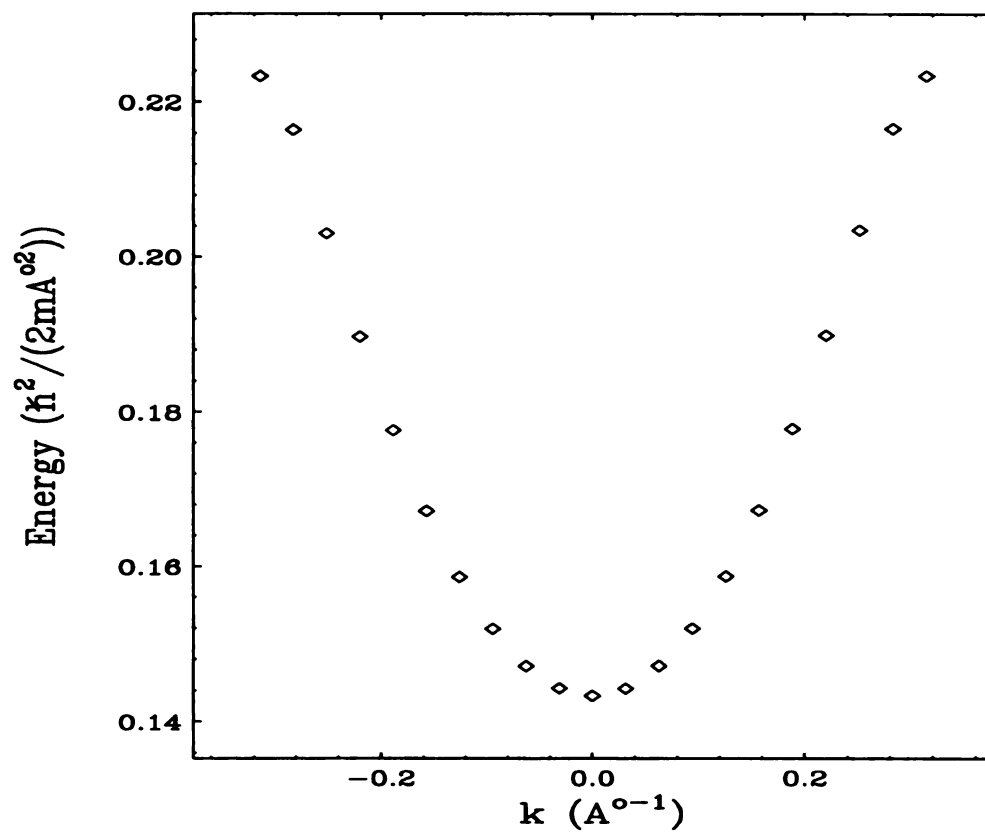


Figure 2.6: A typical energy band structure in the one-dimensional tubular MP channel

5.12 Å). The general trend is as follows: For small c , $m/m^* \sim 1$. It decreases with increasing c and attains a minimum for $c \sim d$. Then it increases with increasing c . The decrease is quite sharp for the tubular channel when d is small. In this case, there is a large region of c for which $m/m^* \ll 1$. Finally, when $c = a$ and $d < 10$ Å, m/m^* is still less than 1 because in this limit the particle still feels the effect of geometry even if the neck length $\rightarrow 0$. In fact $m/m^* \rightarrow 1$ only when $d \rightarrow b$, in which case the particle moves freely inside a tube of uniform cross section.

Fig. 2.9(a) and (b) are the corresponding ground state energy curves. As we can see, the ground state ($k=0$) energy curves are relatively simple and they go to the minimum when $c = a$.

To understand the physical origin of the sharp drop in m/m^* ie. enhanced tendency to localize as we increase the cage length c , we plot in fig. 2.10(a) ($c = 2$ Å) and fig. 2.10(b) ($c = 6$ Å) the square of the ground state wave function ($k = 0$) for the neck size $d = 3.5$ Å for the 2D case. For $c = 2$ Å $< d$, $m/m^* \simeq 1$ and the probability of the particle inside the neck region is quite high, whereas for $c = 6$ Å $> d$, most of the probability is in the cage with almost vanishing probability in the neck. In the latter case when we make $k \neq 0$, the k -dependence of the energy comes from small inter-cage tunnelling process. This leads to a rather low value for m/m^* which for these parameter values is $\simeq 0.19$.

One can also study the above tendency to 'localize' by changing the neck diameter d for fixed values of the cage length c . In fig. 2.11, we give m/m^* as a function of d for three different values of c ($= 2.5$ Å, 5.0 Å, 7.5 Å) for the tubular channel. Similarly, in fig. 2.12 we give m/m^* as a function of d for the 2D case. For small values of d , $m/m^* \rightarrow 0$ but as we increase d , there is a rapid increase

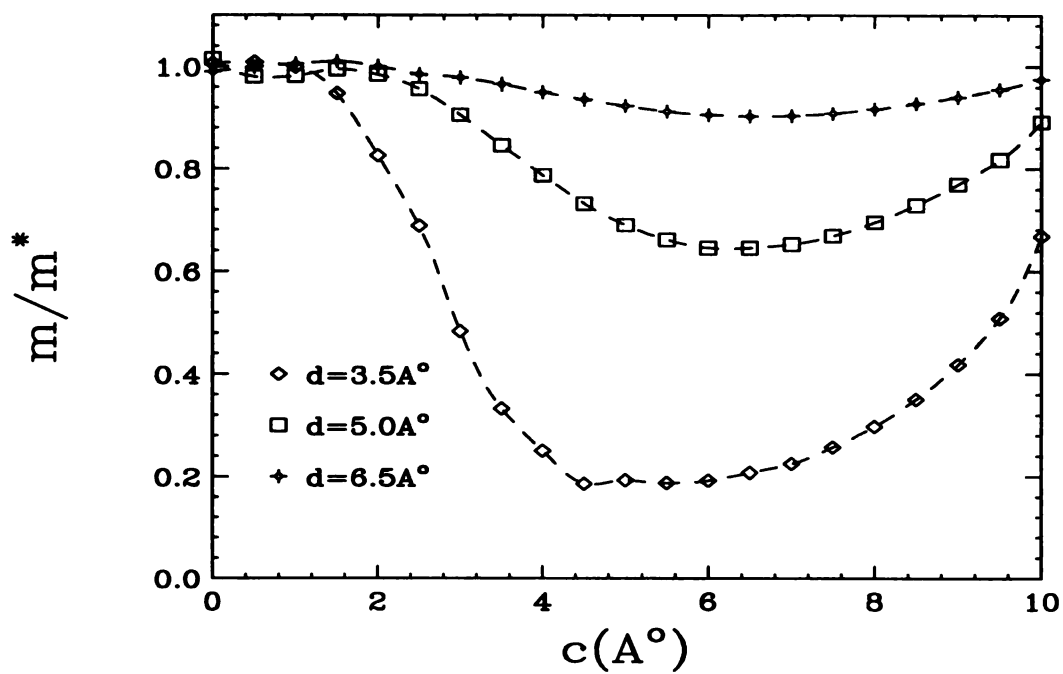


Figure 2.7: The c -dependence of m/m^* for three different neck diameters in the 2D case. Dashed lines are guide to the eyes.

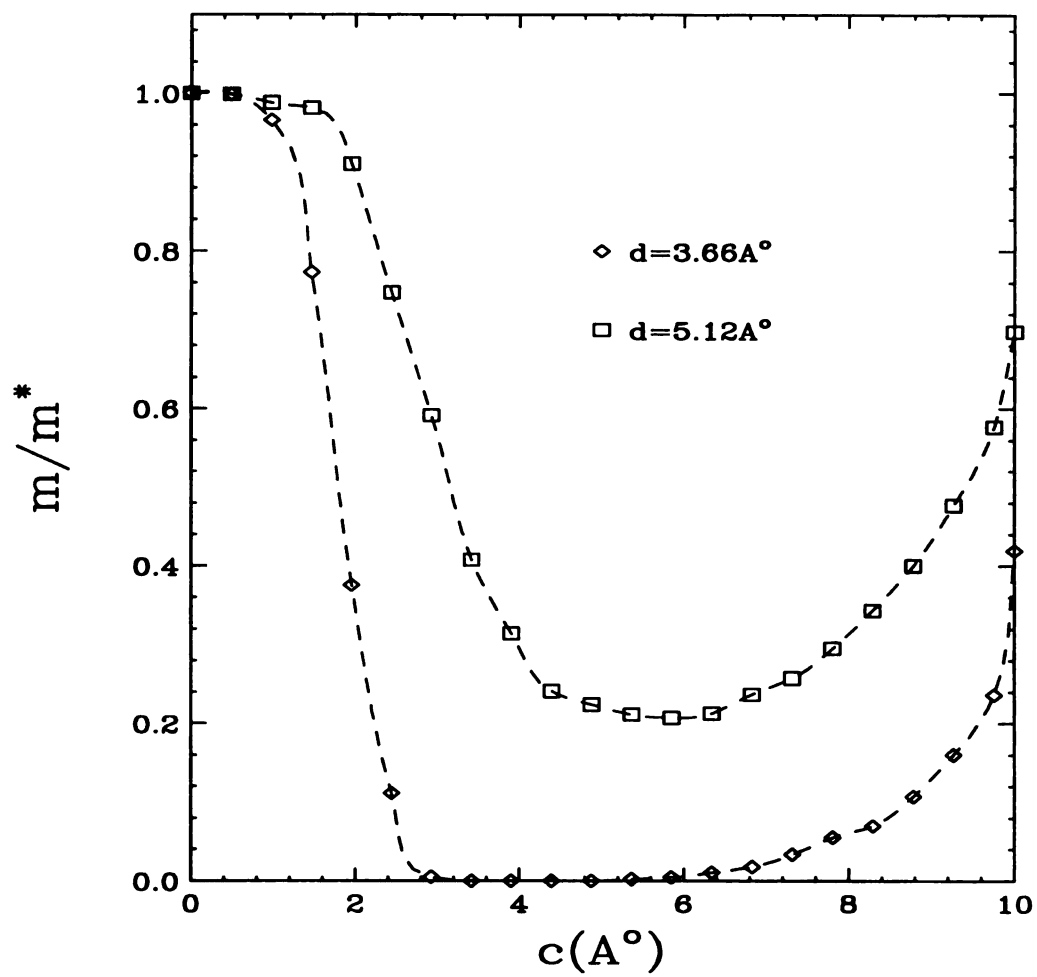


Figure 2.8: The c -dependence of m/m^* for two different neck diameters in the 3D i.e. tubular channel case. Dashed lines are guide to the eyes.

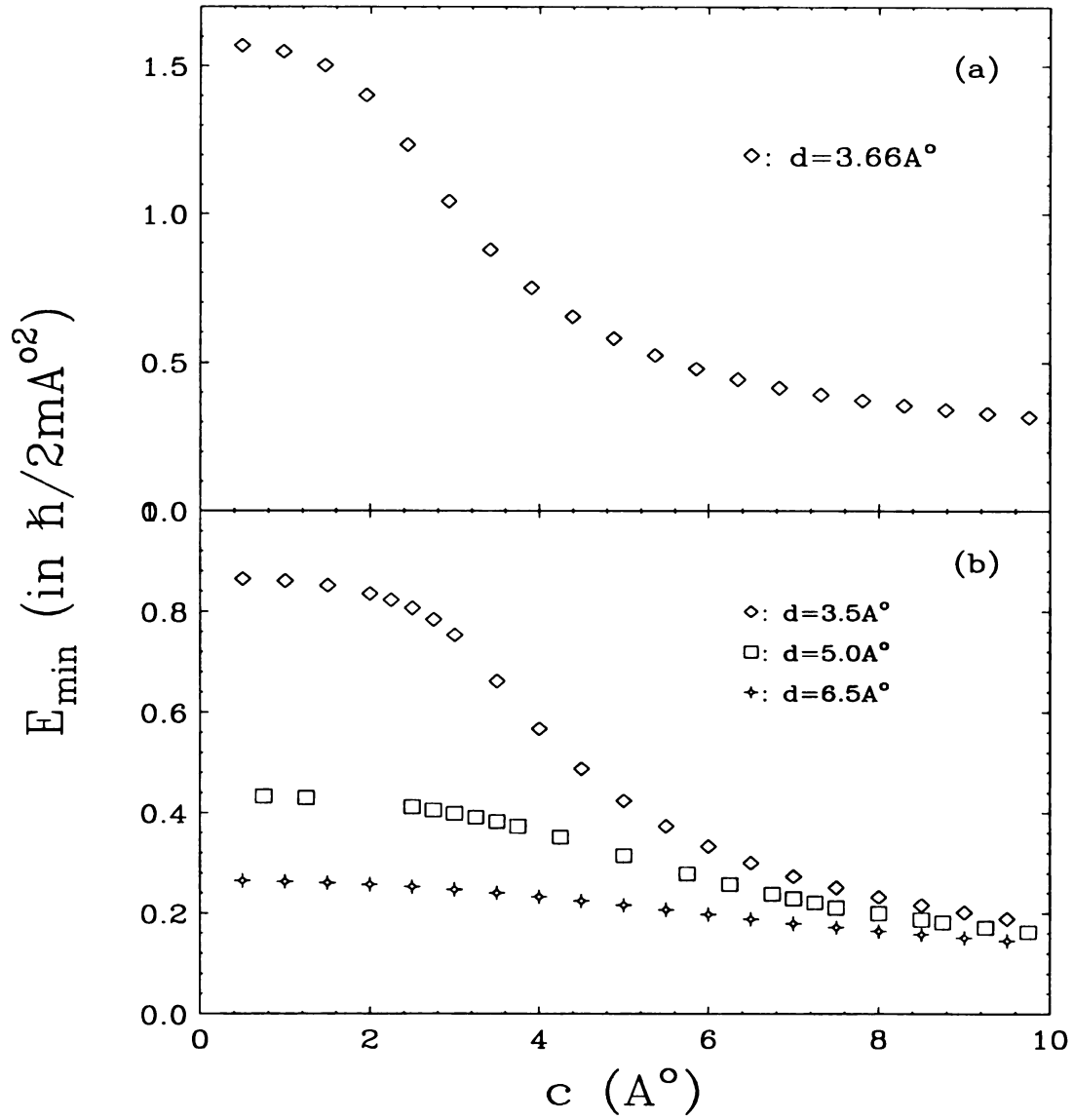
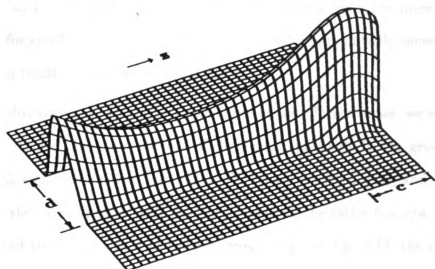
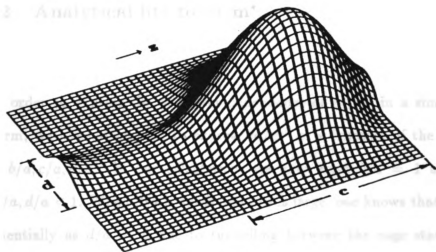


Figure 2.9: The c -dependence of E_{\min} for 2D and 3D case. (a). 2D. (b). 3D tubular case.



(a)



(b)

Figure 2.10: Square of the wave function (u^2) in a unit cell of a particle moving in a channel for $k = 0$ corresponding to the 2D case. The channel parameters of the unit cell are: $a = b = 10 \text{ \AA}$, (a). $c = 2.0 \text{ \AA}$ and $d = 3.5 \text{ \AA}$. For these parameters, cage length is smaller than the neck diameter and $m/m^* \text{ for this case } \simeq 0.83 \simeq 1$. (b). $c = 6.0 \text{ \AA}$ and $d = 3.5 \text{ \AA}$. For these parameters, cage length is larger than the neck diameter and $m/m^* \simeq 0.19 \ll 1$.

in m/m^* to 1. The sharpness of this increase depends on c , the increase being sharpest for small c . The value of d at which $m/m^* = 0.5$, initially increases with c but then tends to saturate at about 6 Å.

After discussing the geometry dependence of the effective mass, we would like to briefly discuss the a dependence of the energy, particularly the ground state energy, E_0 and the effective mass ratio. We have calculated E_{min} and m/m^* by changing the overall length scale (a) but keeping all the ratios $b/a, c/a, d/a$ same and we find that E_{min} scales as inverse square of a (see fig. 2.13, the insert is a log-log plot) while the effective mass ratio m/m^* is unchanged (see fig. 2.14), the small differences are due to numerical inaccuracies.

2.3.2 Analytical fits to m/m^*

In order to express the geometry-dependence of m/m^* in a simple analytical form, we have attempted to express m/m^* as a function of the scaled variables $b/a, c/a, d/a$. In our calculation, we have fixed $b/a = 1$ and changed $0 < c/a, d/a < 1$. When d/a is small and c/a is large, one knows that $m/m^* \rightarrow 0$ exponentially as $d/a \rightarrow 0$ due to tunnelling between the cage states. But to capture the $d/a, c/a$ dependence over a broad parameter space, we have used a different functional form. In fact, a two parameter function that fits m/m^* data reasonably well is given by

$$\frac{m}{m^*} = 1 - \frac{[1 - \tilde{d}^{\alpha\tilde{c}(1-\tilde{d}\tilde{c})}]^{\alpha(1-\tilde{d}\tilde{c})}}{1 + (\frac{n}{2}\tilde{d}\tilde{c})^n} \quad (2.3)$$

where $\tilde{c} \equiv c/a$, $\tilde{d} \equiv d/a$ and the two parameters are α and n .

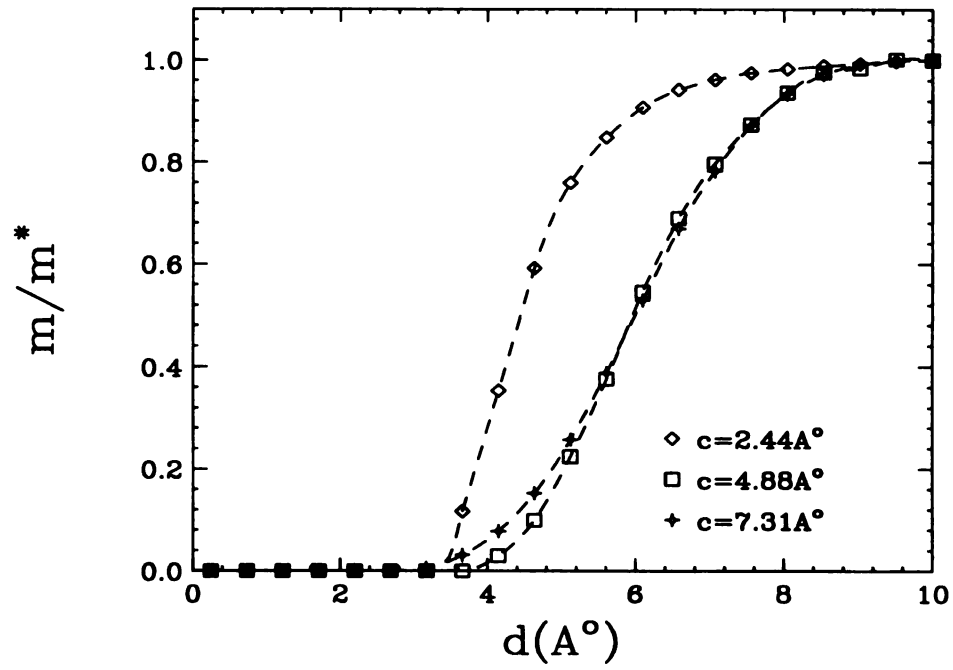


Figure 2.11: m/m^* as a function of neck diameter d for three specific values of the cage length c for the tubular case. Dashed lines are guide to the eyes.

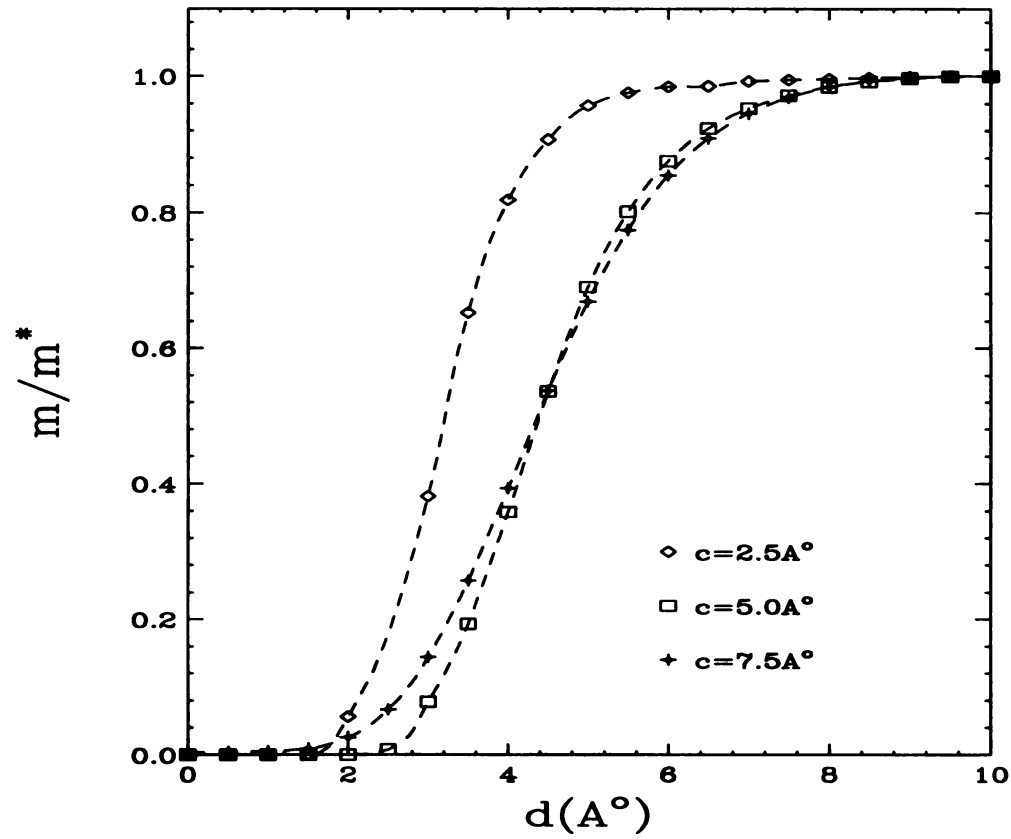


Figure 2.12: m/m^* as a function of neck diameter d for two specific values of the cage length c for 2D case. Dashed lines are guide to the eyes.

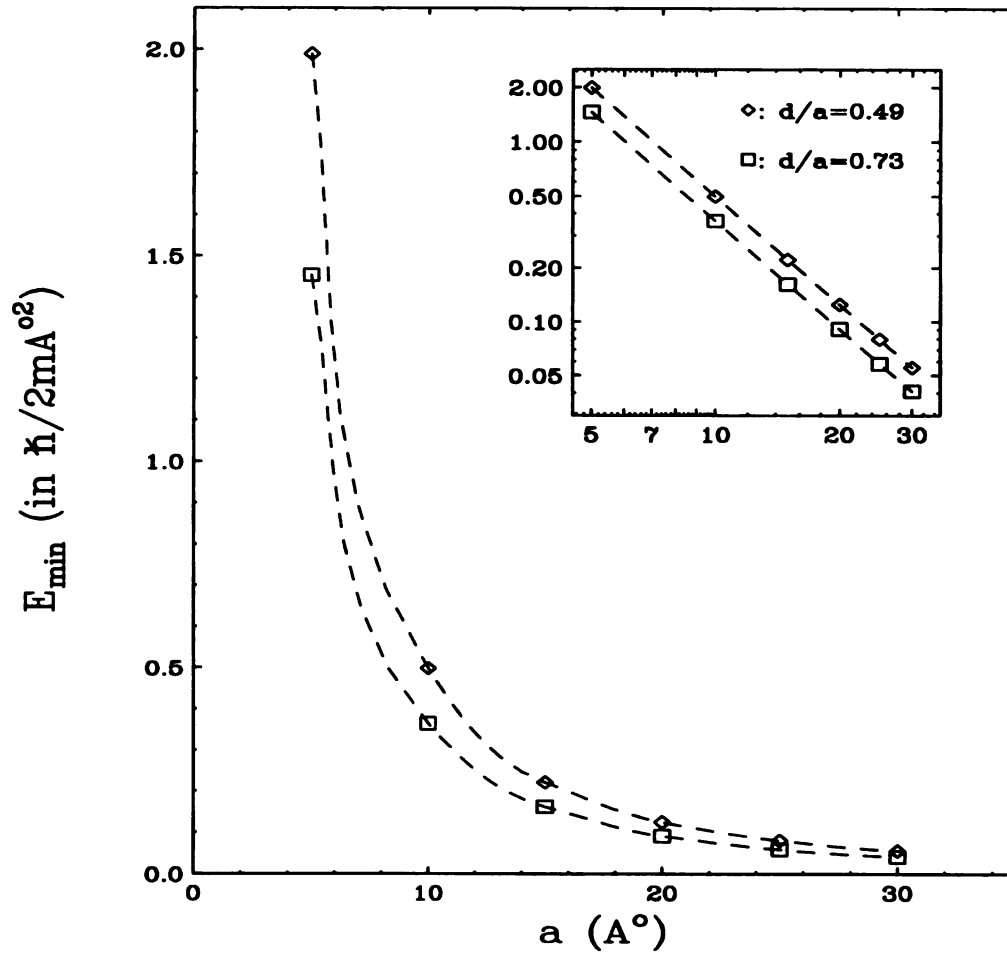


Figure 2.13: Ground state energy as a function of a . The insert is a log-log plot which shows $E_{\min} \sim a^{-2}$. Dashed lines are guide to the eyes.

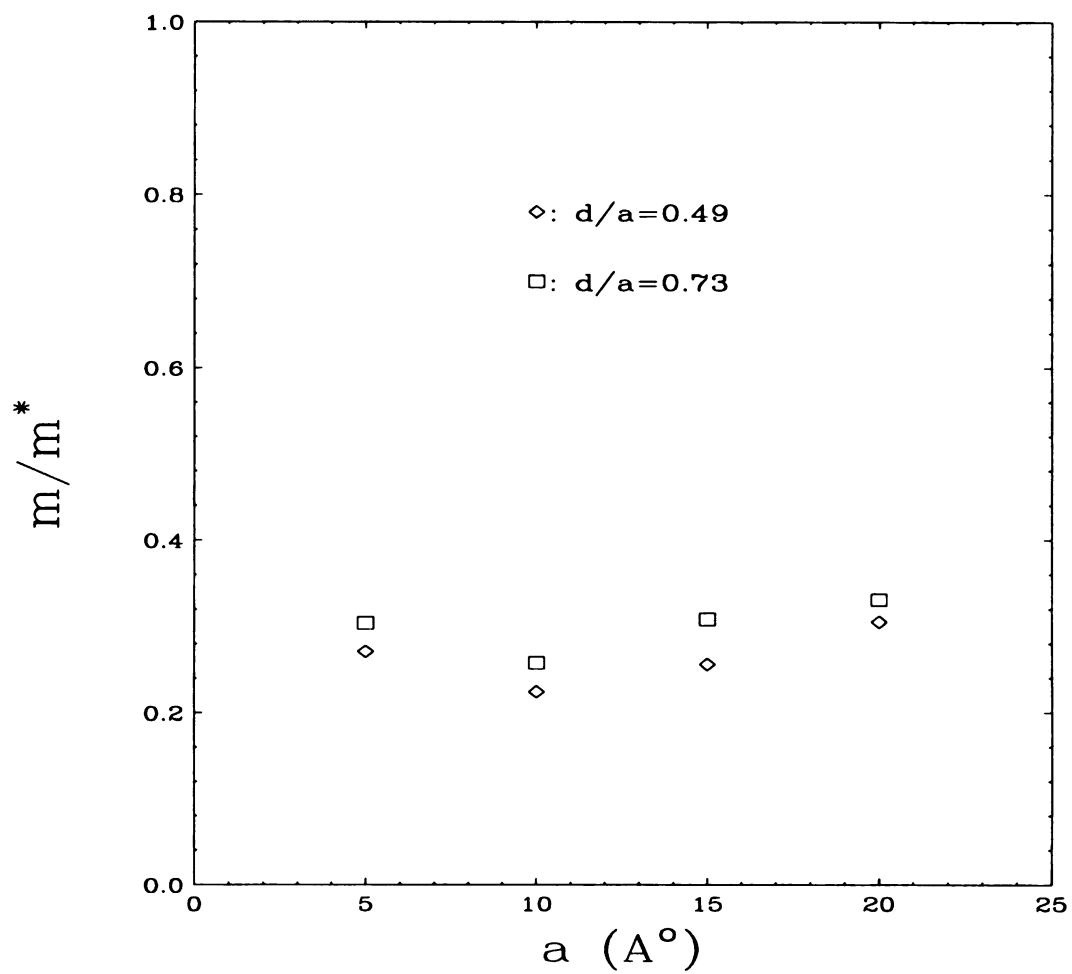


Figure 2.14: m/m^* as a function of a which shows that the effective mass ratio does not depend on a (b/a and c/a are fixed). The observed variations with a represents the inaccuracies in our calculation of m/m^* .

In fig. 2.15 we compare the results of Eqn. 2.3 with the numerically calculated values of m/m^* as a function of \bar{c} for two different values of \bar{d} ($=0.366, 0.512$). We see that the parameter α controls the sharpness of the rapid decrease in m/m^* as \bar{c} increases from 0. For large values of \bar{c} , m/m^* is relatively insensitive to α . In fig. 2.16, we give similar results but fix α and vary n . Clearly the m/m^* values depend sensitively on n as $\bar{c} \rightarrow 1$ and there is hardly any n -dependence for $\bar{c} < 0.4$. The parameters which fit our calculated results well are $\alpha = 18$ and $n = 4$. One can obviously fit the data better by increasing the number of parameters but one does not necessarily gain any additional insight.

2.3.3 Effects of attractive potential due to adsorbed ions on the cage surface and silicate framework

In many zeolites, there are positive ions distributed inside the structure which can provide additional attractive potential to the atoms moving in the channels. The nature of the attractive potential $V(\mathbf{r})$ produced by the positive ions on the channel wall and silicate framework depends sensitively on the location and number of positive ions inside the zeolite cage. As an example, let us discuss the case of K-L zeolite. Depending on the number of K^+ ions, there will be several minima in $V(\mathbf{r})$ as one goes around the wall of the cage. Fig. 2.17 shows the azimuthal potential distribution of K-L zeolite as the number of K^+ ions changes. To represent the general features of this ion-induced attractive potential, we add to the channel in fig.2.5 a potential of the form

$$V(r, \phi, z) = \begin{cases} -V_0 \frac{r}{(b/2)} \sin^2(p\phi), & 0 < z < c \\ 0, & \text{otherwise} \end{cases} \quad (2.4)$$

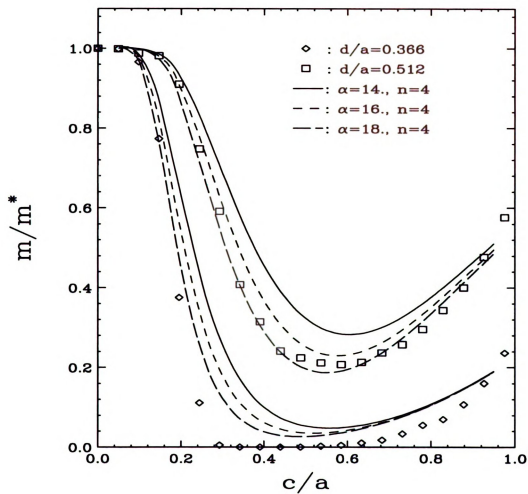


Figure 2.15: Comparison between the two-parameter function (Eqn.2.3) for m/m^* and the calculated m/m^* as a function of c/a for different values of d/a ; varying parameter α and fixing n .

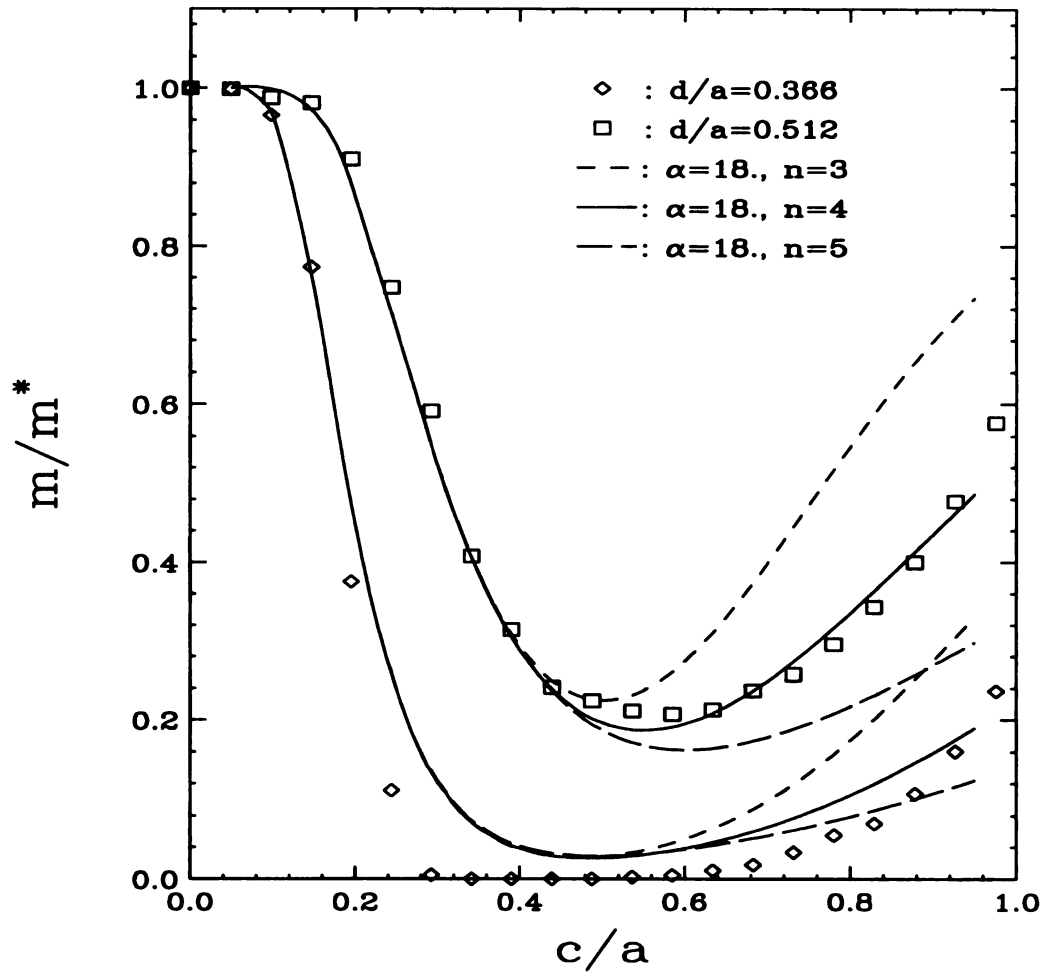


Figure 2.16: Comparison between the two-parameter function (Eqn.2.3) for m/m^* and the calculated m/m^* as a function of c/a for different values of d/a ; varying parameter n and fixing α .

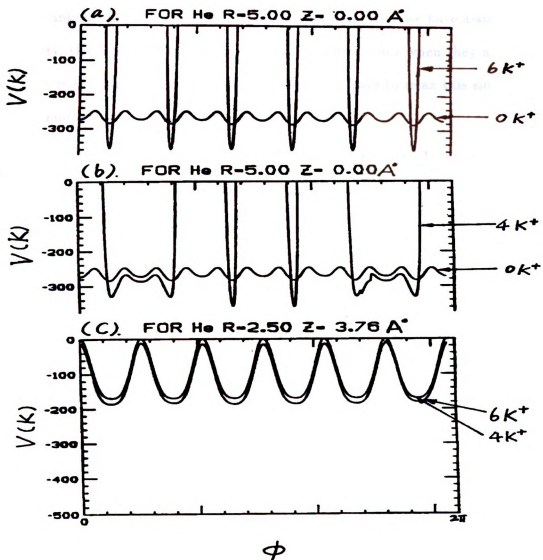


Figure 2.17: The azimuthal distribution of He - K-L zeolite potential with or without K^+ ions. (a) and (b) show the potential along the center of the channel wall. (c) shows the potential along the wall of neck. $0K^+$, $4K^+$ and $6K^+$ correspond to 0, 4 and 6 K^+ ions silicated on the cage wall, respectively.

In the above, r is the radial distance of the quantum particle, for example a He atom, from the axis of the tube, V_0 and p characterize, respectively, the strength and the angular periodicity of the attractive potential. Here we have assumed, for simplicity, that the K^+ ions do not affect the helium atoms when they are inside the neck region. In a more realistic model, one may have to relax this simplifying approximation.

In fig. 2.18, we plot the square of wave function for a particle moving inside a tubular channel as a function of the angle along the cage wall when the attractive potential in Eqn. 2.4 is present. In fig. 2.18a, we choose $p=2$ and $V_0 = 5e_0$. In fig. 2.18b, we choose $p=3$ and $V_0 = 5e_0$ but set two of the potential peaks zero. One can see very clearly that the quantum state of the particle depends very strongly on the potential shape.

To understand the full effect of the attractive potential, we have chosen as before $a = b = 10 \text{ \AA}$. We fix $c = 6 \text{ \AA}$, $d = 5 \text{ \AA}$, take $p = 2$ and vary V_0 in Eqn. 2.4. We find that when $V_0 = 0$, $m/m^* \simeq 0.19$, when $V_0 = 2e_0$ ($e_0 = \hbar^2/2m\text{\AA}^2$), $m/m^* \simeq 0.06$ and when $V_0 = 5.0e_0$, $m/m^* = 0.03$. Thus, an attractive potential produced by the cations located on the cage wall tends to increase the effective mass. The underlying physics is quite simple. When $V_0 = 0$, $m/m^* \ll 1$ indicating that inter-cage tunnelling rate is small. As we turn on V_0 , the particles get attracted towards the wall thus decreasing their inter-cage tunnelling probability and hence decreasing m/m^* . As V_0 becomes sufficiently strong, the particles get trapped near the cage wall and do not contribute to the mass transport along the tube axis. However, these trapped particles can dominate the low-T thermodynamic properties, particularly at low He concentrations as we will discuss in the following

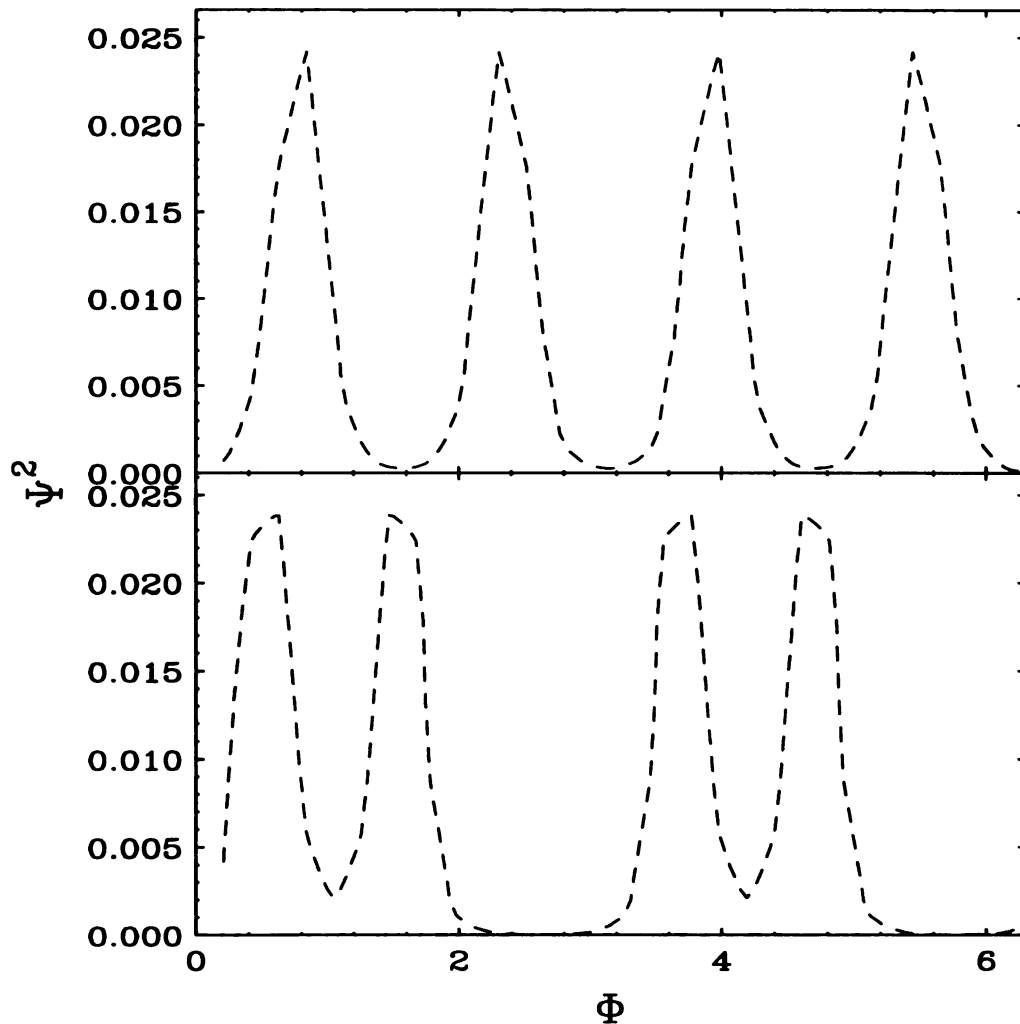


Figure 2.18: Square of the wave function (u^2) at $k = 0$ in the center of the channel as a function of azimuthal angle Φ with a fixed r . The channel parameters are: $a = b = 10 \text{ \AA}$, $c = 6.0 \text{ \AA}$ and $d = 5.0 \text{ \AA}$; (a). with attractive potential $p=2$ and $V_0 = 5.0e_0$ (b). with attractive potential, $V_0 = 5.0e_0$ and $p=3$ but two of the peaks in the potential were set to zero.

two chapters.

The square of wave function $u^2 \equiv \psi^2$ for $k = 0$ is plotted in fig. 2.19 for the three above values of V_0 . When $V_0 = 0$, the cage size is large enough such that the particle spends most of the time inside the cage ($m/m^* = 0.19$). However, u^2 is reasonably large near the tube axis indicating an appreciable inter-cage tunnelling probability. As we increase V_0 , u^2 near the cage axis tends to decrease and for $V_0 = 5.0e_0$, the particle spends most of the time away from the tube axis, i.e. they are trapped near the cage walls. In this case, inter-cage tunnelling is practically zero. The excitations of these particles then come from tunnelling around the cage wall, an intra-cage process.

2.4 Excited state

It is also interesting to investigate the excited energy bands and the wave functions. Since the method we used is good for only low-lying excited states (because of numerical accuracy), here we only present our results for a small number of these excited states. We show, in fig. 2.20, the ground state, the first and the second excited state energy bands for the 2D case with $a = b = 10 \text{ \AA}$, $c = 7.5 \text{ \AA}$ and $d = 5.0 \text{ \AA}$, and without the attractive potential. The unusual feature is the near absence of dispersion of the first excited state. Physically it means that if we can excite the particle from the ground state to the first excited state, the particle will get localized.

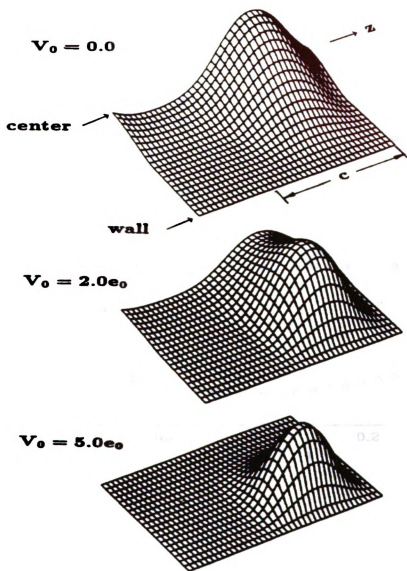


Figure 2.19: Square of the wave function (u^2) at $k = 0$. The channel parameters are: $a = b = 10 \text{ \AA}$, $c = 6.0 \text{ \AA}$ and $d = 5.0 \text{ \AA}$; (a). without the additional attractive potential ($V_0 = 0$); (b). with attractive potential, $V_0 = 2.0e_0$; (c). with attractive potential, $V_0 = 5.0e_0$. Here $e_0 = \hbar^2/2m\text{\AA}^2$.

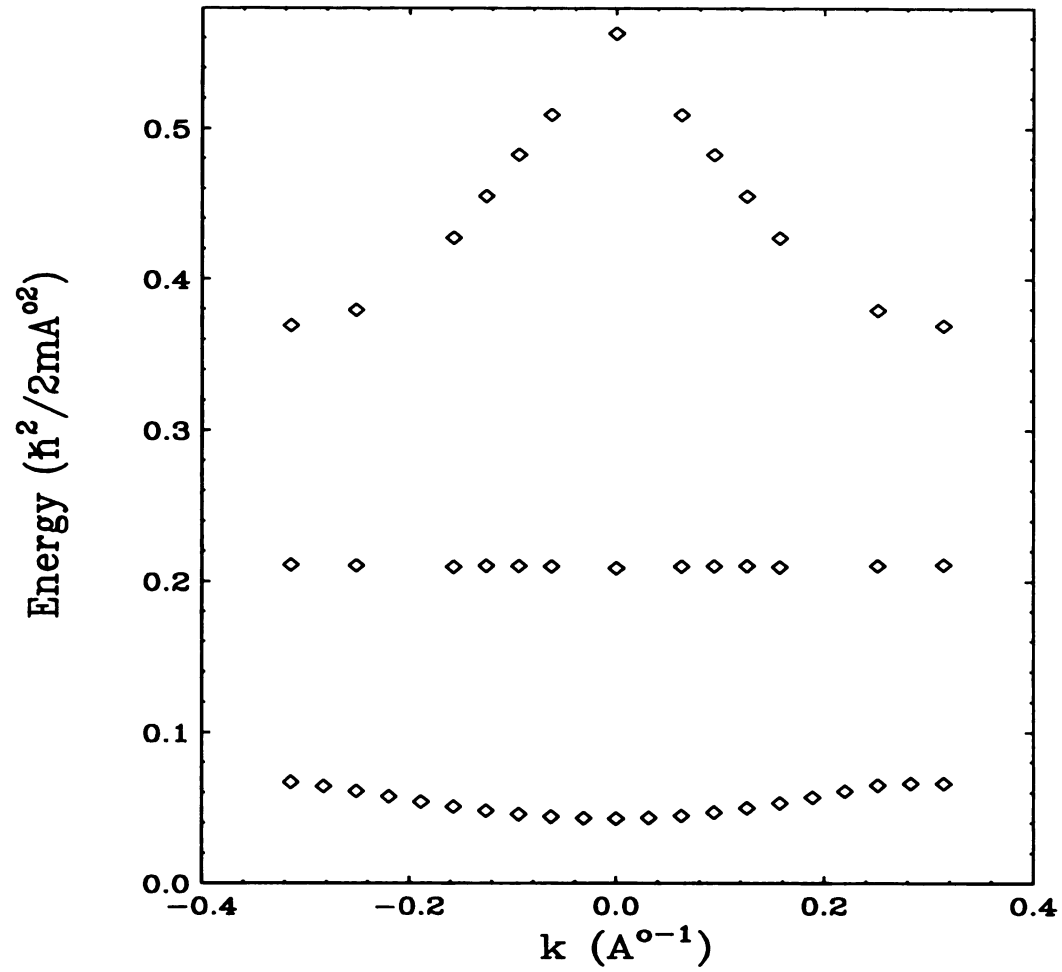


Figure 2.20: Energy bands for the ground state, first excited state and second excited state for 2D case with $a = b = 10 \text{ \AA}$, $c = 7.5 \text{ \AA}$ and $d = 5.0 \text{ \AA}$.

2.5 Summary

In summary, we have investigated the effects of geometrical confinement on the effective mass m^*/m of quantum particles moving along tubular channels. We find that m^*/m is a highly nonlinear function of the geometrical parameters such as cage size c/a and/or neck diameter d/a . There are large regions of parameter values where the m^*/m is quite large. Consequently any small perturbations like defects, scattering from thermal vibration of the wall or inter-particle interaction will have a strong effect on the mass transport along the channel axis. The effect of positive ions embedded in the channel walls can also be very significant. In particular, in the low helium atom concentration regime, helium atoms will be trapped in states near the wall with an extremely low probability of inter-cage motion. These states will not contribute to mass transport but will show up in low-temperature thermal excitations [44].

Chapter 3

Low-Temperature Thermodynamic Properties of Helium Clusters in K-L Zeolite

3.1 Introduction

Properties of ^4He and ^3He atoms confined to move in restricted geometry have been of considerable interest during the last several decades. Examples of confining media are Vycor [50], aerogels [67], zeolites [54]-[60], fullerites [61] and the surface of graphite [68]. Some of the basic questions that have attracted both theoretical and experimental attention include the nature of Bose-Einstein condensation in porous media (singly and multiply connected pore structure) [69]-[72], quantum transport through microporous channels [73], and the ground and excited states of quasi one-dimensional bosonic and fermionic quantum liquids, the so called Luttinger-liquids [74, 75, 76].

In chapter 2, we have discussed the nature of single particle states and the effective mass of transport (m^*) through a simplified 1-dimensional zeolite channel. We argued that in the presence of a strong attractive potential produced by

the ions located near the cage wall, the particle gets bound near the wall and the effective mass associated with intercage motion is large ($m^*/m \rightarrow \infty$). In this case the particles are trapped inside the cages and the motion is primarily along the cage walls perpendicular to the channel axis. In this Chapter, we discuss the results of our theoretical studies on the low-lying excitations of small numbers of ^4He and ^3He atoms (Helium clusters) tunneling inside a single cage of K-L zeolite along the cage wall. These low-lying excitations have been obtained using Bose-Hubbard (BH) and Mott-Hubbard (MH) models [44] with strong intrasite repulsion and finite intersite attraction. For small number of particles and at low enough temperatures, these systems can be represented by one-dimensional BH or MH rings containing a finite number of sites. Differences between ^4He and ^3He arise due to mass and statistics peculiar to the finite number of sites on the ring. We show how, in principle, these two effects can be disentangled. Calculated temperature and concentration dependences of the heat capacity agree qualitatively with experiment, but a quantitative comparison suggests that effects of disorder are extremely important at very low temperatures which will be discussed in the next chapter.

In section 3.2, we give a detailed description of the physical system and what is interesting to us. In section 3.3, we give some results from experiment done by Kato et.al. [58]. In section 3.4, we give the models that we have used based on the physics that we have described. Then, we give our numerical results in section 3.5 and compare our results with the experiments of Kato et.al. In section 3.6, we summarize our work.

3.2 Physical system

In chapter 2, we have shown a schematic picture of a typical K-L zeolite channel. In fig.3.1, we give a slightly different schematic picture of the cross-section of the one-dimensional channels of K-L zeolite. In this figure we also show a few He atoms trapped near the cage wall. The K-L zeolite crystal has a hexagonal lattice structure with lattice constants of $a = 18.4\text{\AA}$ and $c = 7.5\text{\AA}$, and it has one-dimensional channels along the c axis [58]. Each channel is composed of cages, about 13\AA in diameter and 7.5\AA in length. These cages are interconnected through apertures of diameter about 7.4\AA . On the cage walls there are K^+ ions (large circles in fig.3.1) which exert an attractive potential [43] on the He atoms in addition to the potential produced by the Si (Al) and O atoms of the zeolite network. Also the K^+ ions block the pathway for the He atoms connecting different channels. The potential produced by the zeolite cage gives rise to binding sites (in this case eight) for the He atoms; these binding sites (and associated localized cage states) are arranged in a ring geometry along the cage wall shown as small circles in the figure where we also indicate that some of these binding sites are occupied by He atoms (medium circles). Our aim is to develop a suitable theoretical model for this system and to understand how the difference in statistics (bosons and fermions) shows up both in the ground and excited states when the atoms are confined to move inside the cage in a ring geometry. But before that, we would like to briefly summarize the main experimental observations.

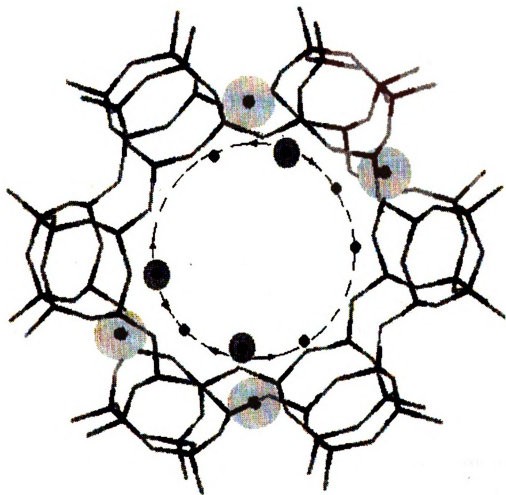


Figure 3.1: Schematic picture of a cross section of K-L Zeolite channel showing the silicate framework and ring arrangement of He adsorption sites (small circles). Large and medium circles are respectively K^+ ions along the channel walls and adsorbed He atoms.

3.3 Experimental results

Kato et.al. [58] have made detailed measurements of the low-T ($T < 5$ K) heat capacity of He atoms adsorbed inside K-L zeolite. Fig. 3.2(a) and (b) show their results of the heat capacities as a function of He concentration for fixed temperatures (fig. 3.2(a) is for ^4He and fig. 3.2(b) is for ^3He). Their results can be broadly divided into two regimes; regime 1 where $\langle n \rangle$, the number of He atoms/ cage $\leq n_c$, regime 2, $\langle n \rangle > n_c$. In regime 1, they find the following: (i) for fixed $T \leq 2\text{K}$, the heat capacity/atom, C vanishes at both $\langle n \rangle = 0$, and $\langle n \rangle = n_c = 8$ and is a relatively flat function of $\langle n \rangle$ between these limits. In this regime C is nearly symmetric about $n_c/2$ for ^3He but not so for ^4He . (ii) For a given $\langle n \rangle$, C is a monotonically increasing function of T . (iii) At same T and $\langle n \rangle$, C for ^3He is larger than that for ^4He by more than 25 %. A careful analysis of the experimental data suggest that in regime 1, He adatoms are trapped near the wall of the cage (we will denote it as cage state). The number of cage states is 8 per cage. In regime 2, where $n_c \ll \langle n \rangle < 12$, the excess He adatoms over n_c , i.e., $\langle n \rangle - n_c$, move along the channel axis in the presence of n_c He atoms bound in the potential minima of the cage, and behave as a one-dimensional quantum liquid [74]-[76]. When $\langle n \rangle$ is increased above about 15 atoms/cage, the heat capacities become small for both ^3He and ^4He . This indicates the freezing out of thermal motion of the He adatoms which form a solid-like structure.

In this chapter we study the thermal-excitations of He atoms in regime 1 where only the cage states which are localized along the cage walls are thermodynamically relevant.

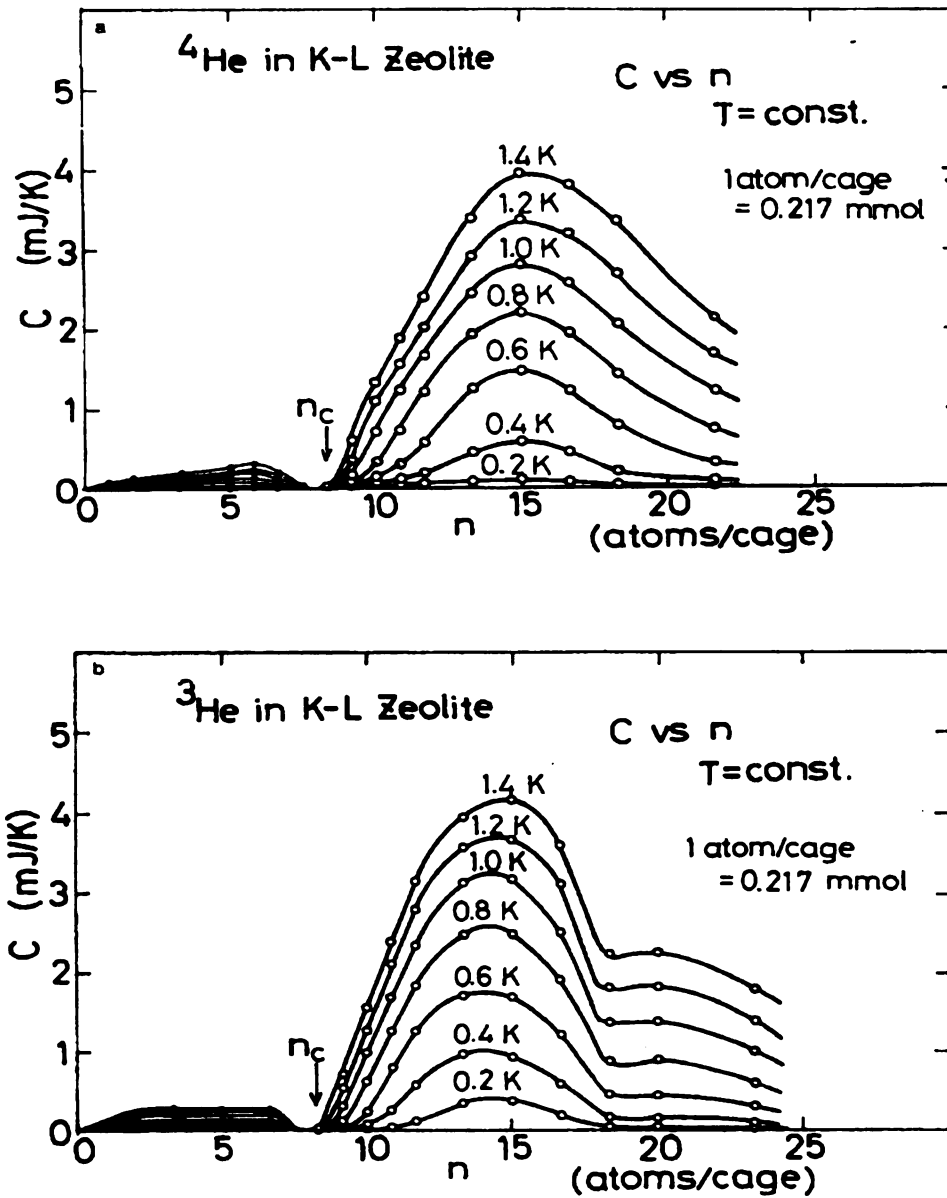


Figure 3.2: The experimental results of heat capacity of He atoms as a function of T for fixed He concentration $\langle n \rangle$ by Kato et.al. [58]

3.4 Models of the system

As discussed in the previous section, at low temperatures ($T < 10\text{K}$) and for sufficiently small concentration n , He atoms are bound near the wall of the K-L zeolite cage. The probability of He atoms going from one cage to another is extremely small because the barrier for this inter-cage motion is estimated to be about 150K from the isosteric heat measurements [58]. The dominant mode of thermal excitation at low- T is therefore tunneling from one binding site to another inside a single cage. These bound states are referred to as the cage states [43]. When n is increased beyond a critical value n_c , n_c He atoms fill up all the cage states and the additional $n - n_c$ atoms move in the region near the cage axis and go from one cage to another. These states will be referred to as the channel states. Of course, at higher temperatures, the atoms trapped in the cage states get thermally excited to the channel states and undergo intercage motion. As has been stated above, our interest is to study the thermal-excitations of low-temperature cage states. Our model is designed to study this low temperature ($T < 10\text{K}$) behavior of ^3He and ^4He in the concentration regime $0 \leq n \leq n_c$. At these temperatures, the channel states are practically unoccupied and one has to deal with the statistical mechanics of cage states only.

The excitations of the ^4He system in the manifold of cage states can be described by an extended Bose-Hubbard model[44, 71, 72]. The Hamiltonian for this model is given by

$$H = -t \sum_{i=1}^{N_m} (b_i^\dagger b_{i+1} + h.c.) + \frac{U}{2} \sum_{i=1}^{N_m} n_i(n_i - 1) + V \sum_{i=1}^{N_m} n_i n_{i+1}, \quad (3.1)$$

where N_m is the number of binding (localized) sites which equals to 8 for the

present case, b_i (b_i^\dagger) destroy (create) a boson (B) at the i th localized site, U is the repulsive energy between two He atoms occupying the same binding site and V is the attractive energy between two atoms occupying neighboring sites. The boson creation and destruction operators satisfy the usual commutation rules and the number operator for the i^{th} site n_i has eigenvalues 0,1,2, etc.

The ${}^3\text{He}$ system is similarly described by an extended Mott-Hubbard model [40, 44] and the corresponding Hamiltonian is given by

$$H = -t \sum_{i,\sigma}^{N_m} (f_{i\sigma}^\dagger f_{i+1\sigma} + h.c.) + U \sum_i^{N_m} n_{i\uparrow} n_{i\downarrow} + V \sum_{i=1}^{N_m} n_i n_{i+1} \quad (3.2)$$

Here the fermion destruction ($f_{i\sigma}$) and creation ($f_{i\sigma}^\dagger$) operators associated with state i and spin σ satisfy the usual anti-commutation rules and $n_{i\sigma}$ can have eigenvalues 0 or 1. The total number of fermions at site i is $n_i = n_{i\uparrow} + n_{i\downarrow}$. Since the spin exchange energy is quite small (about $t^2/U \sim 0.01K$), we first ignore the spin degrees of freedom of the ${}^3\text{He}$ atoms and treat them as spinless fermions (SF's) and later we will discuss the effects of including spin on the many-particle energy spectrum in the limit of large U . In fact, He-He repulsion is quite strong when two atoms occupy the same binding site, we therefore let $U \rightarrow \infty$. Then, n_i can have eigenvalues 0 or 1 for both bosons and fermions. In this limit both B and SF systems can be described by a single Hamiltonian.

$$H = -t \sum_{i=1}^{N_m} (c_i^\dagger c_{i+1} + h.c.) + V \sum_{i=1}^{N_m} n_i n_{i+1} \quad (3.3)$$

where $c_i = b_i(f_i)$ and $n_i = c_i^\dagger c_i = 0$ and 1.

This hamiltonian can be diagonalized exactly numerically for different values of N_m and $n = \sum_{i=1}^{N_m} n_i$. The heat capacity is then calculated by using the fluctuation-

dissipation theorem:

$$C(n, T) = \frac{1}{kT^2} (\langle E(n, T)^2 \rangle - \langle E(n, T) \rangle^2), \quad (3.4)$$

where

$$\langle E(n, T) \rangle = \frac{\sum_j E_j e^{-\beta E_j}}{\sum_j e^{-\beta E_j}},$$

and

$$\langle E(n, T)^2 \rangle = \frac{\sum_j E_j^2 e^{-\beta E_j}}{\sum_j e^{-\beta E_j}}$$

The summation goes over all the energy levels of the n particle system.

3.5 Results for Bosons (B) and Spinless fermions (SF)

3.5.1 Difference between B and SF due to statistics

Although the Hamiltonians for B and SF have the same form, the differences between B and SF cases lie in the commutation properties of the operators and the transfer energy t arising from the ${}^3\text{He}$ and ${}^4\text{He}$ mass difference. For the same t and V , the spectrum of bosons and spinless fermions are identical for an open chain [77]. For the ring geometry, the statistics induced differences between B and SF systems can be seen by writing down the Hamiltonian matrix in localized (on the ring sites) representation. We denote the system of N_m sites and n particles

as (N_m, n) . For the same t and V , one gets identical matrices for the two systems when n is odd [77]. Therefore, the corresponding energy spectra and C are also identical. However, when n is even, they differ considerably. For example, the hamiltonians for 4 site 2 particle systems are:

$$H_B = \begin{pmatrix} V & 0 & 0 & 0 & t & t \\ 0 & V & 0 & 0 & t & t \\ 0 & 0 & V & 0 & t & t \\ 0 & 0 & 0 & V & t & t \\ t & t & t & t & 0 & 0 \\ t & t & t & t & 0 & 0 \end{pmatrix}$$

whereas

$$H_{SF} = \begin{pmatrix} V & 0 & 0 & 0 & t & -t \\ 0 & V & 0 & 0 & t & t \\ 0 & 0 & V & 0 & -t & t \\ 0 & 0 & 0 & V & -t & -t \\ t & t & -t & -t & 0 & 0 \\ -t & t & t & -t & 0 & 0 \end{pmatrix}$$

Thus, in addition to the mass difference, the different statistics can give rise to differences in the heat capacity of the ${}^3\text{He}$ and ${}^4\text{He}$ systems in this ring geometry due to the difference in energy spectrum for even- n values. In fact we will argue that the difference in the statistics can explain the observed [58] trend in C whereas the mass difference goes the other way.

An example of the energy spectrum is shown in fig.3.3 for the system (8,4). It has $8!/4!x4! = 70$ states. If t is finite and $V=0$, then the SF states can be obtained simply by singly occupying the one particles states $k_i = (\pi/4)(0, \pm 1, \pm 2, \pm 3, 4)$ with energy $-2t\cos k_i$. But if $V \neq 0$, one must diagonalize the 70×70 matrix. The lowest 20 states for both $V = 0$ and $V \neq 0$ are shown in fig.3.3. It shows that

the energy spectrum depends sensitively on both the statistics and the intersite attraction. One characteristic feature of these results is that for SF, each energy level is $2n$ -fold degenerate whereas for B, the levels can be both $2n$ and $2n+1$ -fold degenerate.

In fig.3.4, we show the T-dependence of the molar heat capacity $N_A C(n, T)/n$ for the $N_m = 8$ system for different even values of n . Here, N_A is the Avogadro's number. Bosons are found to have much smaller heat capacity than spinless fermions. The reason for this result is that for the same t and V , the lowest energy gap for the bosons is found to be considerably larger than that for the spinless fermions whereas the ratio of the degeneracy of the first excited state to the ground state is 2 for both the systems. (For odd n , B and SF systems have identical heat capacity). We suggest that one should be able to see this difference between even and odd- n systems experimentally. In fact, one can use the odd n results to extract the effect of mass difference (through t) and in principle disentangle the effects of mass and statistics on the heat capacity. In practice this is not easy because due to fluctuations in n from one cage to the other [58], one usually measures C as a function of average n .

3.5.2 Difference between B and SF due to mass

To see the difference between B and SF due to mass, we choose boson statistics and vary the t parameter (which depends on the mass). Fig. 3.5 shows the heat capacities for a (8,4) system with bose statistics and two different values of the tunnelling parameter t . It can be seen clearly that when t is small, i.e. when the mass is large, the heat capacity is large. The same qualitative results are obtained using fermion statistics. This means that if only mass difference is taken into

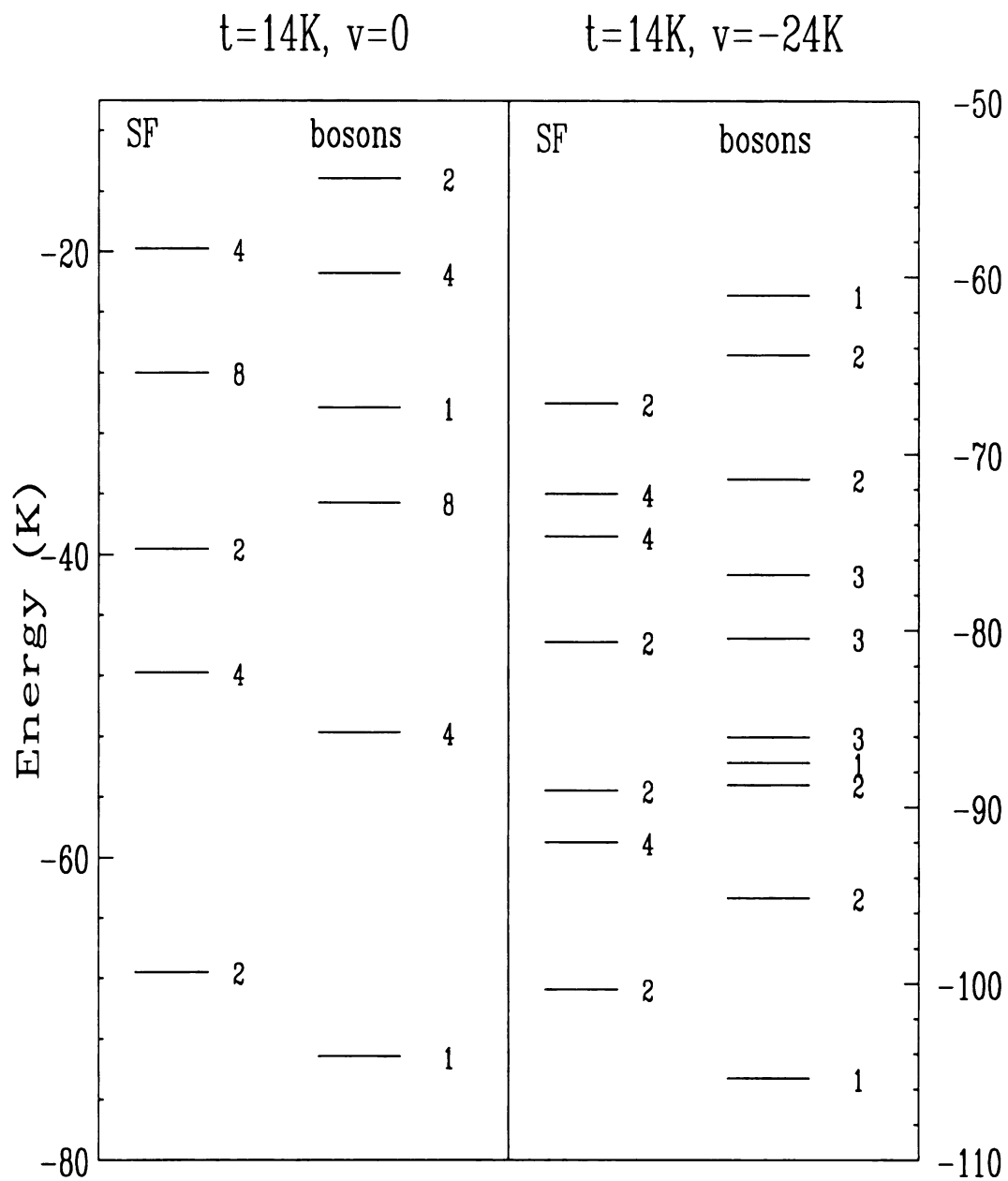


Figure 3.3: Lowest 20 (out of 70) energy states of spinless fermions (SF) and bosons (B) for particles in a 8-site ring. The hopping parameter $t = 14K$ and the intersite attractive interaction V is $0K$ and $-24K$, $U \rightarrow \infty$. The numbers besides the energy levels indicate their degeneracy.

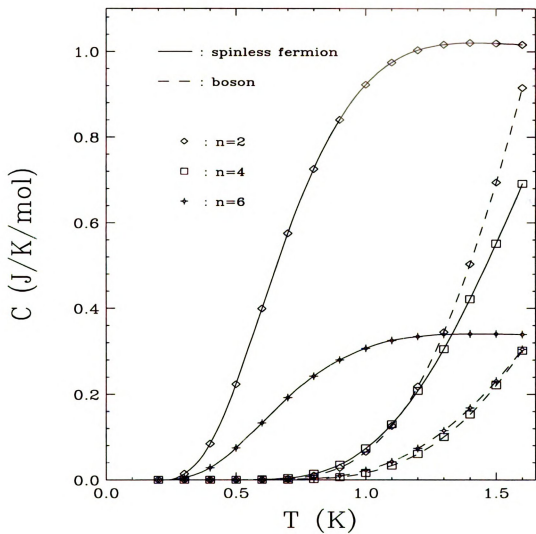


Figure 3.4: Temperature dependence of the molar heat capacity for 8-site n -particle spinless fermion and boson systems. The parameter values are $t = 14K$ and $V = -24K$. (For a discussion of the parameter values, see text)

consideration, the heat capacity of ${}^4\text{He}$ should be larger than the heat capacity of ${}^3\text{He}$.

3.5.3 Comparison with experiments

To compare our theoretical results with experiments of Kato et.al. [58] we note that C was measured as a function of $\langle n \rangle$, where $\langle n \rangle$ is the mean occupation number of atoms/cage. In order to obtain a uniform distribution of He atoms inside different cages, Kato et.al. [58] heated the system to a temperature T_o in order to facilitate a nearly uniform density of He atoms throughout the system and then measured $C(\langle n \rangle, T)$ vs T at $T \ll T_o$. At $T < 2\text{K}$ where C was measured, the intercage equilibration is extremely slow. We therefore assume that

$$C(\langle n \rangle, T) = \sum_{n=0}^8 C(n, T)P(n, T_o), \quad (3.5)$$

where

$$\langle n \rangle = \sum_{n=0}^8 nP(n, T_o),$$

and

$$P(n, T_o) = \frac{Z(n, T_o)z^n}{L(z, T_o)},$$

$$L(z, T_o) = \sum_{n=0}^8 Z(n, T_o)z^n,$$

$$z = e^{\beta_o \mu} = e^{\mu/k_B T_o}.$$

where μ is the external chemical potential. In other words, the distribution $P(n, T_o)$ of He atoms in different cages is governed by the quenching temperature T_o (\cong

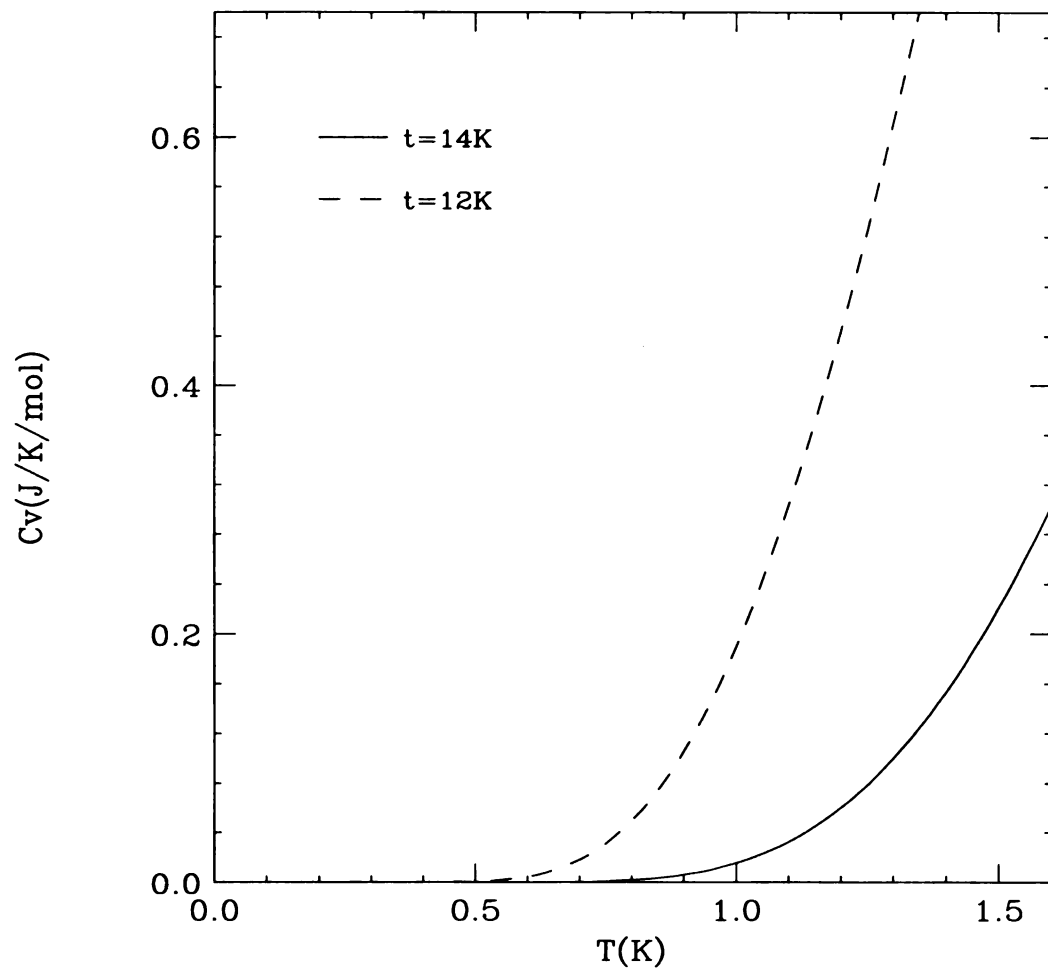


Figure 3.5: The molar heat capacity for the (8,4) system with Bose statistics and different t , $V=-24\text{K}$.

20K in the experiment of Kato et.al. [58]) whereas C is measured at temperatures $T \ll T_o$. At these T , different cages have different number of He atoms, this distribution corresponds to the higher temperature T_o .

As regards the parameter values, we have estimated (see appendix A) V to be about -20K to -25K. A large component of this attraction comes from the 3-body He- K^+ -He interaction. The hopping parameter t was chosen such that the heat capacity for both the He systems is of the same order as the experiment ($\simeq 0.6\text{J/K/mol}$ at $T \simeq 1.5\text{K}$). We have fixed $t=14\text{K}$ and $V=-24\text{K}$ for our numerical calculation of C . The bandwidth $W=2t$ is of the same order as the magnitude of V . With the same parameter values, i.e. when the mass effect is not taken into account, we calculate C for both ^3He and ^4He systems. The effect of mass difference will be commented upon later.

For comparison with the experimental results [58], the computed theoretical values of C (heat capacity/atom) multiplied by a constant, which the experiment gives as 1 atom/cage=0.217mmol. Fig.3.6(a) gives the theoretically calculated values of $C(\langle n \rangle, T)$ as a function of $\langle n \rangle$ and T for three different T values for the spinless fermions. As expected, $C = 0$ when $\langle n \rangle = 0$ and 8 when the sites are either all empty or full. The rapid increase in C as one moves away from these two limits and a relatively flat structure of C for $2 < \langle n \rangle < 6$ is reproduced nicely in our calculations. The theoretical values agree well with experiment at 1.5K but are about 30 % smaller at lower temperatures. Fig. 3.6(b) gives the heat capacity vs. T curve for fixed $\langle n \rangle$. The insert is the experimental results. Our calculated results have captured the main features of this system although we still have some discrepancies at very low- T . Fig. 3.7 shows the discrepancies between

experimental and our results.

For the bosons, we also see a similar n -dependence but with the choice of the same parameter values, the theoretical values of C are much too small compared with the experiment (see fig. 3.8). Also, for the bosons, a small particle hole asymmetry is observed [58] in the experiment whereas our model has in-built particle-hole symmetry. Our calculated C drops much faster with T compared to the experiment and for $T < 0.75\text{K}$, the theoretical values are practically zero. A plausible reason for this may be that the value of t is too large. Since ${}^4\text{He}$ is heavier than ${}^3\text{He}$, we expect the value of t to be smaller for ${}^4\text{He}$. This will reduce the excitation energy and hence increase the low- T heat capacity. For example, for the system (8,4), if we choose $t=12\text{K}$ instead of 14K , the lowest energy gap (Δ) changes from 10.3K to 7K . This reduction in Δ increases the heat capacity at 1K from 0.015 to 0.189 J/K/mol, an increase by nearly a factor of 10. We find that for $\langle n \rangle = 1.67$, our theoretical value is 0.344 J/K/mol compared to the experimental value of 0.4 J/K/mol. However, the theoretical values are still too small at temperatures less than 0.5K . From the above discussions, we see that (i) the difference in statistics leads to a larger heat capacity for the *spinless fermions* whereas the mass difference, through a smaller excitation energy gap, leads to a larger heat capacity for the *bosons*, and (ii) theoretical values are smaller than experiment at very low T .

3.5.4 Spin effect

In the above sections, we have neglected the spin of ${}^3\text{He}$ and treated them as spinless fermions. In this section, we will discuss the effect of including spin of ${}^3\text{He}$ on the low- T heat capacity. Inclusion of spin for ${}^3\text{He}$ dramatically increases the

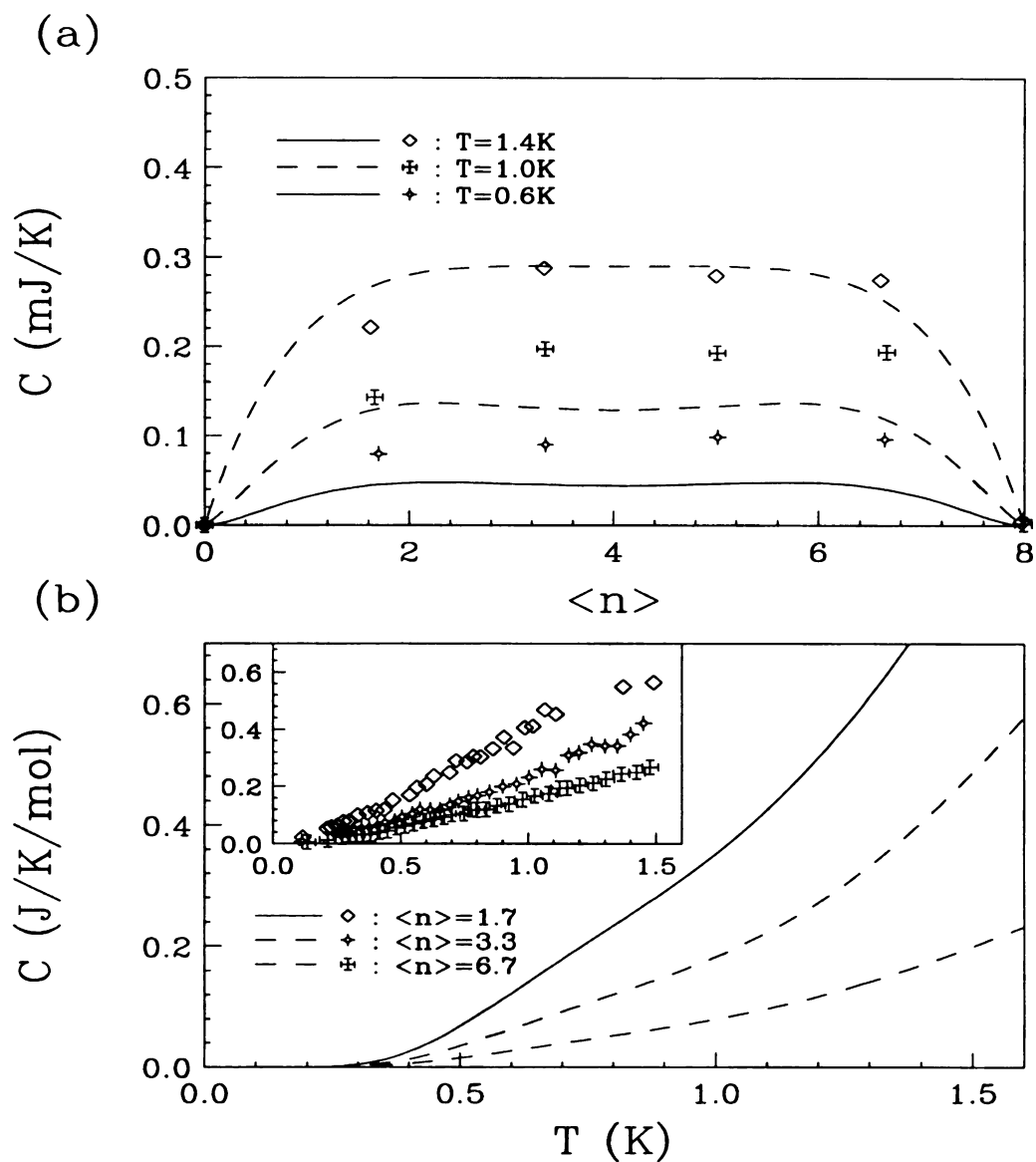


Figure 3.6: (a).Heat capacity for the spinless fermions as a function of $\langle n \rangle$, average number of particles per cage, at three different temperatures. The symbols are experimental values for ^3He . Theoretical values have been obtained using $t = 14\text{K}$ and $V = -24\text{K}$. (b).Temperature dependence of the heat capacity for spinless fermions for three different values of $\langle n \rangle$, average number of particles per cage. In the insert we give the experimental results for ^3He obtained by Kato et.al. [58]

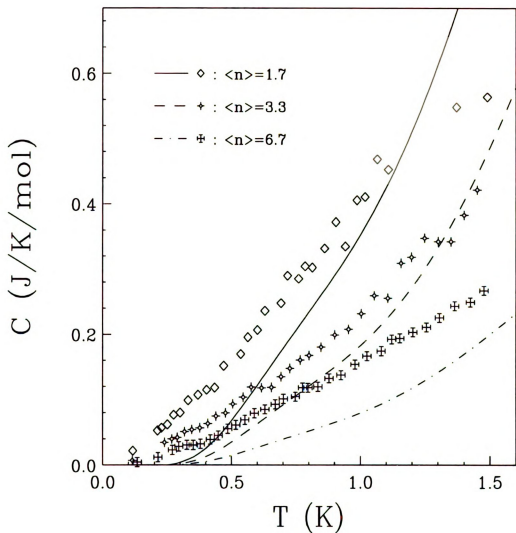


Figure 3.7: Temperature dependence of the heat capacity for spinless fermions for three different values of $\langle n \rangle$, average number of particles per cage. which shows the differences between our calculated results and the experiments by kato et.al. [58].

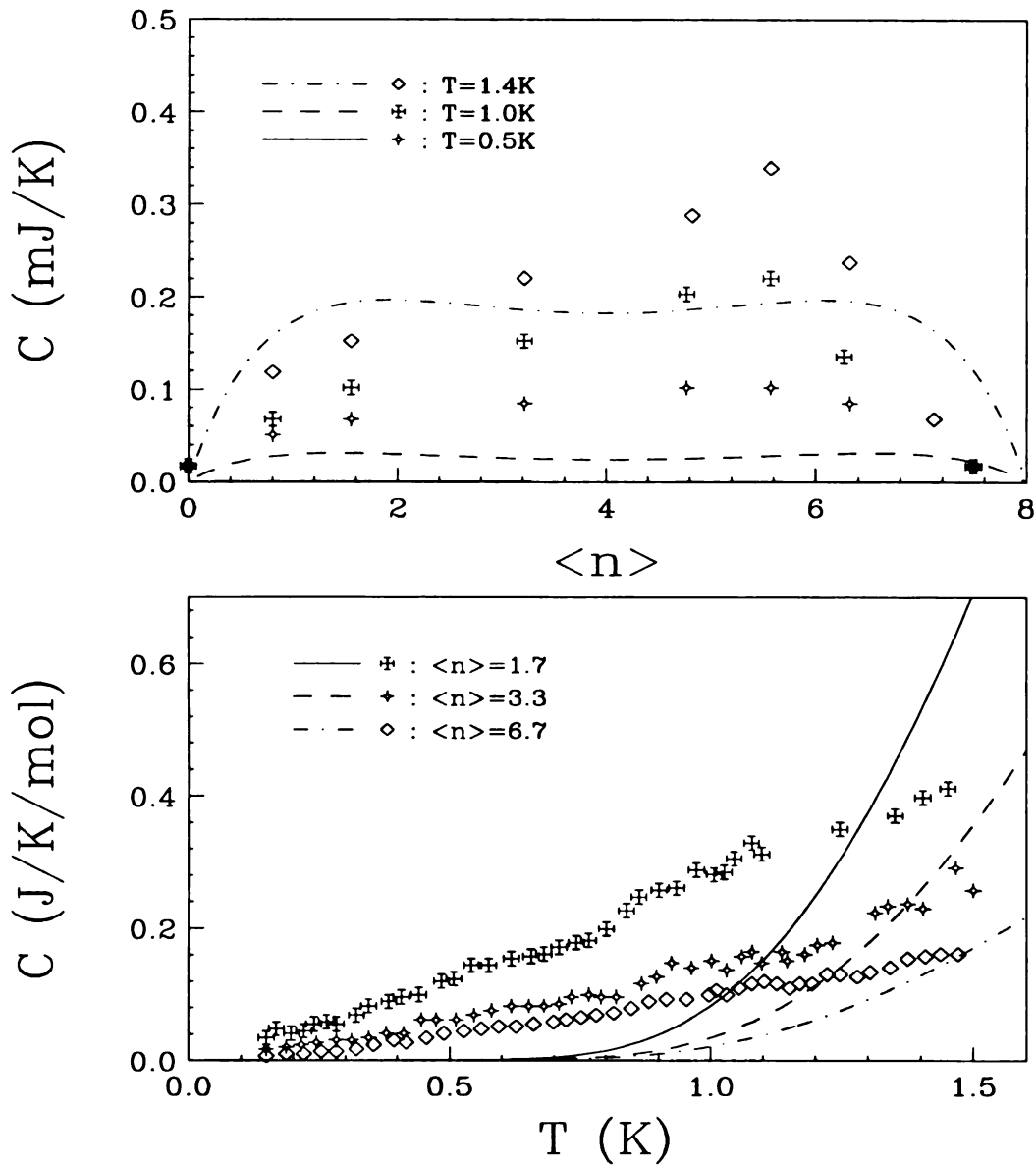


Figure 3.8: (a).Heat capacity for the bosons as a function of $\langle n \rangle$, average number of particles per cage, at three different temperatures. The symbols are experimental values for ${}^4\text{He}$. Theoretical values have been obtained using $t = 14\text{K}$ and $V = -24\text{K}$. The values for $T=0.5\text{K}$ are very small to be plotted. (b).Temperature dependence of the heat capacity for bosons for three different values of $\langle n \rangle$, average number of particles per cage. The symbols give the experimental results for ${}^4\text{He}$ obtained by Kato et.al. [58]

dimension of the Hilbert space. For example, if we include spin in the system (8,4), the manifold of states we have to consider is 1120 instead of 70 for the spinless fermions. But, if the spin and translational degrees of freedom had decoupled [78] (spin-charge separation) as in the case of an open chain geometry or an infinite system (both with $U = \infty$), then the T-dependence of C would have been identical for the SF and fermions excepting for a delta function at $T = 0$ for the latter; the total number of states associated with this peak being $2^4 = 24$ for the open chain with 4 particles. On the other hand, for the ring geometry, the spectrum of SF and fermions differ from each other and in principle the heat capacities should be different. Furthermore, for fermions, one has to take into consideration the thermal equilibration between states differing in total spin quantum number as in the classic ortho and para hydrogen (H_2) problem [79, 80]. Computations in the (8,2) and (8,3) systems suggest that, after taking into account the above thermal equilibration (or lack there of) between manifold of states with different total spin quantum numbers, the heat capacities for the SF and fermion systems are comparable. In fig.3.9, we see that for the (8,2) and (8,3) systems, the T-dependence of the heat capacities have similar behavior for SF and F and, $C(2,T)$ for F is smaller but $C(3,T)$ for F is larger compared to the corresponding SF values. Thus we expect that inclusion of spin and averaging over n will not change $C(\langle n \rangle, T)$ very much. However we have not done this averaging for the spinful fermions because of our lack of any detailed knowledge of the equilibration problem (as in the case of ortho and para hydrogen).

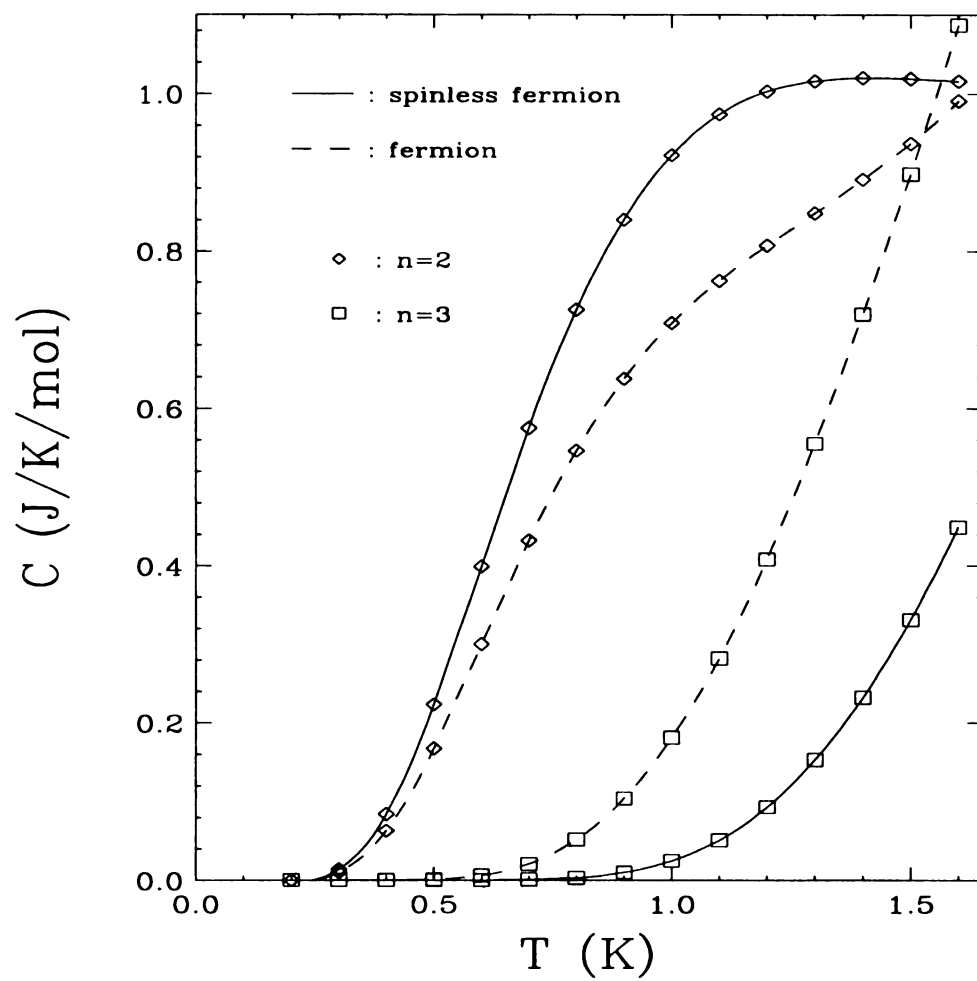


Figure 3.9: Comparison of the heat capacity between SF and F for (8,2) and (8,3) systems. $t=14K$, $V=-24K$.

3.6 Conclusion

In summary, we have shown that the low-T thermodynamic properties of ^3He and ^4He atoms trapped inside the cages of K-L zeolite can be modeled by Mott (Bose)-Hubbard rings. The ring geometry brings out nicely the differences between bosons, spinless fermions and fermions. This behavior should be characteristics of He atoms trapped inside other zeolitic cages such as Na-Y zeolite [55, 56]. The disagreement between theory and experiment at very low temperatures (both for SF and B, particularly for the later) suggests that at very low T, effects of disorder might be important, we therefore explore the effect of disorder next.

Chapter 4

Effect of Tunneling Disorder on the Low Temperature Heat Capacity of ^3He and ^4He in Zeolite Channels

4.1 Introduction

In the last chapter, we argued that the thermal excitation inside K-L zeolite of He system within the manifold of the cage states (for $n < n_c$) can be described by Bose-Hubbard (for ^4He) or Mott-Hubbard (for ^3He) model with binding sites localized on a ring. As pointed out before, the K^+ ions located close to the cage walls and the silicate network provide the potential in which the He atoms are bound. But the K^+ ions are not necessarily situated symmetrically around the ring. As a matter of fact, there are six equivalent sites available for the K^+ ions and a maximum of only four K^+ ions are available per cage to occupy these sites randomly. In addition there is disorder in the silicate framework because some of the silicon ions are randomly replaced by aluminum ions and K^+ ions not located near the cage wall are also randomly distributed inside the silicate

framework. This random distribution of the ions can give rise to disorder in the physical parameters of the Hubbard-type models describing the excitations of the He system, namely the single-site binding energy, inter-site tunnelling matrix elements (also called hopping parameters), etc. Consequently the low temperature heat capacity will be affected by the disorder. In this chapter, we introduce the effects of disorder in our model by treating the hopping parameters as random variables and computing the average heat capacity of the He system using different probability distributions.

The presence of disorder in the model, as noted in chapter 3, is expected to improve agreement of the computed results with experiment. This is so because the system without disorder has low-lying energy levels which are discrete (due to the small size) and separated from one another. Suppose the lowest energy gap is Δ . Then, the heat capacity of the system must exhibit Schottky-type of anomaly [81], leading to an exponentially decreasing heat capacity at temperatures $T \ll \Delta/k_B$. In the present case, the discrete energy levels of the system calculated in chapter 3 lead to $\Delta/k_B \geq 5K$. Hence one gets vanishingly small heat capacity at temperatures below 0.5K. In the presence of disorder the low lying excitation spectrum should be drastically modified and we expect an increase in the density of low energy excitations arising primarily from the region of smaller hopping parameters. This should result in an enhancement of the heat capacity at low temperatures when a proper averaging over the various disorder states is performed.

Before discussing our model and results, we would like to briefly review the models of disorder which have been proposed to explain the enhanced heat capac-

ities seen in glasses (disordered insulators) at low temperature. A rather simple model was proposed by Kaplan, Mahanti, and Hartmann (KMH) [82] within the context of the standard Hubbard model with its three characteristic parameters; single-site energy (ϵ), tunnelling matrix element (t), and intra-site Coulomb interaction (U). In the KMH model, the single-site energies (ϵ_i) are assumed to be random, $t = 0$, $U = \text{constant}$. For a continuous distribution of ϵ_i one obtains a heat capacity linear in T at low T . In the context of Hubbard-type models, our present work is an extension of the KMH model taking into account a finite but random t , constant ϵ_i , $U = \infty$, and a finite inter-site Coulomb interaction V . The most general case is however when all the parameters of the Hamiltonian are random.

Although mathematically our present model is an extension of the KMH model [82], physically it is much closer to the one proposed by Anderson, Halperin, and Varma (AHV) and [83] by Phillips [84]. This model was proposed to explain the observed low-temperature specific heat varying linearly with T in a variety of insulating glasses. The essence of the model was the hypothesis that in any glass system there should be a certain number of atoms (or group of atoms) which can sit more or less equally in two or more equilibrium positions. The thermal excitation between the associated localized ‘tunnelling levels’ leads to a Schottky-type heat capacity with a characteristic energy Δ . A statistical distribution $P(\Delta)$ of these localized tunnelling levels (LTL’s) gives a linear heat capacity at low T . Although this model describes the correct physics of the observed large low- T heat capacity in insulating glasses, a microscopic picture of these LTL’s is not easy to come by [85]. Our model of Helium atoms trapped inside zeolitic cages with random tunnelling matrix elements indeed gives one possible microscopic picture

of these LTL's.

It is in general quite difficult to compute thermodynamic quantities by introducing disorder in the Hamiltonian and then averaging over the disorder. The ring geometry with a small number of sites in the present problem leads to some simplifications, but even then, the computations are quite involved. Therefore, only some calculations illustrating the important trends at low temperatures are presented below. Nevertheless, the numerical evaluation of the effect of disorder by introducing randomness and computation of the average heat capacities is an important feature of the present work. It must be emphasized that the aim of our work is to show the improvements in the computed low temperature specific heat vis-a-vis experiment by including disorder rather than fitting the experimental results accurately.

4.2 Model with disorder

Disorder in the system can arise due to various reasons. One reason could be the random occupation of K^+ ion sites by the ions. Distortions, imperfections etc would give rise to additional disorder. In terms of the Hamiltonian, there can be randomness in the single-site energies, tunneling parameter t , the attractive potential V and the intrasite repulsion U . We consider only the disorder in the tunneling parameters and take single site energies to be zero. Then, the Hubbard Hamiltonian in the limit $U \rightarrow \infty$ may be written as

$$H_{B(SF)} = - \sum_{i=1}^{N_m} t_i (c_i^\dagger c_{i+1} + h.c.) + V \sum_i^{N_m} (n_i n_{i+1}), \quad (4.1)$$

where the tunneling parameters are random numbers which follow some distribution function $f(t_i, \sigma)$, with σ defining the width of the distribution. Note that the

number operator n_i has eigenvalues of 0 or 1 in the case of both bosons (B) and spinless fermions (SF) since the intra-site repulsion energy $U = \infty$.

The heat capacity for a set of $\{t_i, i=1, \dots, N_m\}$ can be obtained as before through

$$C(n, T, \{t_i\}) = (\langle E^2 \rangle - \langle E \rangle^2) / kT^2. \quad (4.2)$$

Here, the thermal averaging is done with the help of the exact partition function. Next, one must perform the configurational averaging for disorder. We have chosen both uniform and gaussian distributions but will report the results for the latter. The gaussian distribution for the random tunneling parameters is giving:

$$f(t_i, \sigma) = \frac{1}{\sigma\sqrt{\pi}} e^{-(t_i - t_0)^2 / \sigma^2}. \quad (4.3)$$

These distributions are symmetric around $t_i = t_0$. The heat capacity for the canonical ensemble may be configurationally averaged over the disorder and the concentration distributions as follows:

$$C(n, T) = \sum_{n=1}^8 \int_{-\infty}^{\infty} \dots \int_{-\infty}^{\infty} C(n, T, \{t_i\}) P(n, T_o, \{t_i\}) f(t_1, \sigma) \dots f(t_{N_m}, \sigma) dt_1 \dots dt_{N_m} \quad (4.4)$$

For simplicity, in the numerical calculations we have assumed that $P(n, T_o, \{t_i\}) = P(n, T_o, \{t_0 \forall i\})$. In this way, we can separate these two averages. The integration is performed numerically by using 6-point Gaussian quadrature. Finally, $C(n, T)$ of Eq. 4.4 is averaged over the distribution in number of particles/cage in the same way as discussed in chapter 3 using $P(n, T_o, \{t_0 \forall i\})$.

4.3 Results and discussions

Before presenting our results for the 8-site system appropriate to the He atoms inside K-L zeolite let us discuss a simpler system consisting of 4 sites and two

spin-less ${}^3\text{He}$ atoms. This will help us elucidate the nature of the tunnelling states in this system. Let (i,j) denote a state when two particles are located at site i and j , respectively. In the absence of tunnelling ($t=0$), the ground state is 4-fold degenerate corresponding to the bound pairs (we take $V=-24\text{K}$ following chapter 3), $(1,4)$, $(3,4)$, $(2,3)$, and $(1,2)$. The excited state is 2-fold degenerate corresponding to the unbound pairs $(1,3)$ and $(2,4)$ since site 1 and 3 and 2 and 4 are next nearest neighbors. The energy splitting between the ground and the excited state is 24K , quite large. In the presence of tunnelling the ground state degeneracy is lifted partially. The spectrum now consists of three doublets which, for $t=-7\text{K}$, have energies -30.44K , -24K , $+6.4\text{K}$ respectively. The lowest energy gap reduces dramatically from 24K to 6.44K . One can physically think of this splitting as resulting from tunnelling of a bound pair from one configuration to another. This lowest energy gap depends on t in a nonlinear fashion, the three values of the gap corresponding to $t=-7\text{K}$, -14K , and -20K are respectively 6.44K , 18.46K , and 29.76K . Thus for a distribution of t , one expects to see smaller energy gaps and hence an increased heat capacity at low- T . Fig. 4.1 gives the comparison of the density of states with and without disorder for the spinless fermions (fig. 4.1(a)) and for bosons (fig. 4.1(b)) for the 4 site 2 particle system. The energy and the disorder parameter σ are in unit of t_0 . The dashed lines correspond to the system without disorder. One can easily see that the density of states is shifted to the lower energy in the presence of disorder. Fig. 4.2 gives the comparison of the corresponding heat capacity changes. The disorder increases the low temperature heat capacities.

Next we present the numerical results for the 8-site system. Since in chapter 3 we concentrated on the spinless fermion model, we will discuss in detail the effects

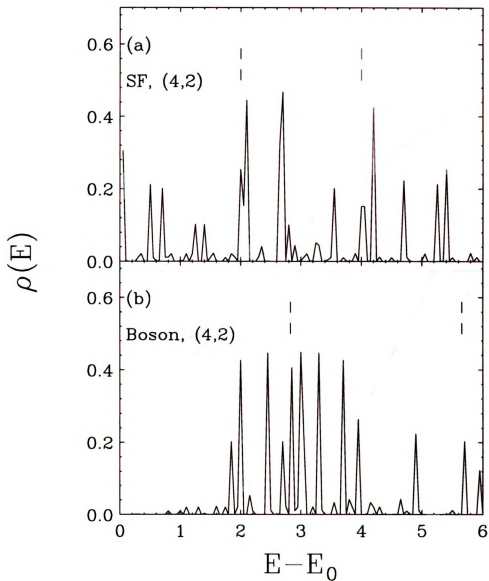


Figure 4.1: Comparison of the density of states with (solid line, $\sigma = 0.5$) and without (dashed line) disorder for the 4 site 2 particle case. Energy and σ in unit t_0 , $V=0$. (a) Spinless fermions. (b) Bosons.

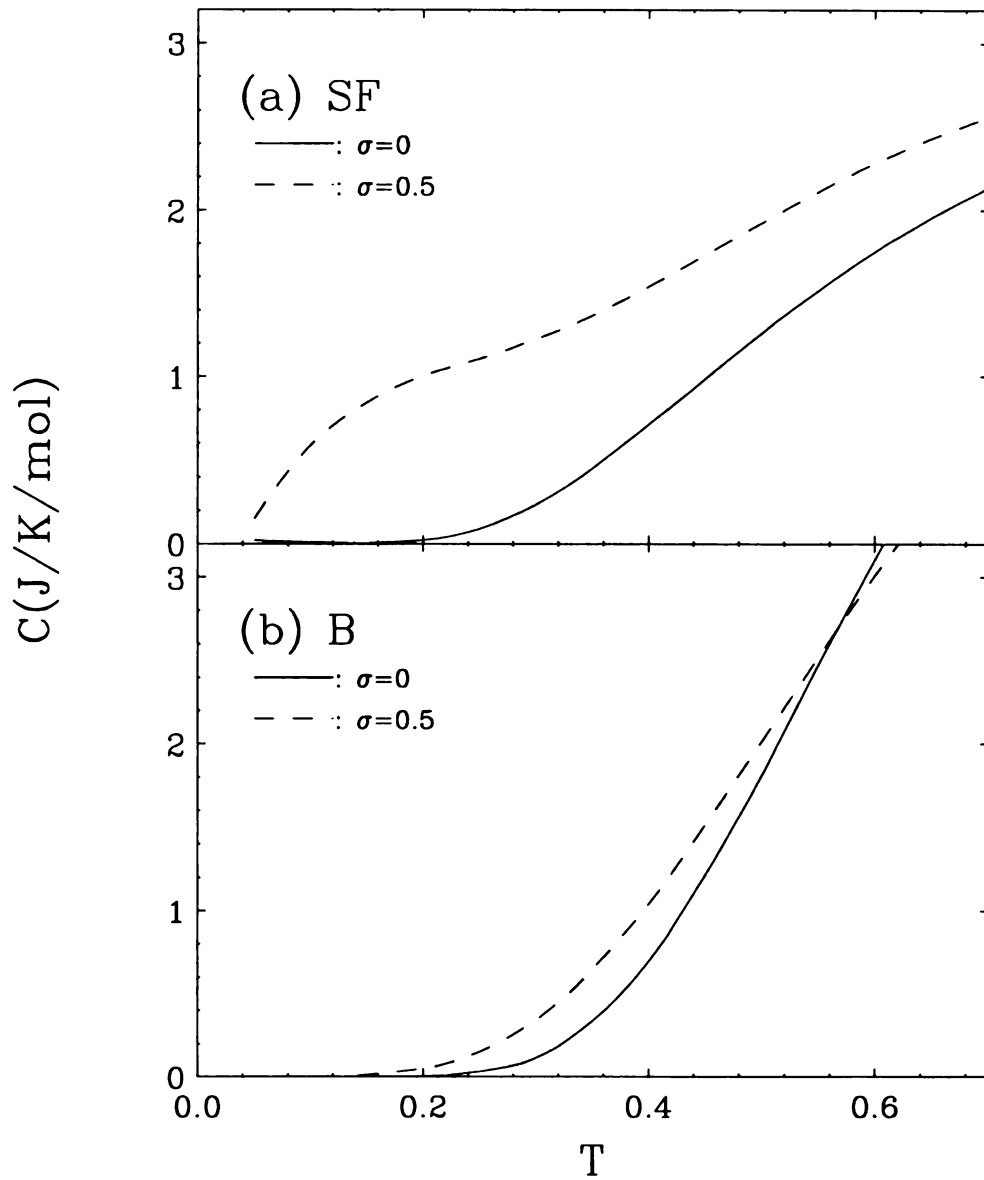


Figure 4.2: Comparison of the heat capacity with (dashed line, $\sigma = 0.5$) and without (solid line) disorder for the 4 site 2 particle system. Temperature (T) and σ are in unit t_0 , $V=0$. (a) Spinless fermions, (b) Bosons.

of disorder for this system. In our calculation, we kept the inter-site attraction parameter V the same as in the non disorder case ($V=-24\text{K}$) and varied the mean value of the tunnelling parameter t_0 and the width of the gaussian distribution σ to get an optimal fit with the experiment for different values of $\langle n \rangle$ and T . The parameter values for which we present our results are: $t_0=-17\text{K}$, $V=-24\text{K}$, and $\sigma=7.0\text{K}$. The ratio of the disorder parameter to the mean band width is about 0.2 which looks quite reasonable. Fig. 4.3 gives the results of the temperature dependence of the heat capacity for ^3He treated as spinless fermions without (fig.4.3(a)) and with (fig.4.3(b)) disorder. As we can see, the effect of disorder is to enhance the low-temperature heat capacity as expected. Fig.4.4 gives the results of helium concentration ($\langle n \rangle$) dependence of the heat capacity again without (fig.4.4(a)) and with (fig.4.4(b)) disorder. It is obvious that the results with disorder agree much better with experiments especially at very low temperatures. But, there is still a large discrepancy between our calculations and experiment for $\langle n \rangle$ larger than 6. We do not understand the reason for this rather large discrepancy.

We have carried out the same calculations for bose system. As we can see from fig. 4.5, there is a dramatic increase in the very low temperature heat capacity in the presence of disorder.

4.4 Summary

In summary, we have investigated the effect of disorder on the low-T heat capacity of small He clusters inside K-L zeolite by extending the model developed in the previous chapter by taking a random distribution of tunnelling parameters,

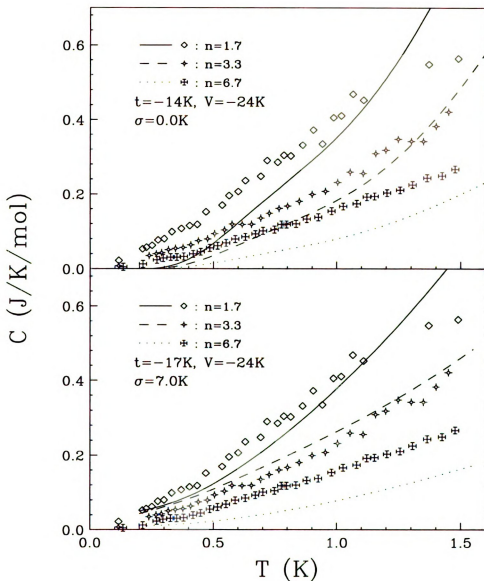


Figure 4.3: Heat capacity vs. temperature for fixed helium atom concentration for ${}^3\text{He}$. Symbols are experimental results and lines are our corresponding calculated results. (a) without disorder, $t=-14\text{K}$, $V=-24\text{K}$. (b) with disorder, $t=-17\text{K}$, $V=-24\text{K}$, $\sigma = 7.0\text{K}$.

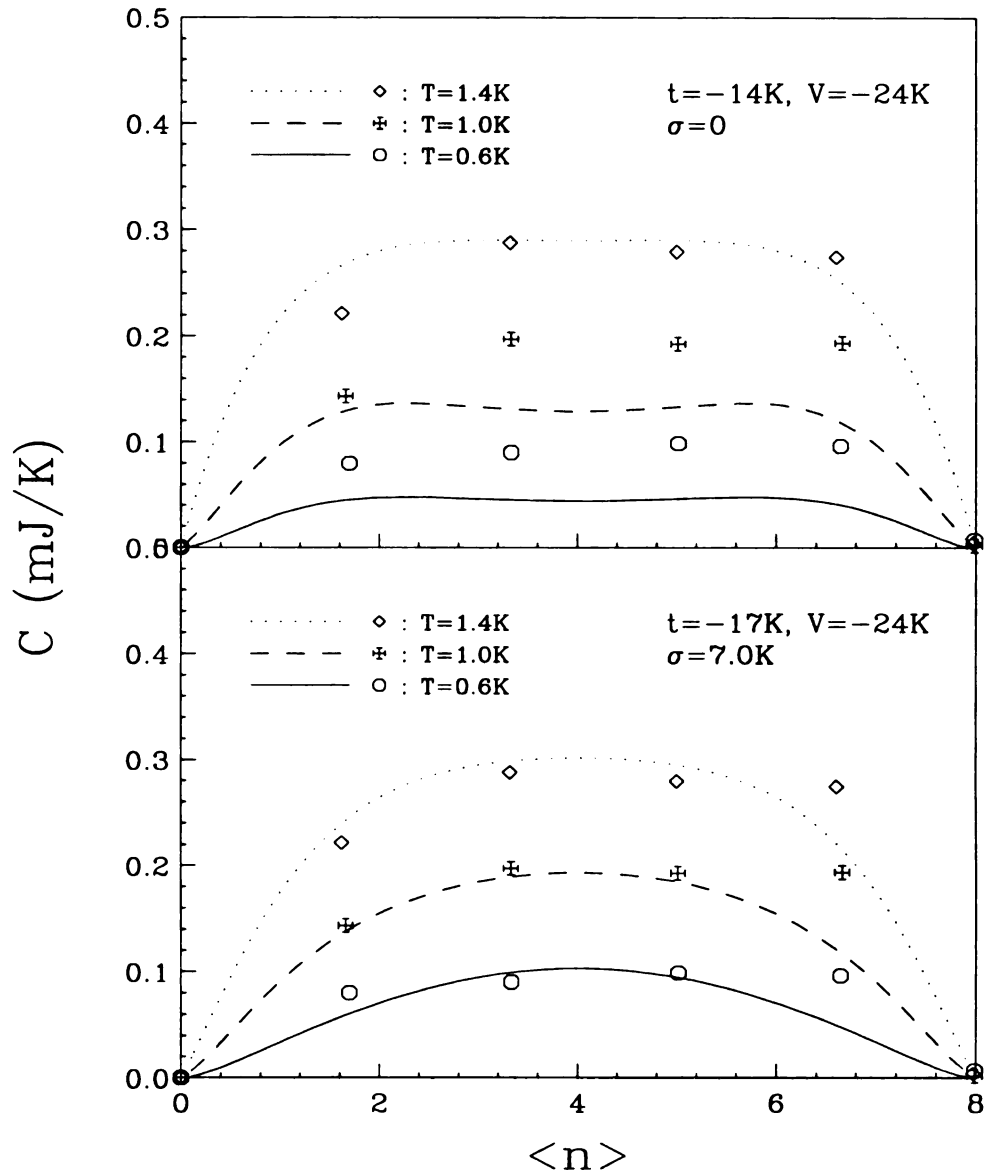


Figure 4.4: Heat capacity vs. helium atom concentration $\langle n \rangle$ for fixed temperatures for ${}^3\text{He}$. Symbols are experimental results and lines are our corresponding calculated results. (a) without disorder, $t = -14\text{K}$, $V = -24\text{K}$. (b) with disorder, $t = -17\text{K}$, $V = -24\text{K}$, $\sigma = 7.0\text{K}$.

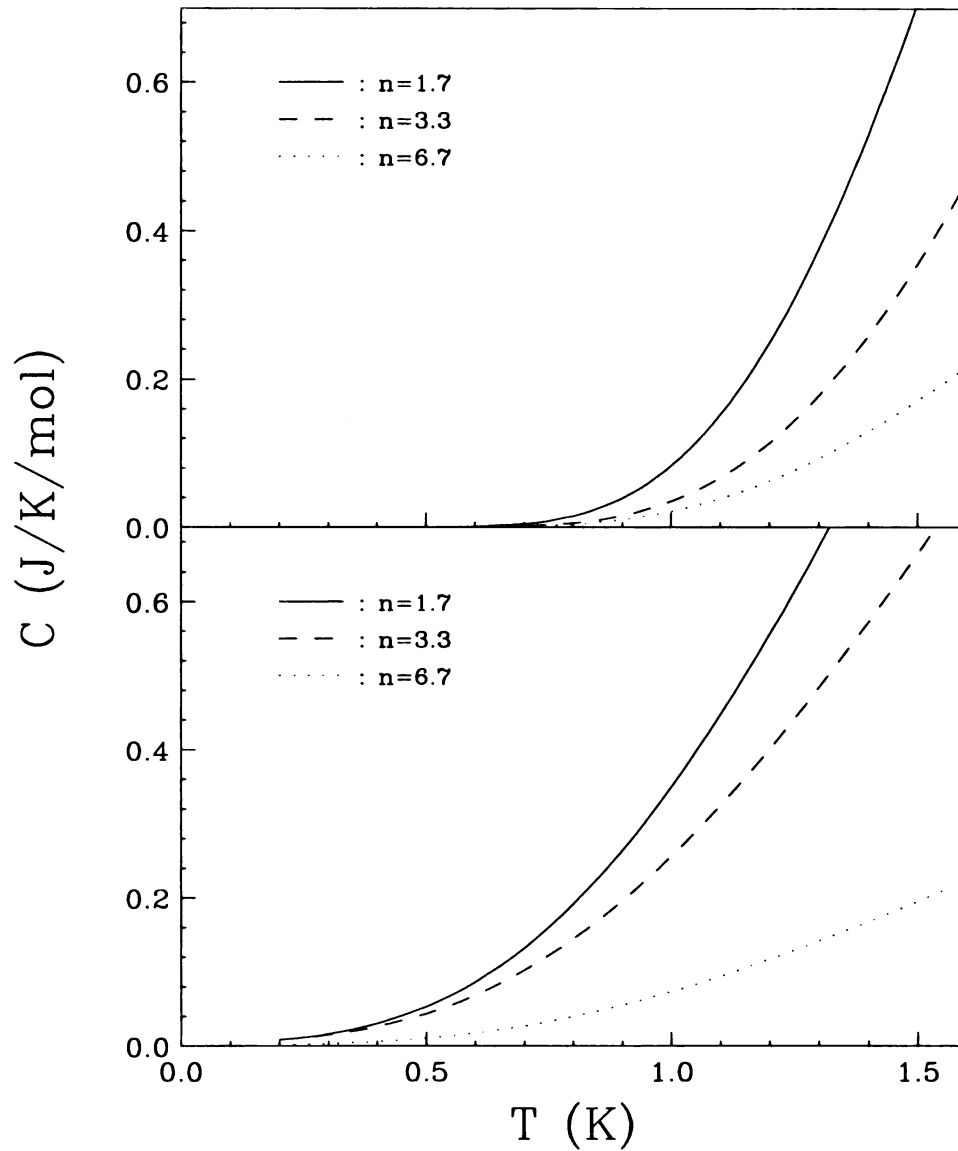


Figure 4.5: Heat capacity vs. temperature for fixed helium atom concentration for ${}^4\text{He}$. (a) without disorder, $t=-14\text{K}$, $V=-24\text{K}$. (b) with disorder, $t=-14\text{K}$, $V=-24\text{K}$, $\sigma = 8.0\text{K}$.

computing the energies and averaging the heat capacity using different probability distributions. This approach to a quantitative evaluation of the effects of disorder on the low-T heat capacity yields results in much better agreement with experiment although detailed quantitative agreement is still lacking. Our model gives a microscopic picture of disorder induced low energy excitation spectrum associated with the correlated tunnelling motion of cluster of He atoms.

Chapter 5

Thermal Excitations of Xenon Clusters Inside a Model L-Zeolite

5.1 Introduction

As we have discussed in earlier chapters, an important feature of the intracrystalline space of zeolites is its inhomogeneous nature. To see how the thermodynamic properties of clusters of atoms or molecules confined inside these microporous media depend on their internal inhomogeneity we have investigated the physical properties of small rare gas clusters confined inside the cages of L-zeolite. In the previous chapters (chapter 2, 3, 4), we discussed the case of interacting helium particles (^4He , ^3He atoms) by modeling the internal inhomogeneity of the confining medium and the inter-particle interaction through Hubbard-like models. In this chapter and the next one, we focus our attention on confined classical systems instead but take into account the effect of the microporous hosts in a more realistic fashion [21].

We have chosen cluster of Xe atoms inside L-zeolite, because these atoms are

excellent NMR probes and their physical properties can be experimentally studied using NMR experiments. It is also possible to directly probe the structure of the confined cluster by either X-ray or neutron diffraction measurements.

Thermodynamic and dynamic properties of rare gas atoms, such as Ar and Xe, trapped inside intracrystalline cavities of zeolites (referred to as hosts) have attracted considerable attention in recent years.[86]-[92] These trapped atoms (referred to as guests), depending on their number density and the relative strengths of the guest-guest and the guest-host interactions, form clusters whose structure and physical properties can differ dramatically from those of their free counterparts. One of the interesting features is the so called gas/liquid phase coexistence [90] resulting from a rapid exchange between the gas phase atoms inside zeolite cages with those adsorbed on the intracrystalline surface. Depending on the thermodynamic state of the adsorbed atoms one may think of this as gas/solid coexistence instead. To develop a microscopic understanding of the above mentioned coexistence, Li and Berry carried out preliminary studies of the dynamics of six Ar atoms trapped inside model cavities.[90] Their model cavity consisted of a spherical shell with the guest-host interaction modeled by Morse potential, with comparable strengths of the guest-guest and guest-host potentials. They observed that the confinement strongly altered the geometry *i.e.* instead of 2 minima and 4 saddles seen in Ar_6 in free space they found 5 minima and 8 saddles. The overall melting characteristics were however quite similar for both the free and the confined Ar_6 clusters. Our interest here is to introduce a more realistic host and study the above mentioned properties.

In addition to isolated confined clusters, there is also a great deal of current

interest in cluster assembled materials(CAM), where a solid is formed out of clusters. A simple example of CAM is C_{80} solid. Physical properties of CAM's are expected to be dramatically different from their atomic counterparts. A simple way to fabricate CAM's is by trapping the clusters inside the intra-crystalline space of inhomogeneous hosts such as zeolites, layered silicates etc..

5.2 Method and the physical system

We have concentrated on the thermodynamic and dynamic properties of two types of confined Xe clusters, (1) a single 6 atom Xe cluster inside an L-zeolite cage (denoted as Xe_{6c}) and (2) a periodic array of Xe_{6c} which we identify as a cluster assembled material and denote as Xe_{6CAM} . For the thermodynamic properties, we have used Monte Carlo (MC) method, the details of which can be found in the earlier work of Eppers and Kaelberer who were the first ones to study the 'melting' of free Lennard-Jones clusters [93]-[95]. For the dynamics studies we have used classical constant temperature molecular dynamics simulation [96].

The structure of the L-zeolite has been shown in fig. 1.1 and fig. 1.2. Most of the zeolites normally contain a mixture of Si and Al atoms in the silicate framework and for overall charge neutrality there are a number of charge compensating cations which occupy different positions inside the system. For simplicity, in the present study we assume the framework contains no Al ions and therefore we do not have to worry either about the disorder in the positions of framework anions or the charge compensating alkali (K and Na) cations as in the L and K-L zeolites. We expect the basic physics underlying both melting and dynamics at high temperatures not to be greatly affected by this approximation.

Before performing the simulation with many Xe atoms, the potential energy surface for a single Xe atom was analyzed to get an idea of how the single particle potential V , varied inside the cage of the main channel and whether it was possible for a single Xe atom to go from one main channel to another through the subsidiary 4- and 8-channels. Following Vernov *et.al.* [88] the interaction between the Xe and Si atoms has been replaced by an effective Xe-O interaction potential and by readjusting the Oxygen Lennard-Jones parameters. Hence the cage consists of only a frame work of Oxygen atoms. The Lennard Jones parameters used in this calculation are: $\sigma_{Xe-O}=3.3\text{\AA}$, $\epsilon_{Xe-O}=151\text{K}$, $\sigma_{Xe-Xe}=4.1\text{\AA}$, and $\epsilon_{Xe-Xe}=221\text{K}$. We also compared the potential calculated using the effective Xe-O parameters with that obtained using more realistic Xe-Si and Xe-O parameters [97] and the two results agreed very well. It is found that the energy barrier along the transverse direction (perpendicular to the channel axis which we denote as the z axis) is extremely high, of the order 150,000 K for a rigid framework. For the temperature range in which we are interested in this paper (room temperature or less), the probability of Xe atoms escaping from one main channel to other neighboring channels in this transverse direction is therefore extremely small. Therefore, periodic boundary conditions are applied only along the z direction of the cell. The position of the cage is taken symmetrically to be about $z=0$. Hence each time the potential produced by the framework atoms on a Xe atom is required, the coordinate of the latter is folded back to the central cage. This ensures the calculation of the potential due to all the Oxygen atoms within a given cutoff radius.

We have chosen a cut off radius of $4.5\sigma_{Xe-O}$, where σ_{Xe-O} is the length parameter associated with the Xe-O Lennard Jones potential. A cage consisting of

five unit cells along the z direction, and parts of the neighboring unit cells along in the x - y plane are used to satisfy the cutoff requirement from any point inside the central unit cell. The total number of Oxygen atoms inside the cut-off radius turns out to be 1464.

Before analyzing the interplay of Xe-cage and Xe-Xe interactions we first investigated the thermal properties of a single Xe atom and then starting from the ground state configuration of the Xe_{6c} cluster, we slowly heated up this system. ‘Melting’ of the Xe_{6c} cluster is monitored by recording the average energy ($\langle E \rangle$) and average bond length fluctuation (δ) which typically show a characteristic rapid change even for small clusters.[90, 93, 94, 95]. For the Xe_{6c} system, we have taken two sets of MC runs. A set of 11 runs, each consisting of 10^5 MC step/particle (MCS/p) at each temperature; the other set consists of 3 runs where the number of MC steps is increased by a factor of 10. We will discuss the comparison of these results later. For the Xe_{6CAM} system, we do the same steps as for the Xe_{6c} system. We have taken 3 runs and each run takes 10^5 MCS/p for the heating process and at least 2×10^6 MCS/p for the cooling process. The step length is 0.165 (in unit of σ_{O-Xe}) for heating and 0.033 for cooling. We will discuss the step length problem later.

The molecular dynamics simulation method we have used to probe the dynamics is the well-known Nosé dynamics [96] which generates a canonical ensemble (or constant temperature ensemble). In this method, an additional degree of freedom s is introduced, which acts as an external system. The interaction between the physical system and s is expressed via scaling of the velocities of the particles,

$$\mathbf{v}_i = s\dot{\mathbf{r}}_i. \tag{5.1}$$

The Lagrangian of the extended system of particles and s is given by

$$L = \sum_i \frac{m_i}{2} s^2 \dot{\mathbf{r}}_i^2 - \phi(\mathbf{r}) + \frac{Q}{2} \dot{s}^2 - (f+1)kT_{eq} \ln(s). \quad (5.2)$$

where the third term and the fourth term are the kinetic energy and the potential energy associated with the dynamic variable s , respectively. The quantity f is the number of degree of freedom of the physical system and Q has the dimensions of energy. T_{eq} is the required equilibrium temperature.

The equation of motion for the particles are

$$\ddot{\mathbf{r}} = -\frac{1}{m_i s^2} \frac{\partial \phi}{\partial \mathbf{r}_i} - \frac{2\dot{s}}{s} \dot{\mathbf{r}}_i. \quad (5.3)$$

The equation of motion for s is

$$Q\ddot{s} = \sum_i m_i s \mathbf{r}_i^2 - \frac{(f+1)kT_{eq}}{s}. \quad (5.4)$$

To make sure that the system is at equilibrium, we first run MC simulation upto 10^5 time steps/particle at the temperature we want. Then, we read the configuration and use this to initiate the MD run. The time interval is 10^{-5} ns and the total time period that we followed is typically about 1.6 ns.

5.3 Results

5.3.1 MC simulation

A single Xe atom inside L-zeolite channel

Figures 5.1 and 5.2 show the potential energy landscape for the $z=0$ plane for different values of the azimuthal angle Φ and r , the distance from the center as

one approaches the cage wall (please see fig. 1.1 and fig. 1.2 for the L-zeolite structure). The potential has nearly 12-fold azimuthal symmetry as we approach the cage wall, the symmetry is slightly broken because the 12 oxygen atoms, although at the same distance from the center, are not uniformly distributed in multiples of 30 degrees along Φ . In addition, there are 6 pairs of oxygen atoms further away which are oriented parallel to the z-axis, and are separated by 60 degrees intervals along Φ . These oxygens atoms also break the 12-fold degeneracy. The primary minima, with energy -2391K, are located at $r=4.45\text{\AA}$. The difference in the energy values of the primary and secondary minima is about 80K. As r is reduced or the particle moves away from the cage wall, the potential shows nearly 6-fold symmetry. We see from the figure that the Φ -barrier goes from about 350K for $r=4.4\text{\AA}$ to a few K for $r=3\text{\AA}$. As regards the barriers along the channel axis, we show in fig. 5.3 how the potential changes as we change z starting from one of the Φ -minima, for different values of r . For $r = 0$, i.e along the channel axis, the potential is minimum near the aperture (neck) and maximum near the cage center, the energy barrier to move along the channel axis being about 250K. Therefore the most likely path taken by a Xe atom in going from a primary minima near the wall to that near the neck is to first move towards the cage center and before actually making it to the center move towards the neck.

In fig. 5.4 we give the results of MC simulation for a single Xe atom in the temperature range $5\text{K} < T < 150\text{K}$. Starting from the ground state where the particle occupies one of the primary minima, as we heat the system, the average energy $\langle E \rangle$ initially increases linearly with a slope 1.5, consistent with that for a 3-dimensional harmonic oscillator. In the temperature interval 10-70K, the slope rises and then changes back to 1.5 after about 70K. The physical origin

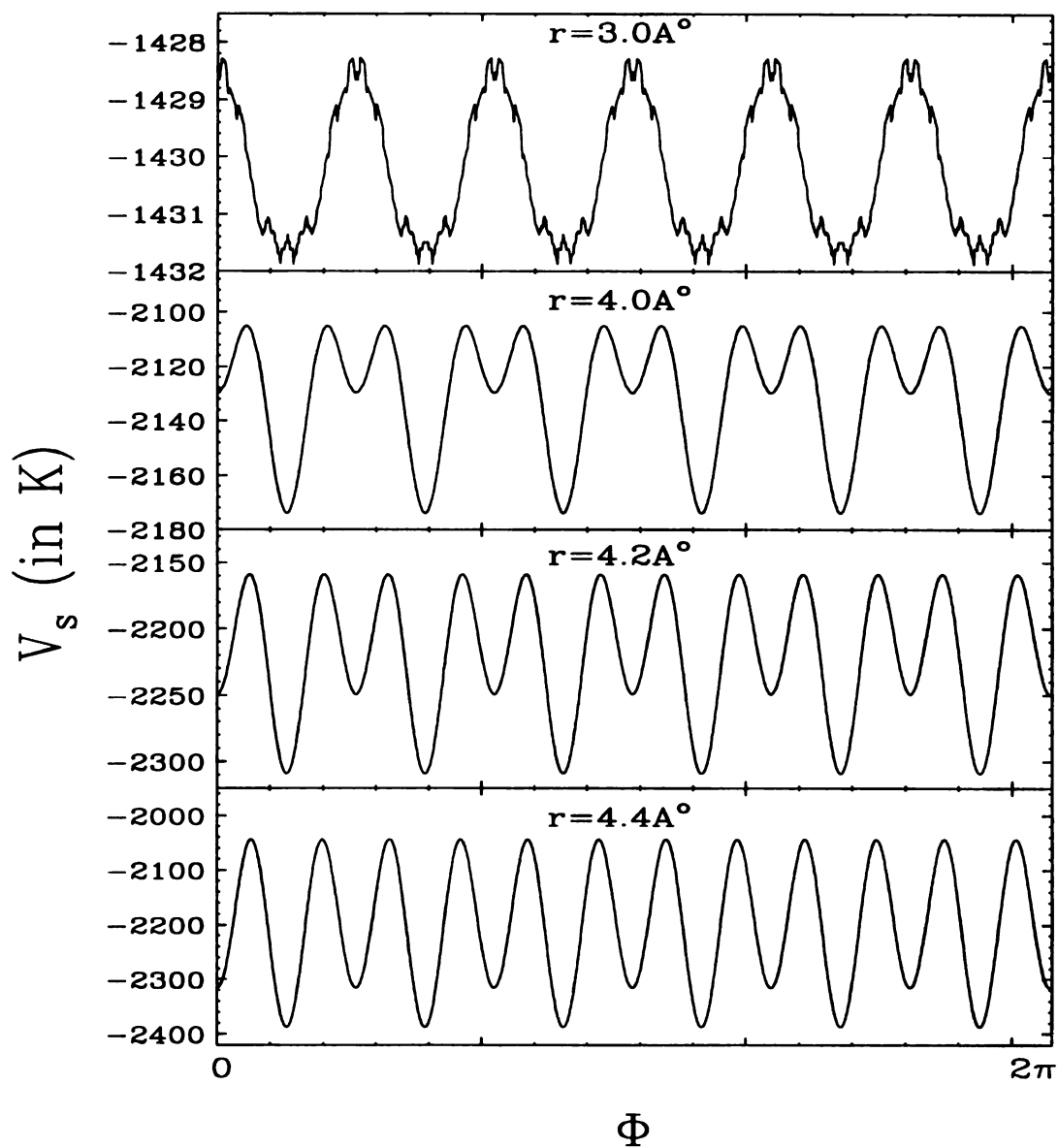


Figure 5.1: Single-particle potential energy V_s for Xe as a function of Φ in a plane passing through the center of the L-zeolite cage in units of K, r is the radial distance from the cage axis.

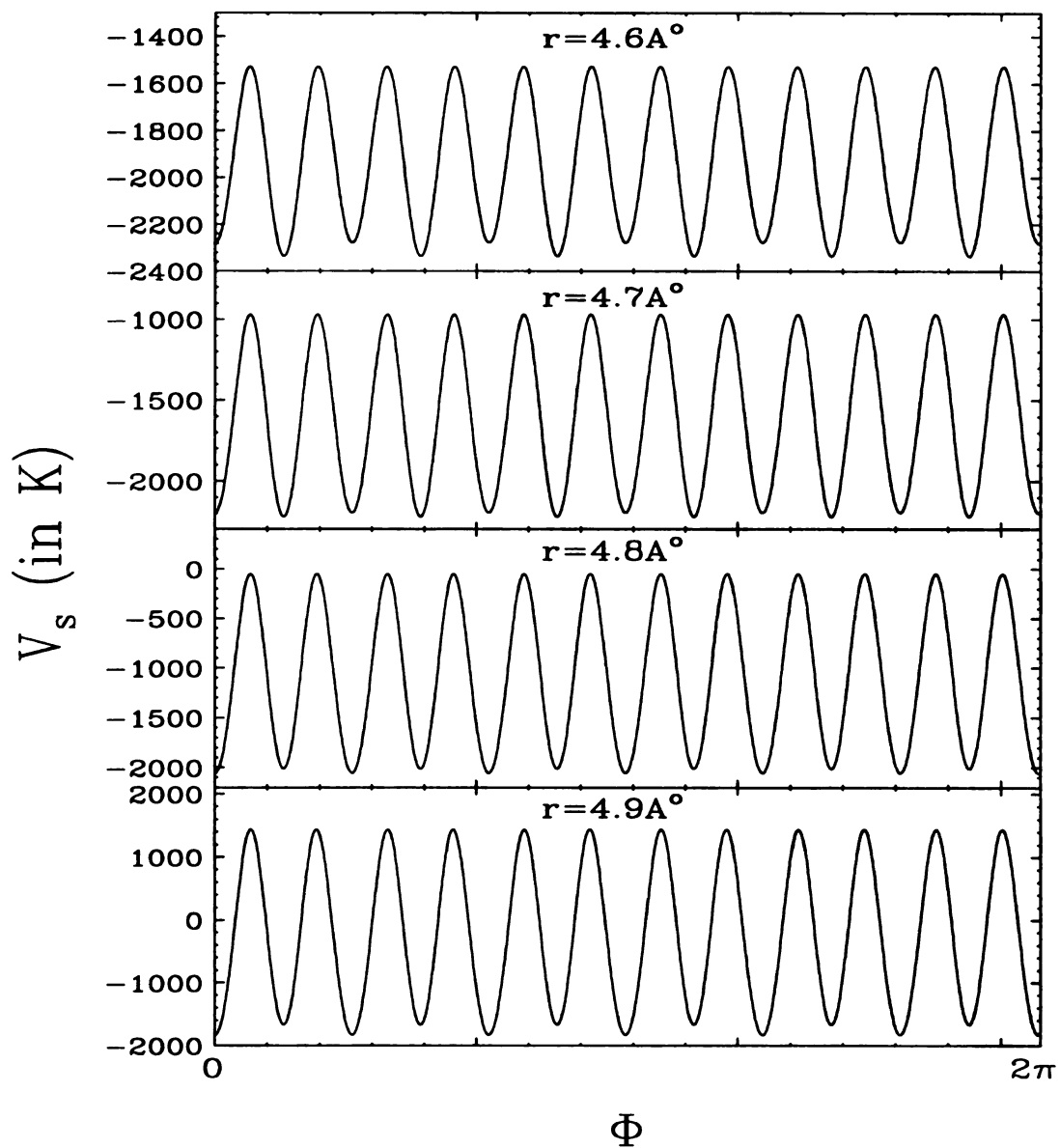


Figure 5.2: Single-particle potential energy V_s for Xe as a function of Φ in a plane passing through the center of the L-zeolite cage in units of K, r is the radial distance from the cage axis.

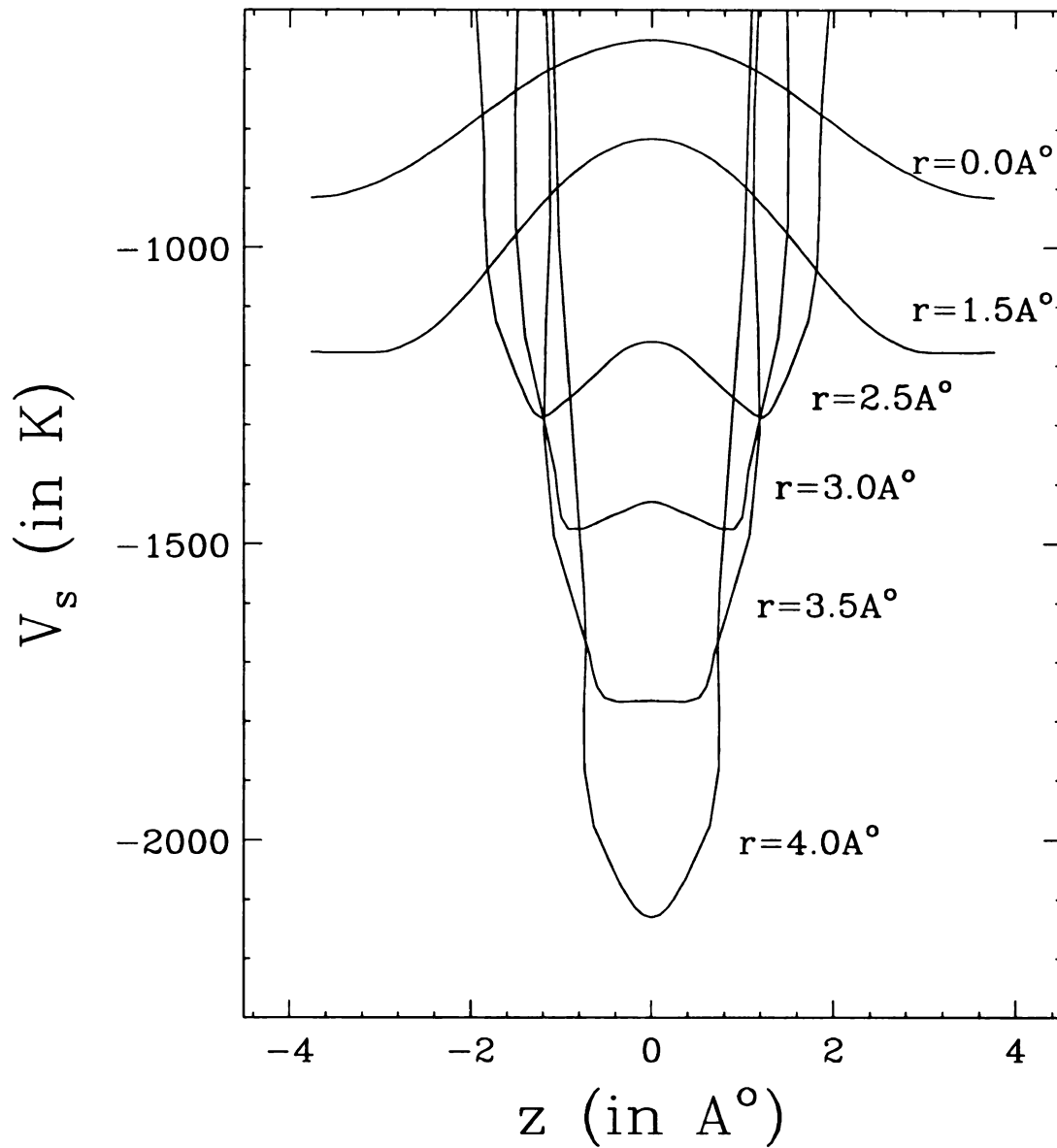


Figure 5.3: Single-particle potential energy V_s as a function of z inside the L-zeolite cage in units of K, r is the radial distance from the cage axis. The azimuthal angle ϕ is chosen to be zero.

of this temperature dependence of the slope can be attributed to the existence of six secondary minima separated from the primary minima by an energy Δ of about 80K. The particle still behaves like a harmonic oscillator as regards r and z degrees of freedom. On the other hand the partition function for the Φ degree of freedom can be approximated as $Z_\phi = 6(1 + \exp(-\Delta/kT))Z_{osc}$ which gives a cross over region in T dependence of $\langle E \rangle$ at kT near 0.5Δ . This is in accordance with our MC simulation results.

Xe_{6c} cluster

At first, the ground state structure of Xe_{nc} clusters was determined by Monte Carlo quenching (some times referred to as MC docking). Because of the strong one particle potential, the Xe atoms occupy essentially the primary minima as long as $n \leq 6$ per cage. In fact the distance between two Xe atoms occupying the two nearest primary minima is about 4.45Å whereas the distance between two isolated Xe atoms at their LJ minimum is 4.60Å at which distance the Xe-Xe pair energy is -221K. Since the Xe-Xe pair energy at a separation 4.45Å is about -210K, the Xe atoms prefer to form a nearly commensurate structure with the zeolite single particle potential. The ground state of the Xe_{6c} cluster is therefore a ring where the Xe atoms are located very close to the six primary minima as shown in the fig. 5.5. In contrast, the free Xe₆ cluster has the usual bi-pyramid structure (see fig. 5.6). Thus the guest-host interaction strongly affects the structure of confined Xe_{6c}.

The melting of the Xe_{6c} system is studied by slowly heating the system in temperature intervals of 8K. As mentioned in the method section we carried out

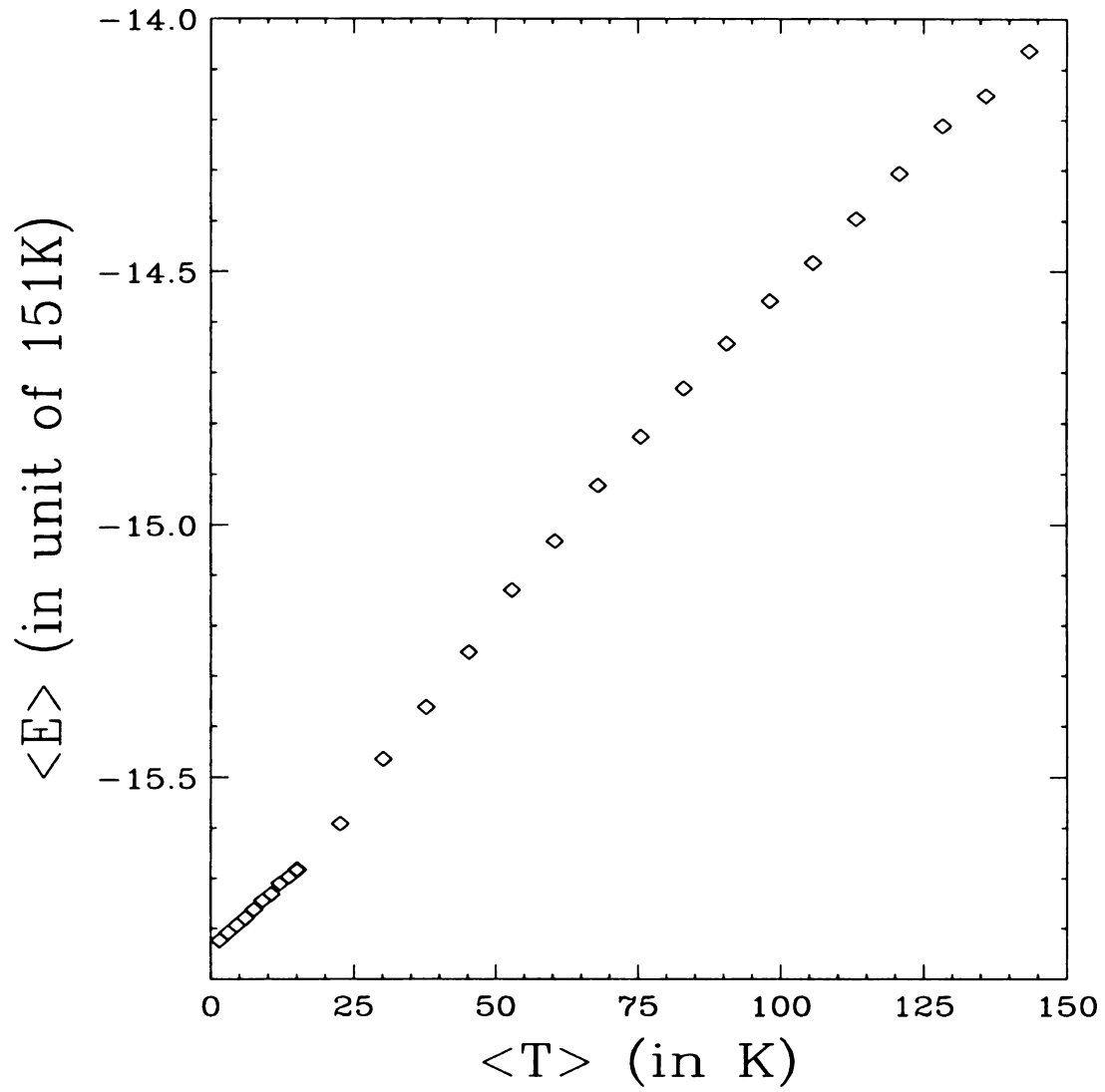


Figure 5.4: Average energy $\langle E \rangle$ vs T for a single Xe atom inside L-zeolite.

Active

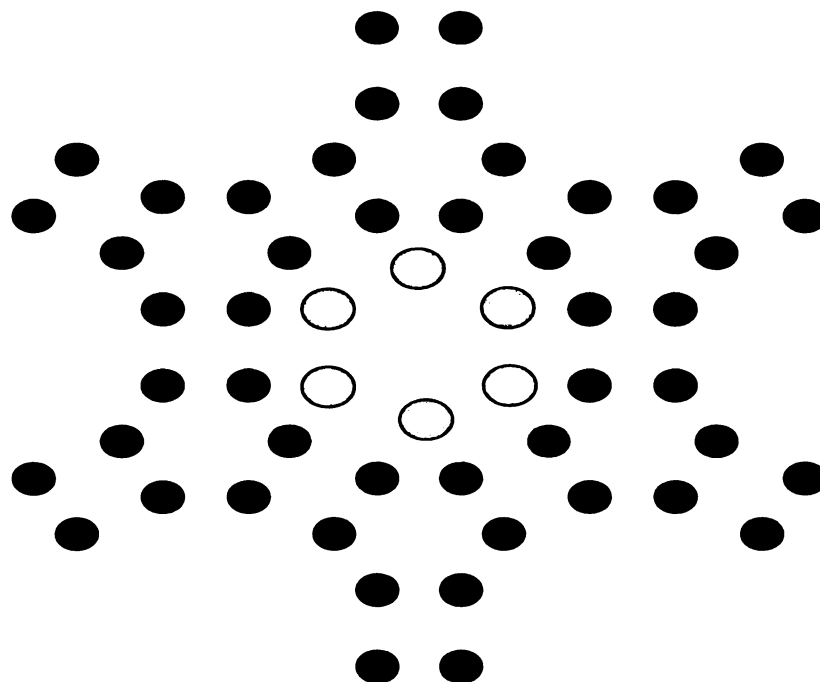


Figure 5.5: Positions of the six Xe atoms (large circles) in the ground state of Xe_{6c} and the framework Oxygen atoms (small circles) in the $z=0$ plane.

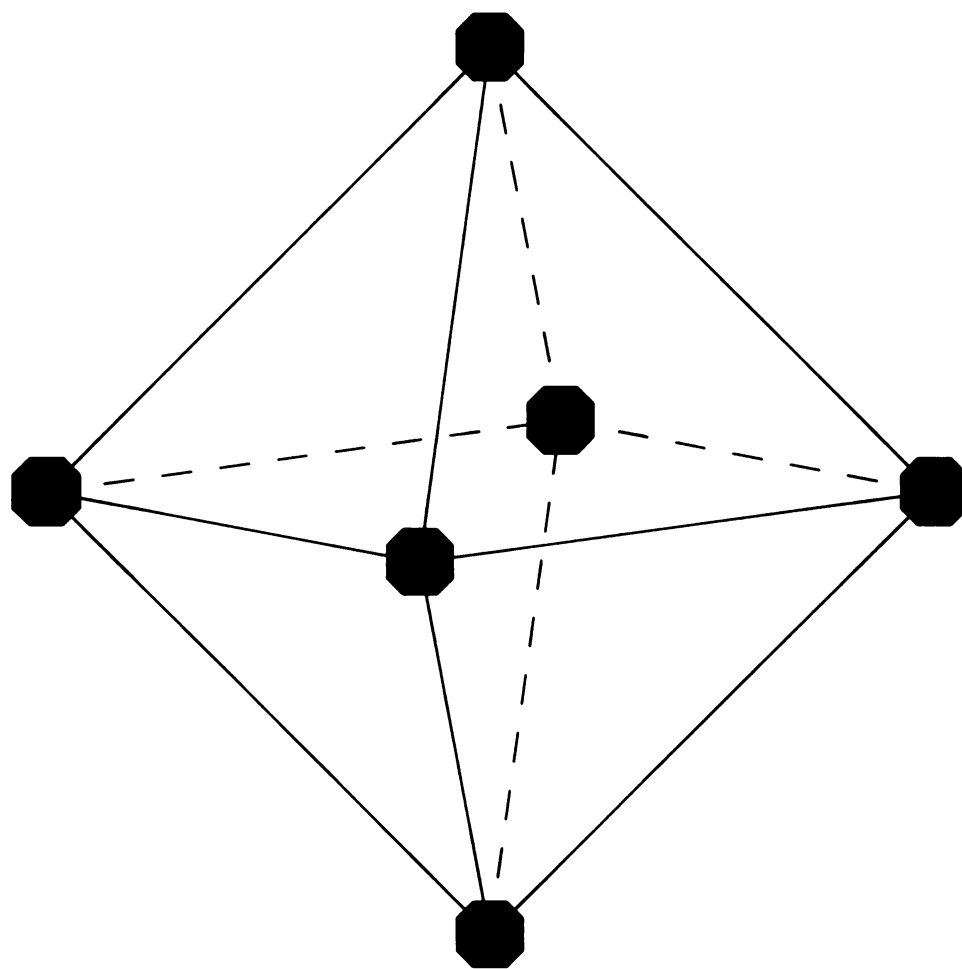


Figure 5.6: The ground state of a free Xe_6 cluster

two sets of MC runs, one with 10^5 MCS/p and the other with 10^6 MCS/p. Fig. 5.7(a) shows the average energy $\langle E \rangle$ as a function of temperature for the first set of runs. Fig.5.7(b) gives the corresponding value of the average bond length fluctuation. In this set of runs, for each T, the number of MC steps were 100,000, following 20,000 discarded sweeps for thermalization. The line in each figure is the average taken over all the 11 runs. Fig. 5.8 shows the same functions as fig. 5.7 except in this case the number of MC steps is 10 times more than in the previous set. At low T the excitations of the 6-atom ring are those of a harmonic oscillator and hence one expects to see a slope of 1.5 in the $\langle E \rangle$ vs T curve. The observed slope in fig. 5.7 and in fig. 5.8 is 1.4. We find that ‘melting’ of the cluster occurs when one of the six ring Xe atoms is dislodged and moves towards the center of the cage and then towards the neck region. The movement of the remaining five Xe atoms between the ring sites becomes much more likely and this process can be looked at as a vacancy moving from one ring site to another. We will refer to this excited state structure as the (5-1) cluster. The average bond-length fluctuation δ increases rapidly in the neighborhood of 120K which may be close to the ‘melting’ temperature of the confined Xe_{6c} cluster. We also note that the value of δ above the melting temperature is larger for the longer MC runs. This results from the intercage diffusive motion of the excited Xe atom.

The energy needed to excite one Xe atom from one of the primary minima (ring sites with energy about -2400K) to the minimum energy position of the ‘odd’ atom of the (5-1) cluster is about 1150K (see fig. 5.3, $r=1-1.5\text{\AA}$). The T=0 energy of the (5-1) cluster differs from the true ground state (6-atom ring) by about 1000K. Thus the rapid increase in δ vs T near 120K must be due to reasons other than simple energy considerations. One contributing reason for this rapid change is the

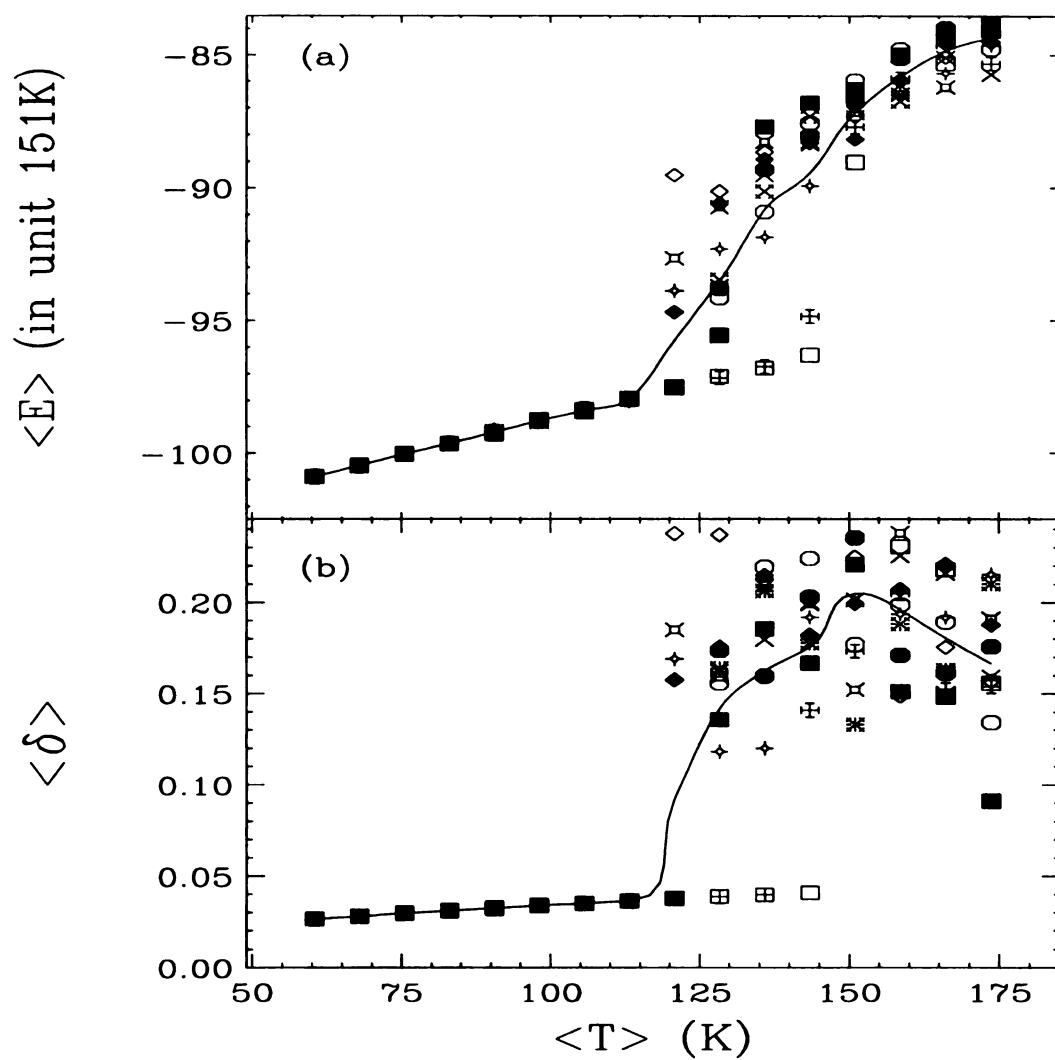


Figure 5.7: Melting of a Xe_{6c} cluster inside the L-zeolite; (a) the average energy $\langle E \rangle$ vs T ; (b) average bond length fluctuation δ vs T . The solid line is the average of 11 sets of run, each consisting of 10^5 runs for each temperature.

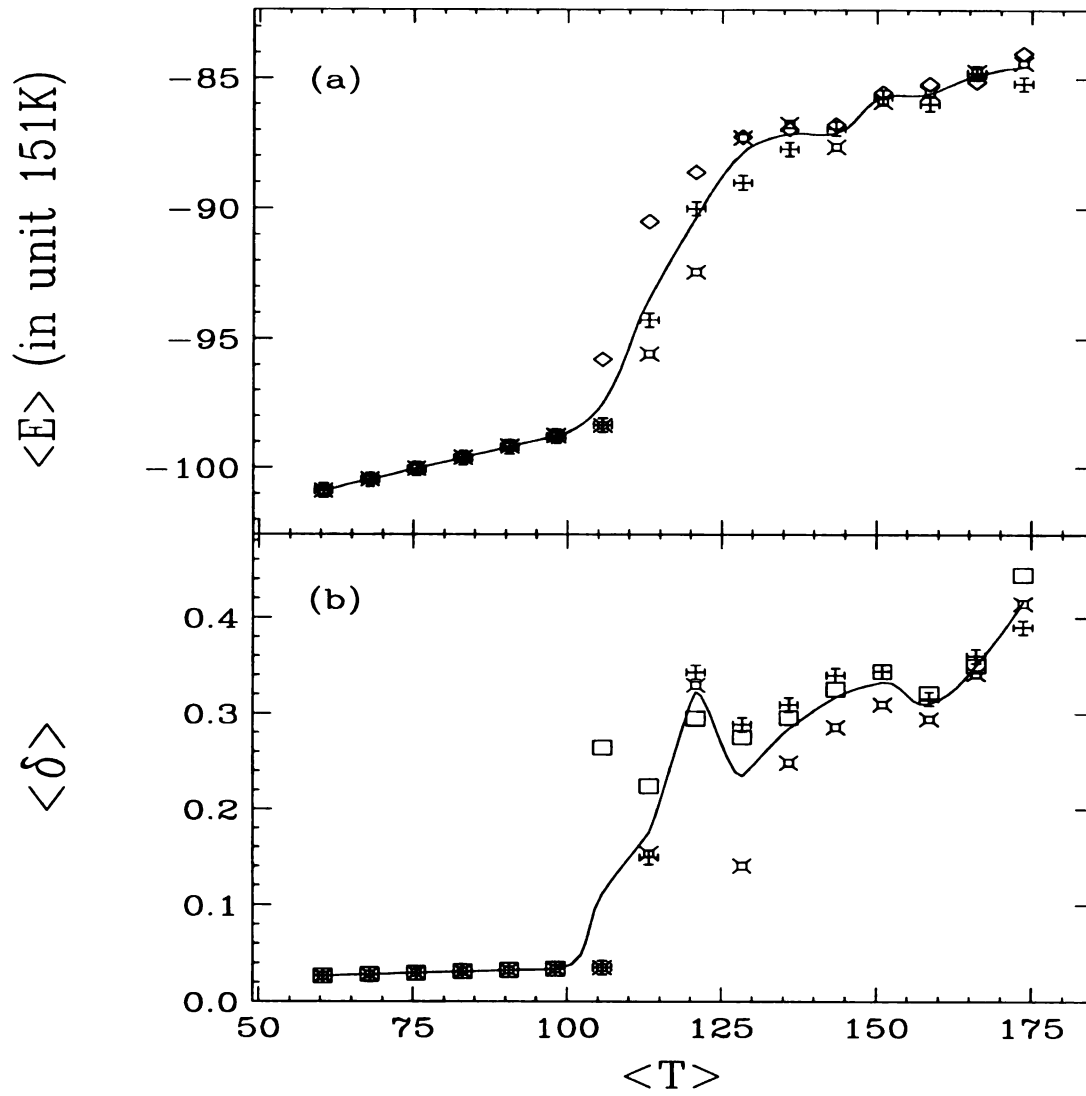


Figure 5.8: The same as in the previous figure excepting here each run consists of 10^6 MC steps and the number of MC run was 3.

higher degeneracy of the (5-1) cluster. Another contributing factor could be the rather large phase space available to the 'odd' atom in the (5-1) cluster compared to the very tightly confined atoms near the primary minima. To see how zeolite confinement alters the thermal properties of a Xe_8 cluster, we show in figs. 5.9 and 5.10 the variation of $\langle E \rangle$ and δ as a function of T for a free Xe_8 cluster. Compared to Xe_{8c} in L-zeolite, the fluctuation in $\langle E \rangle$ is smaller for a free Xe_8 cluster and also the melting temperature of the free Xe_8 cluster is much lower, about 11K.

Melting of Xe_{8CAM} solid—a cluster assembled material

Xe_{8CAM} corresponds to an one-dimensional solid made out of Xe_8 rings and with one ring/cage. The 'melting' curve is obtained by gradually heating the system from 15.1K and at a interval of 8K. We run up to 10^5 MC steps for each temperature point and the step length is 0.165\AA . We have averaged over three sets of MC runs. The cooling curve is much harder to get. It takes at least 2×10^6 MC time steps and the step length has to be reduced to 0.033\AA . This is because there exist some metastable states in this complex potential which make it very difficult for the system to relax to its equilibrium configuration. Fig. 5.11 shows the average energy/cage vs. T curves for both heating and cooling processes. Comparing to the Xe_{8c} system, the 'melting' of Xe_{8CAM} system is much more well defined, but the melting temperature is quite close to but slightly larger than that for a single Xe_{8c} cluster. This reduction in the fluctuation in going from Xe_{8c} to Xe_{8CAM} is clearly due to the inter-cluster interactions. This inter-cluster interaction effects also clearly show up in the difference of $\langle E \rangle$ for Xe_{8c} (shown as a solid line) and Xe_{8CAM} in the same figure.

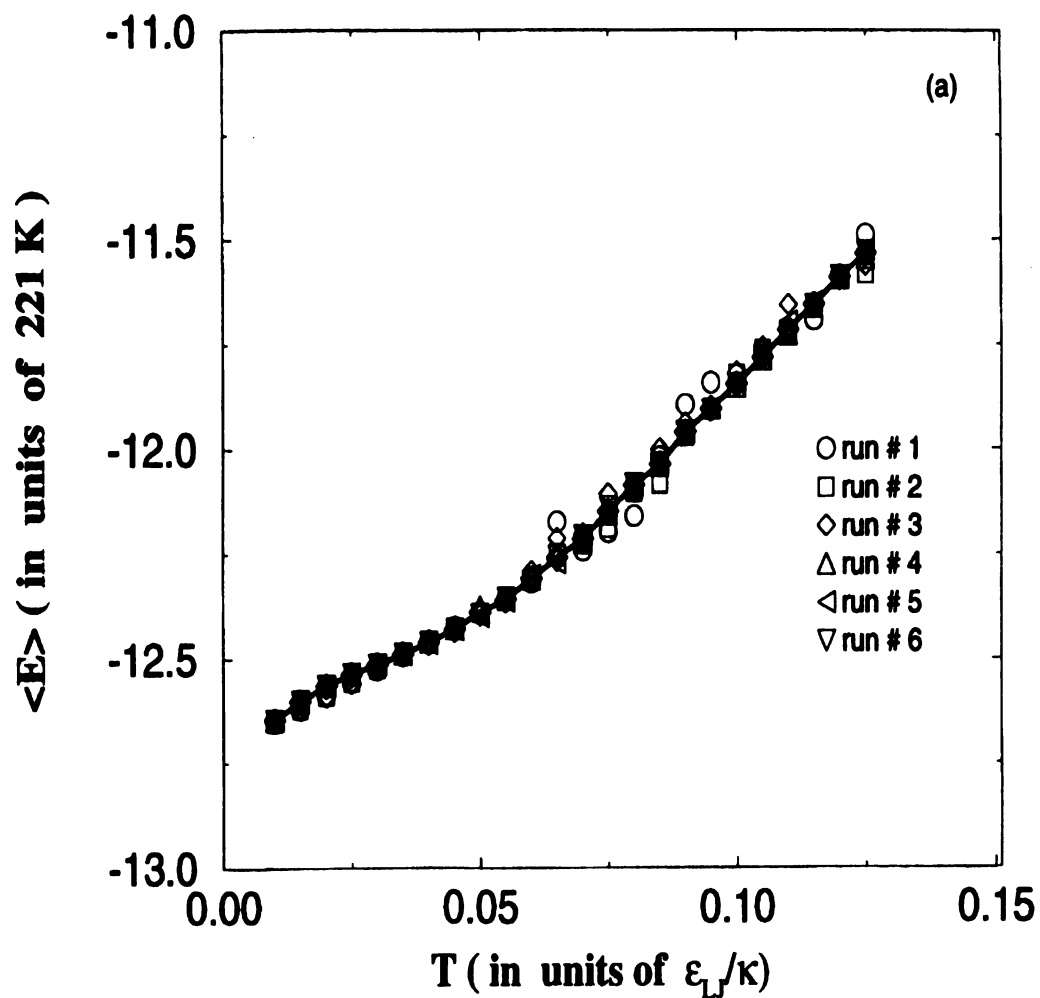


Figure 5.9: Melting of a free Xe_6 cluster: the average energy $\langle E \rangle$ vs T ; The solid line is the average of 6 sets of runs, each consisting of 1.6×10^6 runs for each temperature. $\langle E \rangle$ and T are expressed in terms of Lennard-Jones parameter $\epsilon_{Xe} = 221$ K.

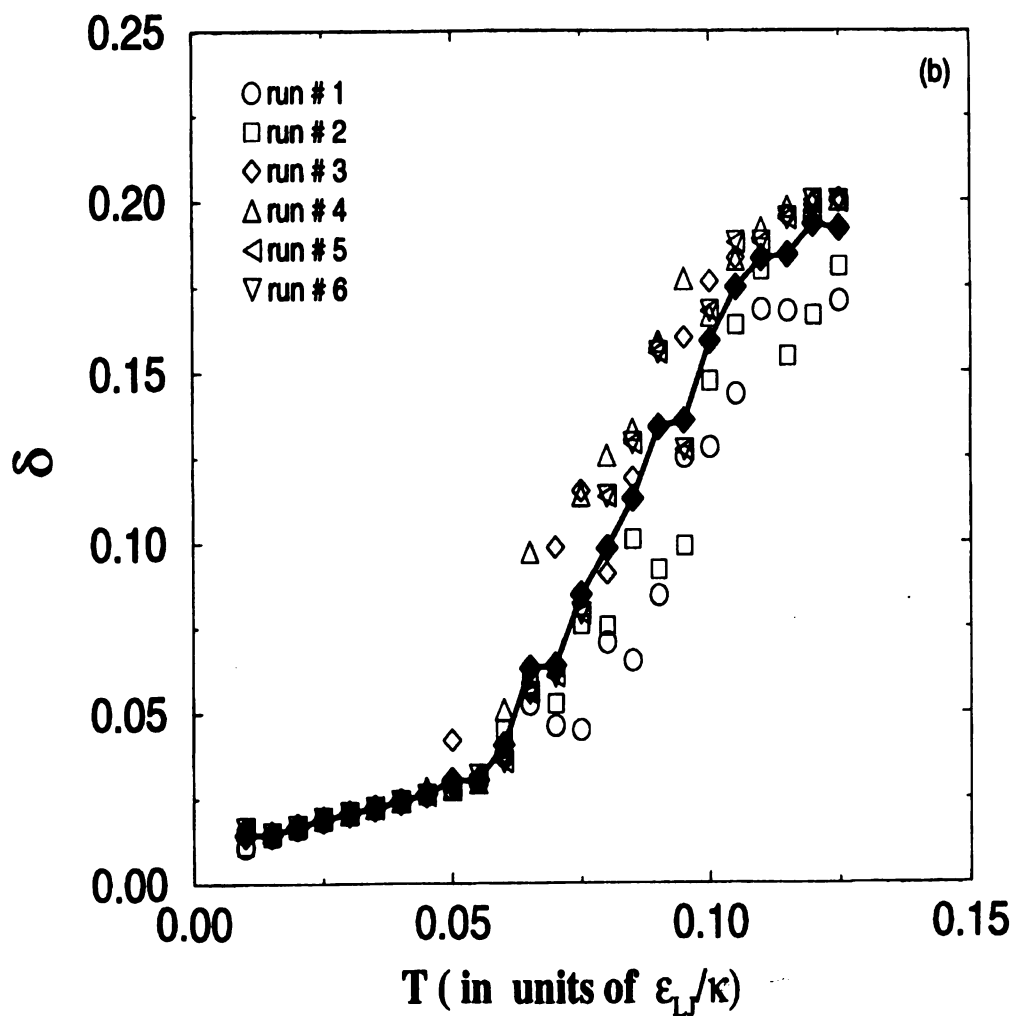


Figure 5.10: Melting of a free Xe_6 cluster: average bond length fluctuation δ vs T . The solid line is the average of 6 sets of runs, each consisting of 1.6×10^6 runs for each temperature. T is expressed in terms of Lennard-Jones parameter $\epsilon_{Xe}/k_B = 221$ K.

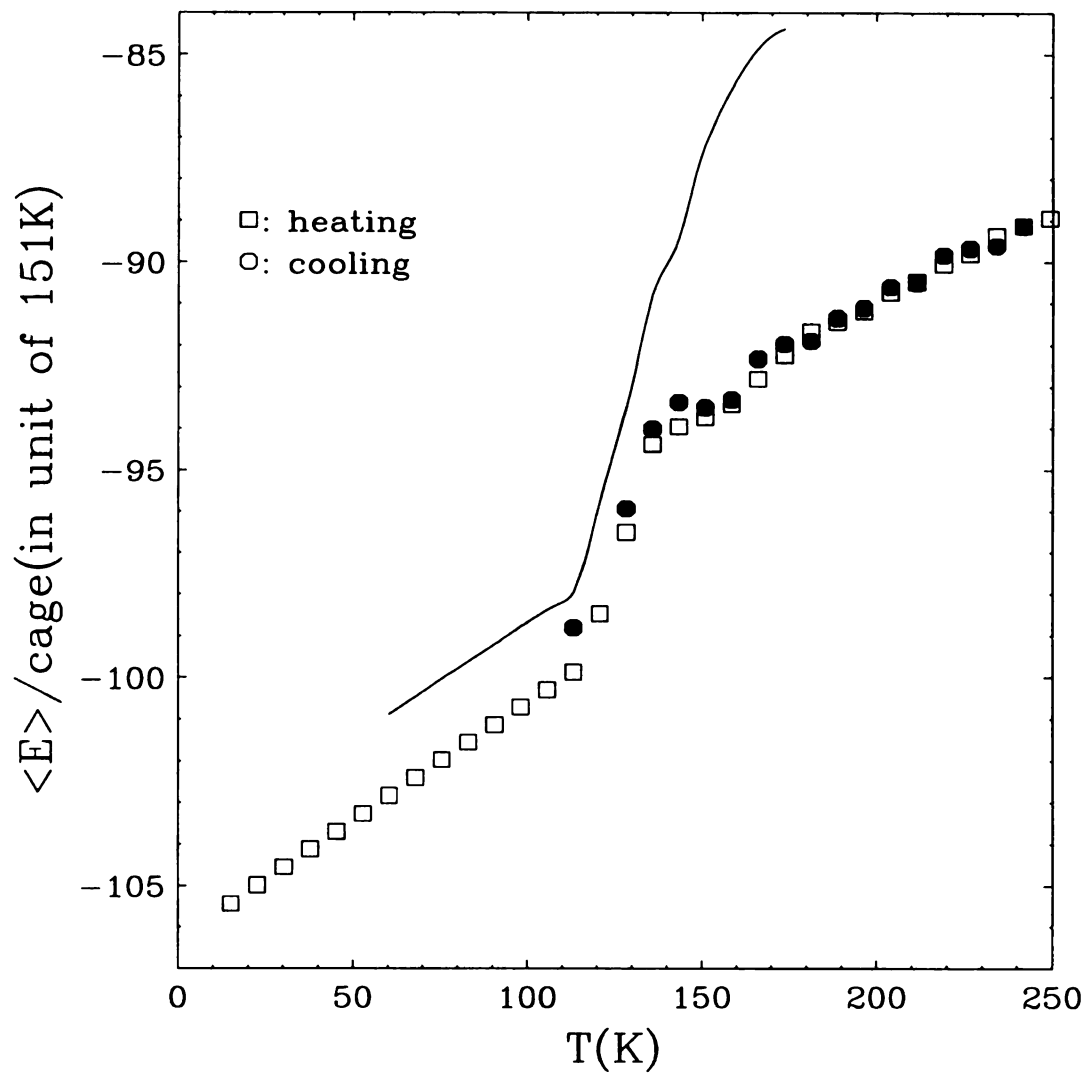


Figure 5.11: Average energy $\langle E \rangle$ vs T for Xe_{8CAM} , a cluster assembled material consisting of a periodic array of Xe_8 clusters inside L-zeolite. Solid line is the averaged energy of Xe_{8c} for comparison.

5.3.2 MD simulation

To study the dynamics of Xe atoms in L-zeolite, we performed molecular dynamics simulation at about room temperature using Nosé dynamics [96]. As we have stated before, we run MC first to make sure that the system is in equilibrium and then observe the diffusion of Xe atoms using MD simulation. Fig. 5.12 is the averaged r^2 vs. time for the Xe_{6c} system. Results for three runs are shown in the figure, each with a different initial configuration. As can be seen from the figure, the path depend sensitively on the initial condition. This is due to the complexity of the system potential. The plateau in one of the curve means that there are no inter-cage motions while the sharp increase in the other means some particle (or particles) is undergoing inter-cage motion. Fig. 5.13 is the r^2 vs. time for each individual Xe for the run 3 which gives evidence for the above statements (note: the cage length is about 7.5Å).

We next study the temperature dependence of the inter- and intra-cage dynamics. In fig. 5.14 we give the averaged r^2 vs. time for Xe_{6c} system at three different temperatures starting from the same initial configuration. The diffusion are quite different in the three runs and for the three temperatures that we have chosen. From our limited number of runs we find that the diffusion rate does not necessarily increase with temperature. Our limited simulation studies indicate that one needs much longer runs and averaging over many more initial configurations to probe the dynamics in this highly inhomogeneous medium accurately.

For the Xe_{6CAM} system, we also take three runs for r^2 vs. time at temperature 302K. As we can see in fig. 5.15, the diffusions is much slower than that of Xe_{6c} system shown in fig. 5.12 (note the scale differences between the two figures).

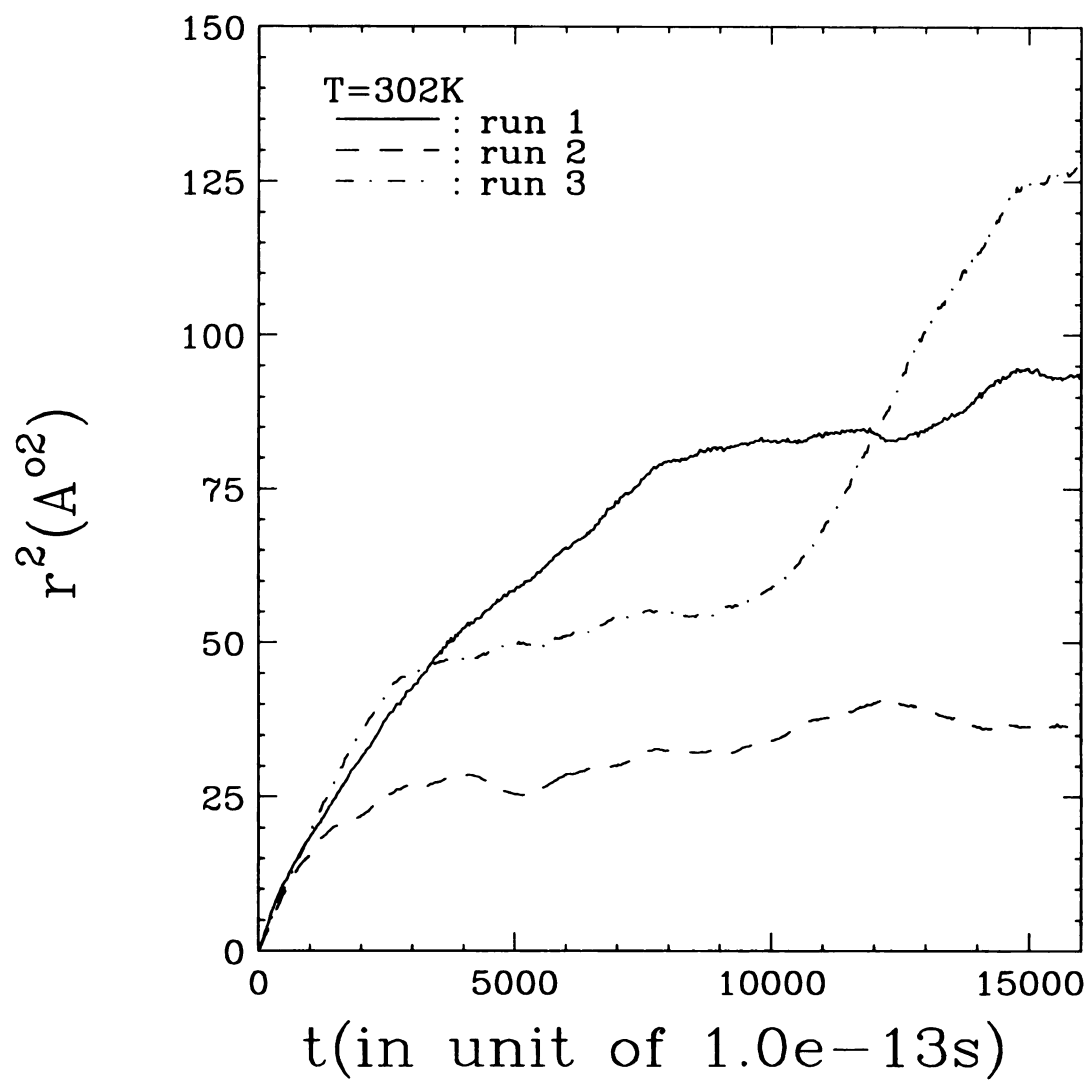


Figure 5.12: r^2 vs. time for the Xe_{6c} system

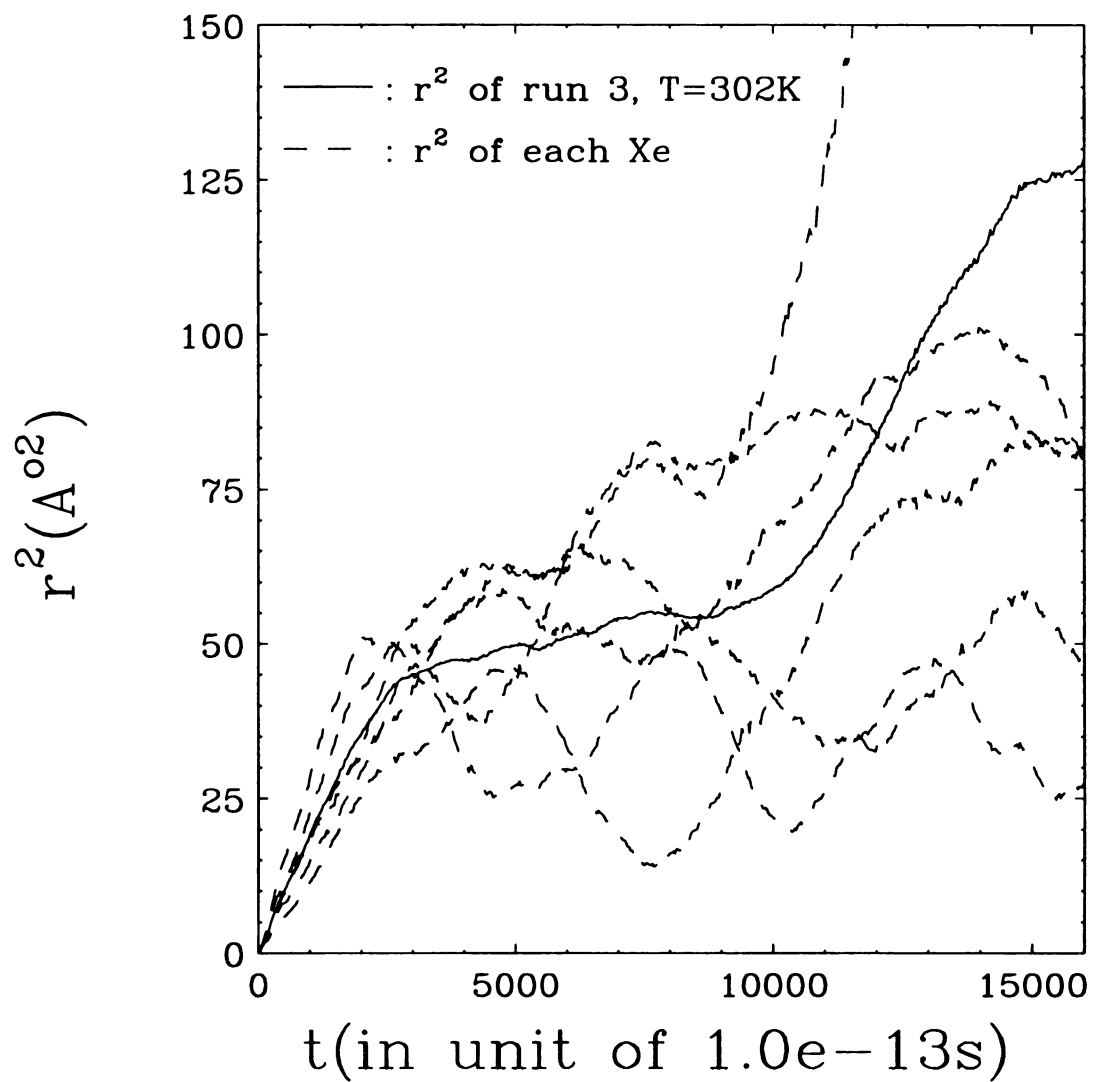


Figure 5.13: r^2 vs. time for each Xe atom along with the result of the averaged one for the $Xe_{e_{6c}}$ system

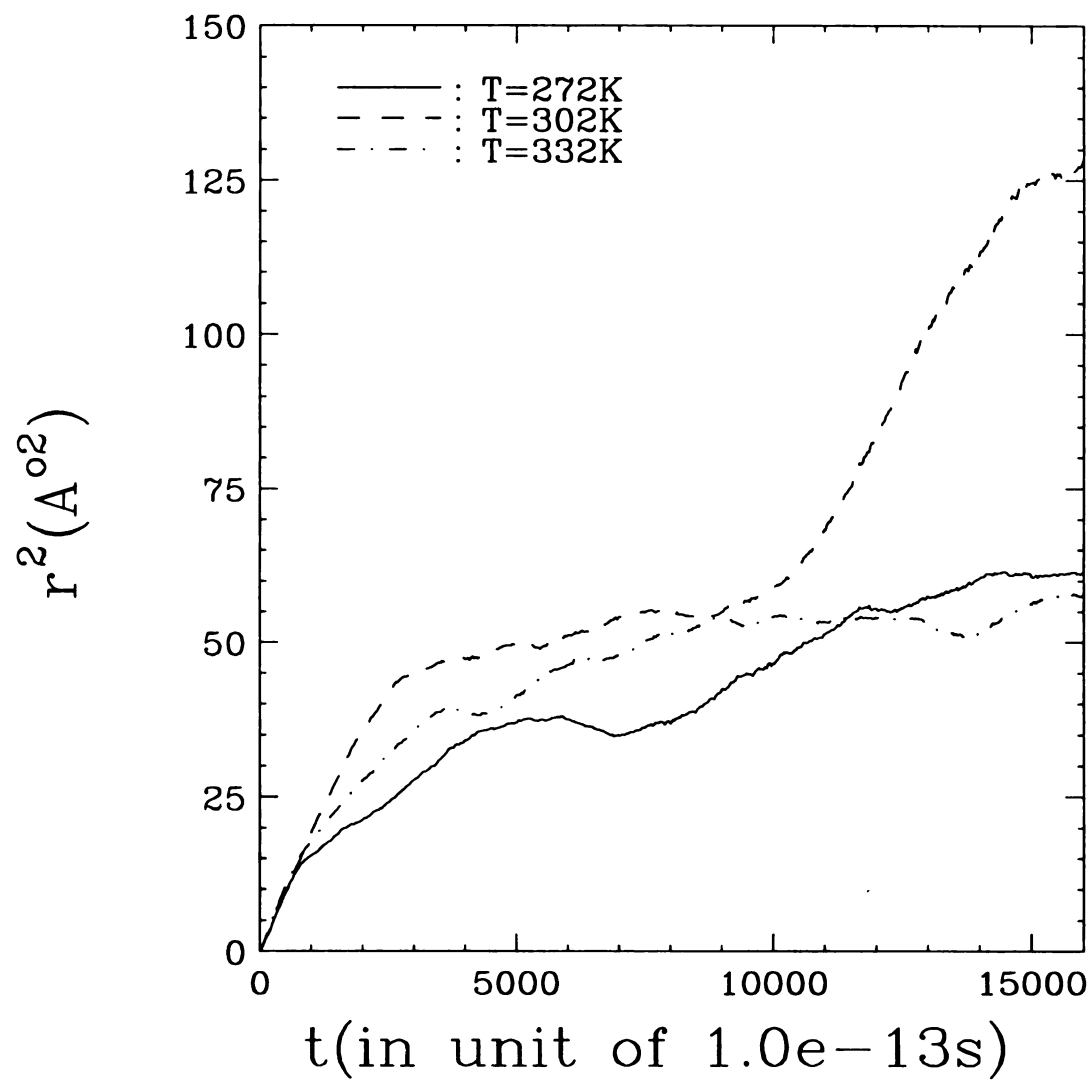


Figure 5.14: r^2 vs. time for the Xe_{8c} system at three different temperatures

Also, there are no inter-cage motion occurring during the time period that we followed which means that it is much harder for Xe atoms to diffuse through the channel in the Xe_{6CAM} system. This is due to the strong particle-particle interactions between the thermally excited atoms in nearest neighbor cages. Fig. 5.16 gives r^2 , x^2 , y^2 and z^2 vs. time in run 1. It shows that there is almost no intercage motion along the channel axis (i.e. in the z direction). Fig. 5.17 is the effective diffusion rate $D(t)$ vs. time for the three runs. Clearly the dynamics is not diffusive since $D(t)$ decreases (perhaps approaches zero) with time.

5.4 Discussion

Monte Carlo studies of confined (in L-zeolite) and free Xe_6 clusters clearly brings out the dominant role played by the guest-host interaction. The inhomogeneous nature of the single particle potential produced by the zeolite cage profoundly alters both the single particle and many particle potential energy surfaces and consequently their thermal properties. Unlike the free cluster where the melting process is rather smooth, i.e. 100,000 MC steps/atom give reasonably converged results for the T dependence of $\langle E \rangle$ and δ , the fluctuation effects are large in the case of the confined cluster. A careful inspection for the two sets of runs indicates that melting process shifts to a lower temperature in fig. 5.8 which consists of runs 10 times longer than for those shown in fig. 5.7. The reason could be traced back to the large potential energy barriers present in the zeolite systems. The energy barriers for particles close to the wall is estimated to be ~ 1200 K. This corresponds to an exponential factor $exp(-\beta * \Delta E) \sim 10^{-6}$ for temperature ~ 100 K. Since the transition is triggered by the dislodging of one of

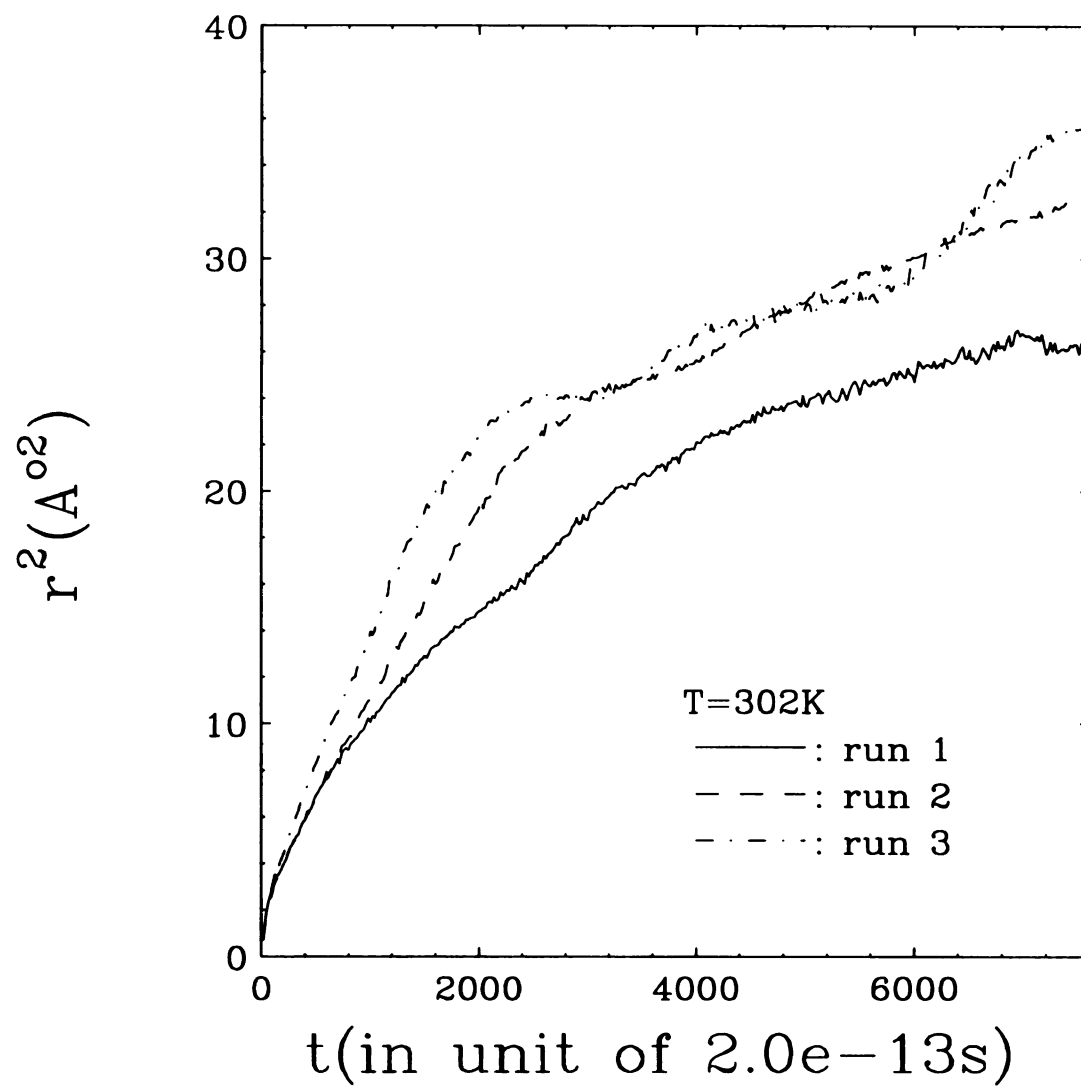


Figure 5.15: r^2 vs. time for the X_{e6CAM} system

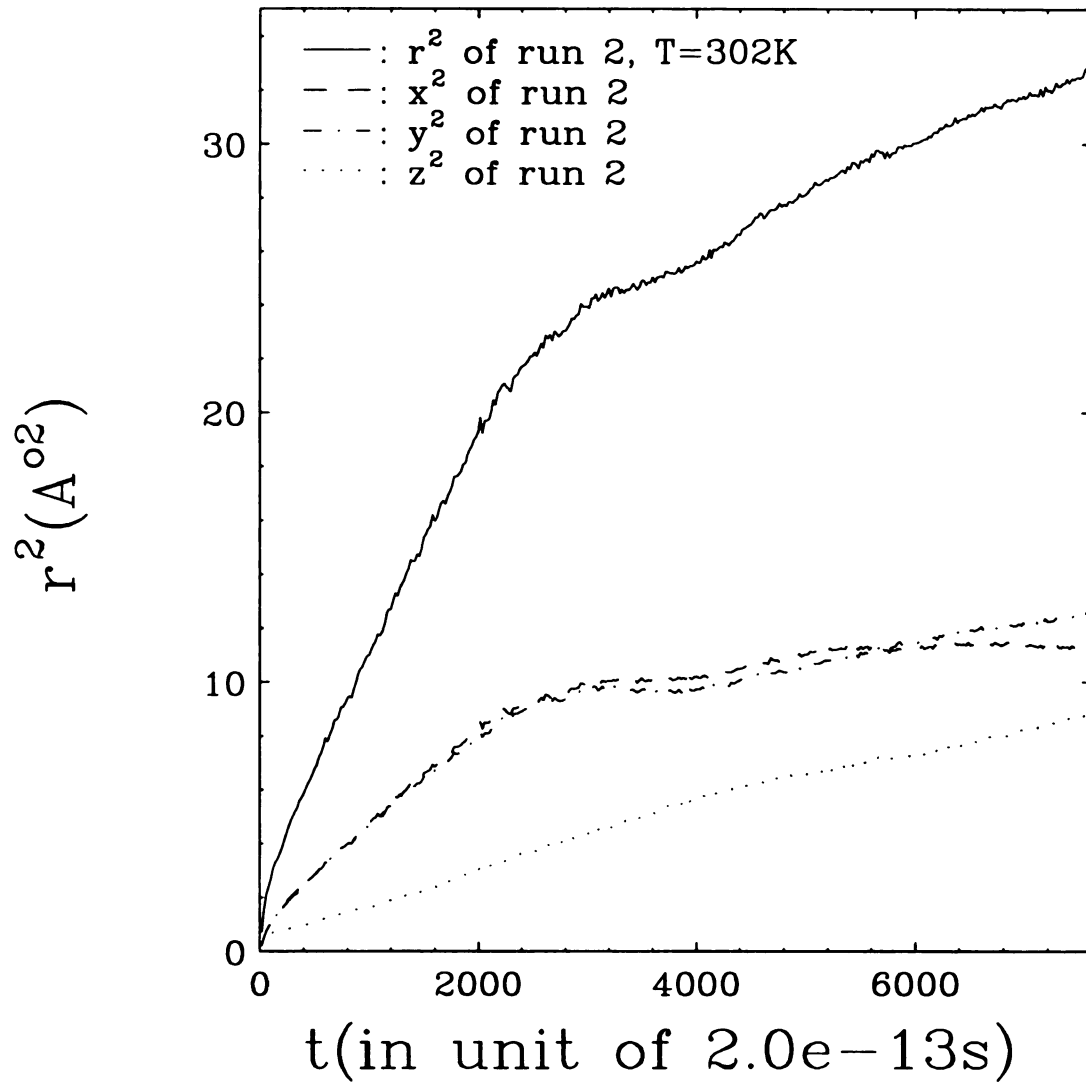


Figure 5.16: r^2 vs. time of run2 with x^2 , y^2 , z^2 also for the Xe_{6CAM} system

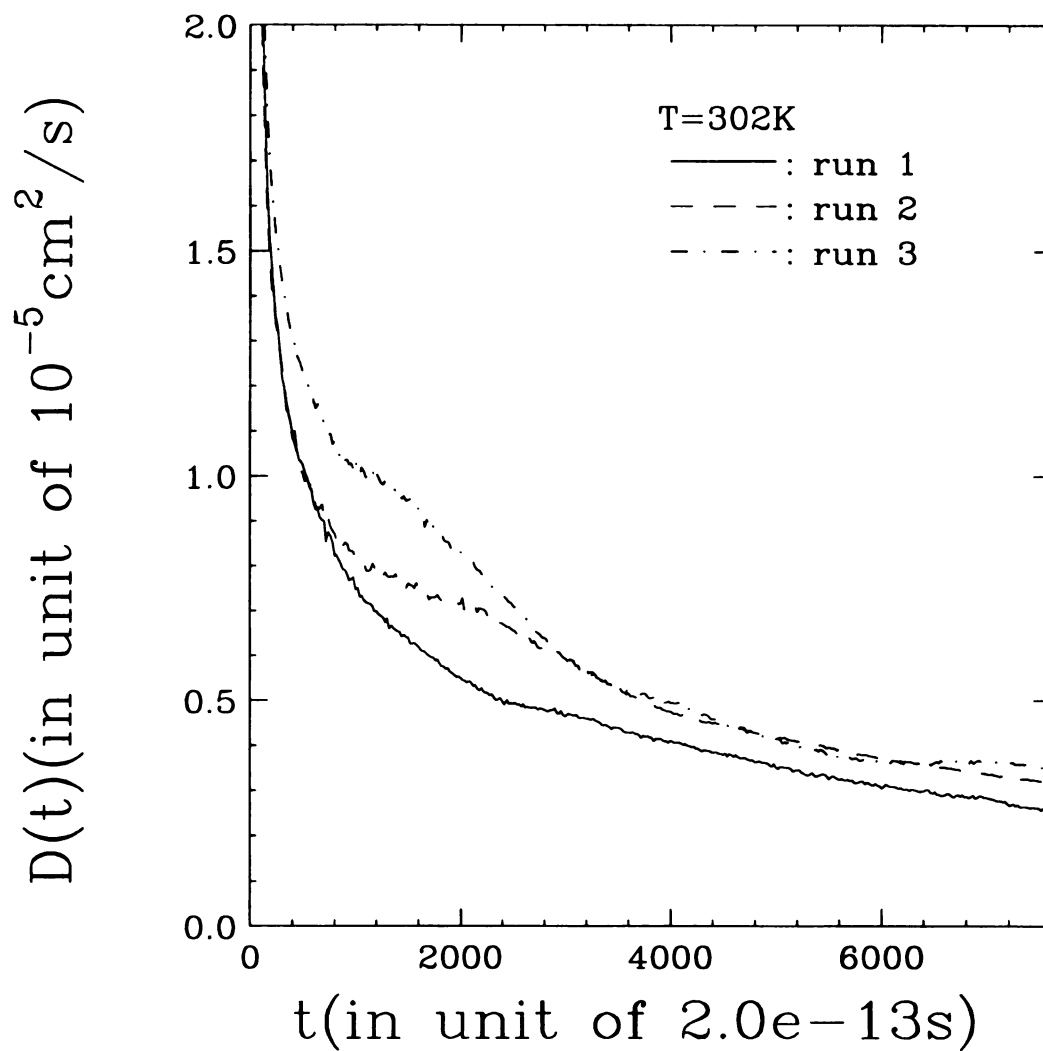


Figure 5.17: Diffusion rate $D(t)$ vs. time for the Xe_{6CAM} system

the six ring atoms it is possible to miss this transition for small MC steps/particle. But with increasing number of MC steps the chance of accepting the move which would dislodge the particle becomes more probable thereby causing the melting temperature to shift to a lower value. For increasing number of runs the 'melting' asymptotically becomes a continuous process as it should be but with a rapid change (with T) in δ determined purely by the equilibrium canonical distribution. If one can relate the MC steps to the actual time scale in which a real time experiment is performed, then depending upon the waiting time one should see different transition temperature as observed in our simulation. In addition if one experimentally probes the dynamics of Xe atoms, say through NMR, one should see two distinct type of dynamics: one associated with the correlated hopping of Xe atoms from one ring site to the other and the second associated with the intercage motion of the excited 'odd' atom of the (5-1) system. Xe_{6CAM} system shows a very well defined 'melting' curve. This is because that the system has a rather stable structure. The inter-cluster interaction reduces the fluctuations and its effects are seen clearly when we study the diffusion of the system, namely the inter-cage diffusive motion is dramatically suppressed in the Xe_{6CAM} system.

Chapter 6

Percolation and Diffusion in 2D Microporous Media: Pillared Clays

6.1 Introduction

Although adsorption and diffusion of gases in porous media have been the subject of investigation since the beginning of the century, it is only in recent years that any fundamental understanding of the underlying physical processes have begun to emerge[98]. As we have already discussed in the earlier chapters, a simple way to incorporate the effects of a porous medium on the dynamical properties of particles moving through it is through geometrical constraints. These constraints can not only alter these dynamical properties drastically but their thermodynamic properties as well. For example, in a macroporous medium one sees capillary condensation of the adsorbed gas to a liquid phase at a pressure which is less than the bulk saturated vapor pressure, a result of the shifted gas-liquid transition temperature caused by the confining geometry [99]. The diffusion rates both in the gas and the liquid phases are also known to be profoundly affected by the porosity leading, in certain cases, to the phenomena of percolation [100].

Until now we have been looking at one-dimensional microporous systems such as zeolites. Now we shift our attention to two-dimensional microporous system. A novel class of porous media that has been also of great interest during the last decade or so are pillared clays and related complex layered oxides. In this systems the guest particles diffuse between host layers held apart by laterally spaced pillaring agents. Pillared clays, in general, are intercalation compounds obtained by intercalating large pillaring ions into the galleries of layered oxides such as vermiculite [101], fluorohectorite [28], and montmorillonite [101]. Intercalation implies the insertion of guest species into a layered material without disturbing the main structural features of the host [102]. Intercalation compounds have been of interest for many years [6, 7, 20, 27, 103, 104] in part because they provide a two dimensional(2D) arena for both theoretical and experimental studies of many physical properties such as diffusion, percolation, commensurate-incommensurate structures, 2D-melting on corrugated substrates, 2D magnetic phase transition and so on. In clay intercalation compounds (CIC's), the host layers are highly rigid towards transverse distortion. In fact, one needs a large transverse layer rigidity to form good MP medium, otherwise the host layers will collapse around pillaring ions thereby precluding gallery access.

In almost all the CIC's there are fixed negative net charges in the layers which are compensated by counter ions in the intralamellar gallery space. These clays have the ability to be intercalated by guest ions or intercalants through ion-exchange mechanism [38, 105]. When the guest ions are of nanoscopic dimensions the resultant pillared clay is characterized by host layers that are propped apart by these laterally spaced guest ions, sometimes called pillars. The lateral separation between these guest ions can range from a few Å to as large as 10-20

Å (considerably larger than their lateral size) thus giving a well characterized 2D MP system with varying degree of microporosity. The specific sites where these intercalants reside depend on the charge of the intercalants, their lateral size and the commensuration energy associated with the interaction of the intercalants with the atoms of the host layers.

In this chapter, we model a real physical system representing such a 2D MP system (section 6.2), and then briefly discuss the experimental results on adsorption [38] and diffusion [28] carried out in this system (section 6.3). We introduce in section 6.4, microscopic lattice models with different levels of physical reality to characterize the microporosity, probe diffusion and percolation of particles moving in this MP medium using simulation techniques and compare our results with experimental measurements wherever available. Finally we give a brief summary of this work in section 6.5.

6.2 Physical system and the geometrical model

Mixed ion (or Heteroionic) clays with different size intercalants occupying specific gallery sites are excellent models of 2D MP media. Examples of such systems in which adsorption and diffusion measurements can be performed are ternary intercalated layered silicates $A_x B_{1-x} - Y$, where Y is the host layer; A and B represent the gallery cations which have different sizes [28, 38, 104, 105]. One usually studies the diffusion of a neutral guest species C (for example He, Ar) inside this 2D MP medium [28, 103]. An example of such MP medium is $[Cr(en)_3^{3+}]_x [Co(en)_2^{3+} - en]_{1-x} - FHT$, where FHT stands for fluorohectorite, a layered silicate, and the intercalants are Cr and Co complexes with en ligands.

The geometrical characteristics of the mixed-ion systems are the following: The precise positions and the structure of the intercalants inside the gallery of FHT are not known. However, from the X-ray measurement of the in-plane packing of the intercalants (pillars) in smectic clays as a function of relative pillar charge (pillar ion charge/clay surface charge ratio), there is strong evidence that the intercalants form a triangular lattice [106]. From a physical point of view it is reasonable to assume that the intercalants form an incommensurate triangular lattice. The size of the intercalants $Cr(en)_3^{3+}$ and $Co(en)_3^{3+}$ are $\sim 5.4A^0$ compared to the lattice constant $a \sim 5.2A^0$, where a is a measure of the size of the hexagonal cage of the substrate Kagomé network of O-atoms. In fact, the Ar and N_2 adsorption data [38] shows that the lateral size of these complexes are slightly larger than $5.4A^0$. Thus, one expects the substrate commensuration energy to be rather small. This is in contrast to the well known alkali-graphite intercalation compounds [27, 107]. If we neglect, in the leading order, the effect of substrate corrugation, then we have a system of (3+) ions interacting via unscreened Coulomb interaction. The ground state structure of such a system is known to be a triangular lattice. Consequently, we can model the $[Cr(en)_3^{3+}]_x[Co(en)_2^{3+} - en]_{1-x} - FHT$ system as a triangular net whose sites are randomly occupied by $Cr(en)_3^{3+}$ and $Co(en)_3^{3+}$ ions, the lattice constant being $10.22A^0$.

In order to characterize the microporosity, we will briefly review the discussion presented by Cai et.al.[103]. Assuming that the intercalants(to be denoted as cations for simplicity) A, B and the diffusing molecule C can be represented by cylinders with (diameter,height) given by (d_A, h_A) , (d_B, h_B) , and (d_C, h_C) , one

can define a set of porosity parameters by the following:

$$s_1 = \Theta\left[\frac{a - d_A}{d_C}\right]$$

$$s_2 = \Theta\left[\frac{a - d_A/2 - d_B/2}{d_C}\right]$$

$$s_3 = \Theta\left[\frac{a - d_B}{d_C}\right]$$

$$s_4 = \Theta\left[\frac{h_A}{h_C}\right]$$

$$s_5 = \Theta\left[\frac{h_B}{h_C}\right]$$

where the function $\Theta(x) = 1$ if $x > 1$, $\Theta(x) = 0$ if $x < 1$, and a is the distance between two nearest neighbor(nn) cations which are assumed to form a triangular lattice. Although the ideas presented here are not restricted to a triangular lattice, we will argue later that for the physical systems we have studied, a triangular lattice is the appropriate model. If C can pass between two nn A cations laterally, then $s_1 = 1$, otherwise $s_1 = 0$. Similar definitions can be given for s_2 and s_3 which are the other two lateral porosity parameters. The parameters s_4 and s_5 describe the vertical porosity of the MP medium. We however note that the transverse rigidity of the host layers can significantly alter the definition of these vertical porosity parameters. For a given system, the diffusion of the guest particle C is controlled by the above set of five porosity parameters. Depending on the values of s_i 's, one can have no diffusion, complete diffusion, one or two percolation thresholds [103] in the system $A_x B_{1-x} - Y$ as one changes x from $0 \rightarrow 1$. Our physical system was modeled with the assumption that the heights of the intercalants and the guest species do not influence the diffusion in the plane, ie. we take $s_4 = 1$ and $s_5 = 1$. Later we will argue that this is reasonable

for the systems under study. Thus there are only three relevant lateral porosity parameters $s = (s_1, s_2, s_3)$ left to deal with.

Rare gas adsorption [38] and diffusion [28] experiments were done in heteroionic pillared clay $[Cr^{3+}(en)_3]_x[Co^{3+}(en)_3]_{1-x}$ - FHT, where en is ethylenediamine ligand. This system has the following properties: At room temperature $Co(en)_3^{3+}$ and $Cr(en)_3^{3+}$ have the same diameters and height ~ 5.4 Å. They prop up the gallery of FHT to a height of ~ 5.4 Å and the average distance between two adjacent intercalants is about 10.22 Å. This allows atoms like Argon ($d_C \equiv d_{Ar} = 4.0$ Å [28]) and Helium ($d_C \equiv d_{He} = 2.6$ Å [25]) to pass through the space between AA, BB and AB pairs of intercalants, ie. $s=(1,1,1)$. When the system is heated to a temperature somewhere between 100C to 150C, $Co^{3+}(en)_3$ complex breaks into $Co^{3+}(en)_2 + (en)$, which has smaller vertical dimension (about 3.8 Å) and larger lateral dimension (> 6 Å) than the parent cation. The $Cr^{3+}(en)_3$ cations remain unchanged during heating. So if one takes a system $[Cr^{3+}(en)_3]_x[Co^{3+}(en)_3]_{1-x}$ - FHT and heats upto a temperature between 100°C and 150°C, the resultant system becomes $[Cr^{3+}(en)_3]_x[Co^{3+}(en)_2 + (en)]_{1-x}$ - FHT. Using the values of the lattice constants and diameter of the pillars and the diffusing particles, we find that for Argon atoms $s=(0,0,1)$, whereas for Helium atoms $s=(1,1,1)$ and remains unchanged. This implies that Argon atoms can pass only through two nn $Cr^{3+}(en)_3$ (see fig.6.1), and therefore in this case there exists a threshold x_c such that the Argon atoms can not diffuse through the system at all when $x < x_c$, ie. one should see one percolation threshold as observed in adsorption measurements [38]. Z. X. Cai [108] used lattice model simulation and I have used continuum diffusion simulation to probe this percolative property. In section 6.4, I will introduce both

the models and compare the simulation results with experiments.

6.3 Review of experimental situation

Before we discuss the details of our simulations, we briefly review the experimental situation. Two types of studies have been done [28, 38]. (1) Mass adsorption measurement were carried out [38] where the mass uptake of Argon in the system $[Cr^{3+}(en)_3]_x[Co^{3+}(en)_2 + (en)]_{1-x} - FHT$ was measured (see fig.6.2) as a function of x at room temperature. The measurements show that for $0 < x < 0.8$, the system does not take up Argon except for some background effects whose cause is not completely known. As x exceeds 0.8, there is a rapid increase in the mass uptake indicating that the system begins to open up to Argon which can diffuse through the system and get adsorbed at available sites. (2) Diffusion experiments were carried out [28] where the diffusive property of Argon and Helium gas was measured at room temperature in both unannealed $Co^{3+}(en)_3 - FHT$ and annealed $Co^{3+}(en)_2 + (en) - FHT$ films. These two systems have the same effective properties as the $x=1$ and $x=0$ limits of the mixed system $[Cr^{3+}(en)_3]_x[Co^{3+}(en)_2 + (en)]_{1-x} - FHT$, because the unannealed $Co^{3+}(en)_3$ has the same dimensions as $Cr^{3+}(en)_3$. Helium gas was found to diffuse through both the systems but with different saturation time (t_s) [28], 30s. and 1800s. respectively [109]. The corresponding diffusion constants (D) were estimated to be $\sim 10^{-6} cm^2/s$ and $10^{-8} cm^2/s$. On the other hand Argon gas could diffuse only through the unannealed system, i.e. when $x=1$, with $t_s = 2600s$, and $D \sim 10^{-8} cm^2/s$. No Argon diffusion was detected in the annealed system i.e. when $x=0$.

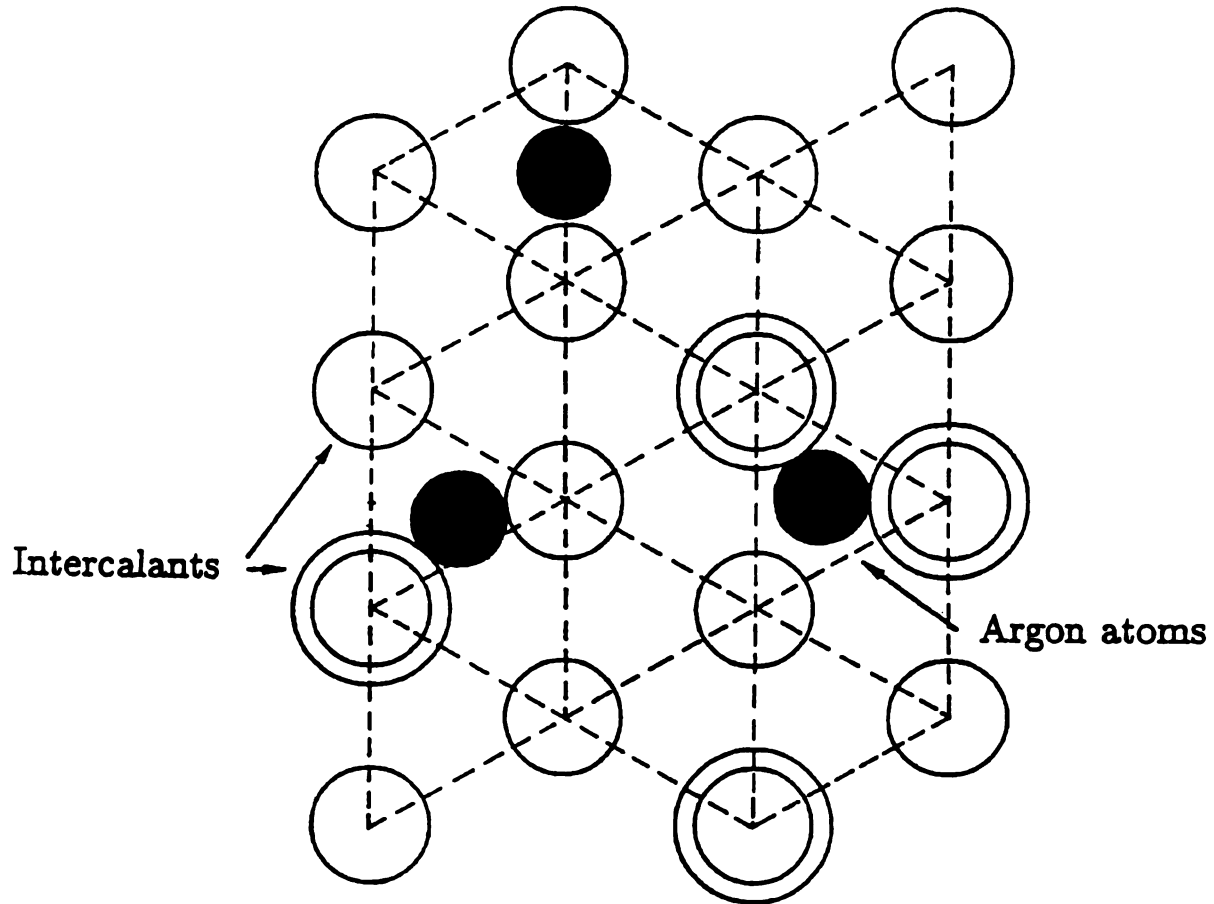


Figure 6.1: Argon atoms diffusing in the annealed $[Co^{3+}(en)_3]_{1-x}[Cr^{3+}(en)_3]_x - FHT$. Single circles represent $Cr^{3+}(en)_3$. Concentric circles represent $Co^{3+}(en)_3$ where smaller circles are for the ions before annealing and larger circles are for the ions after annealing.

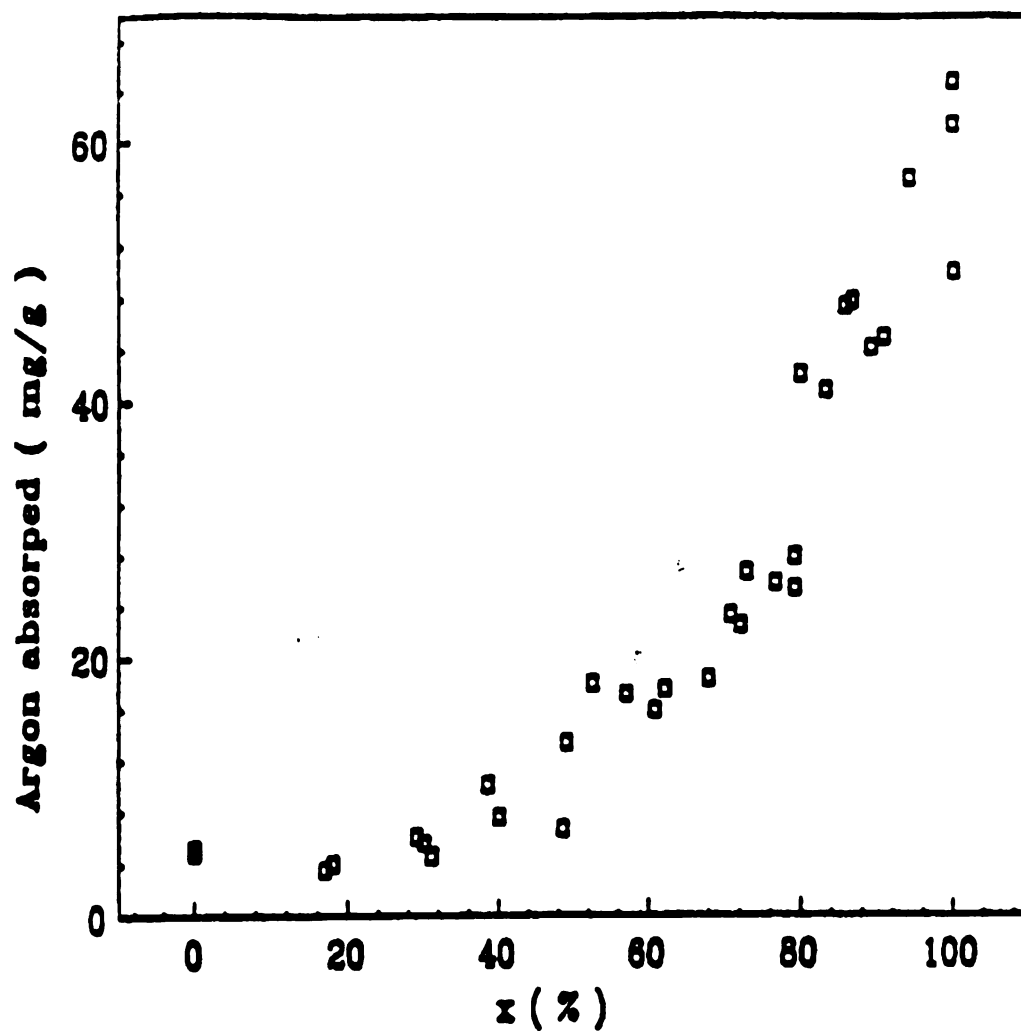


Figure 6.2: The amount of Argon adsorbed by $[Co^{3+}(en)_3]_{1-x}[Cr^{3+}(en)_3]_x - FHT$ as a function of x. [38]

6.4 Results of computer simulation

To understand the adsorption, diffusion and percolation in the above system, we have constructed models with different levels of sophistication and have studied the diffusion and percolation properties using different computation techniques. The simulations were done on a triangular lattice where the $Cr^{3+}(en)_3$ and $Co^{3+}(en)_2 + (en)$ cations were randomly distributed on the triangular lattice sites with probability x and $1-x$ respectively.

6.4.1 Lattice model

A simple lattice model was constructed by Cai and Mahanti [108] to see if one can understand the sharp rise in the Ar adsorption near about 80% concentration of $Cr^{3+}(en)_3$ intercalants. The $Cr^{3+}(en)_3(A)$ and $Co^{3+}(en)_2 + (en)(B)$ complexes were assumed to occupy the triangular lattice sites randomly. They further assumed that only AA bonds are large enough so that Argon atoms(see fig.6.3) can diffuse through it and get adsorbed near these bonds. Thus if we look at the dual honeycomb lattice(DHL), a bond is open or closed depending on whether two sites of the triangular lattice on the two ends of this bond have A atoms or not. We assume that when the open bonds on the DHL percolate then only there is significant Ar adsorption. The rationale behind the assumption is that one needs access before adsorption in macroscopic scale can occur. However as will be discussed later, this assumption may not be completely correct and one sees observable macroscopic adsorption even below this threshold. Here we consider this type of adsorption as background effect.

For the A_xB_{1-x} system when $x < 0.5$, one does not have an infinitely perco-

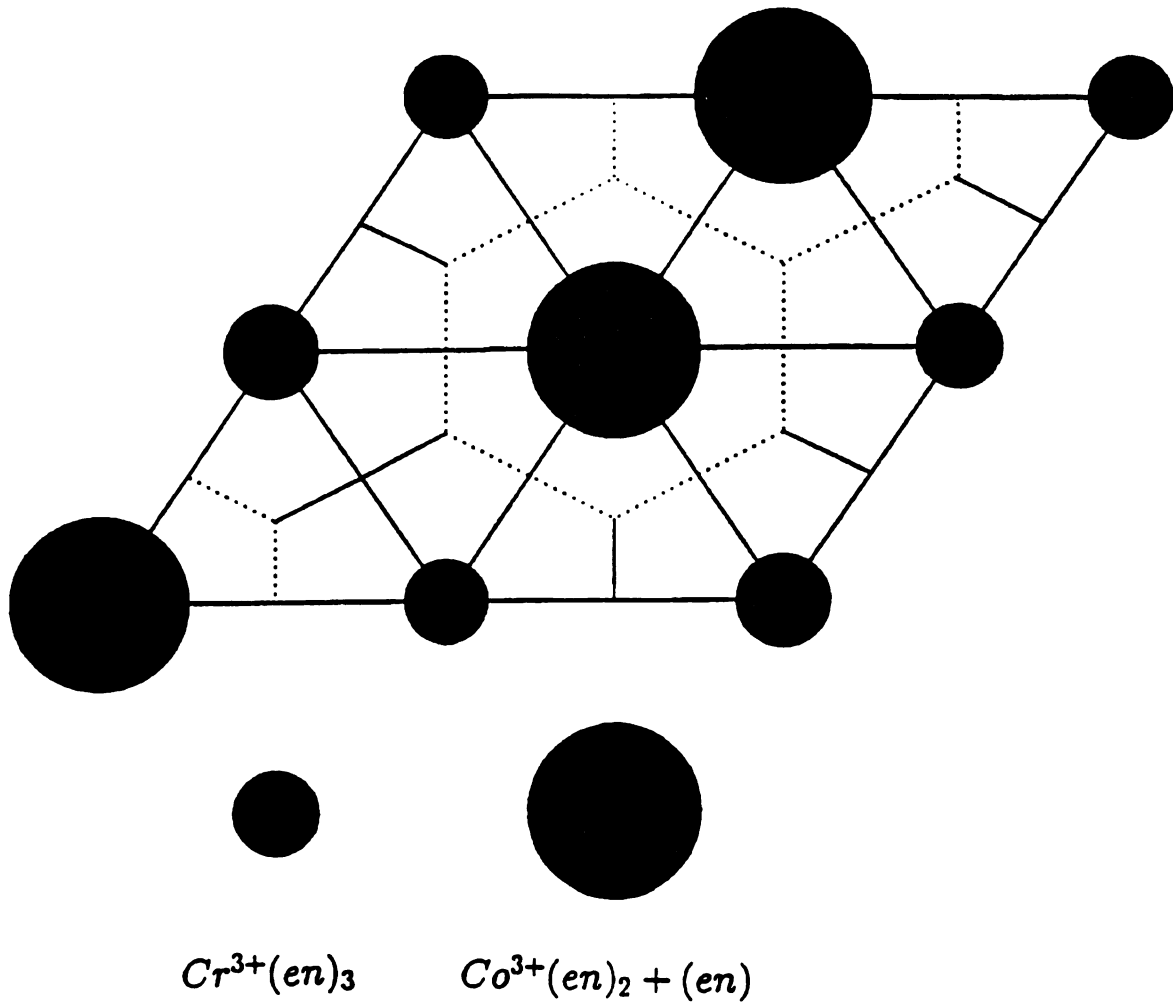


Figure 6.3: Lateral constraints on Argon atoms diffusing in the annealed system $[Co^{3+}(en)_3]_{1-a}[Cr^{3+}(en)_3]_a - FHT$. The dashed lines are closed bonds and the solid lines are open bonds of the honeycomb lattice on which the Argon atoms is diffusing.

lating A cluster. For $0.78 > x > 0.5$, although we have a infinite percolating A cluster, the concentration of AA bonds is not large enough for the corresponding bond percolation to occur on the DHL. In fig.6.4, we plot the fraction of AA bonds i.e. the fraction of open bonds(P) on the DHL belonging to the infinite percolating cluster for different lattice sizes. Near $x \approx 0.78$ one sees the usual rapid increase of P with x and we estimate the percolation threshold x_c to be $0.78 < x < 0.80$. For the following discussion we take $x_c = 0.79$.

Now let us compare the pure bond percolation on the honeycomb lattice with the above percolation threshold. Associating the sites of the triangular lattice with a variable σ_i such that $\sigma_i = 1$, if the site i is occupied by an A atom, and $\sigma_i = -1$, if it is occupied by an B atom, we can define a parameter b_{ij} associated with the bond between site i and site j (or equivalently the bond on the DHL). The parameter $b_{ij} = 1$, if the bond is open, $b_{ij} = 0$, if the bond is closed. The relation between b_{ij} and σ_i 's is

$$b_{ij} = \frac{1}{4}[1 + \sigma_i + \sigma_j + \sigma_i\sigma_j], \quad (6.1)$$

and

$$\langle b_{ij} \rangle = x^2 \quad (6.2)$$

where we have used $\langle \sigma \rangle = (2x - 1)$, x being the concentration of A atoms, and $\langle \sigma_i\sigma_j \rangle = \langle \sigma_i \rangle \langle \sigma_j \rangle$.

Since the bond percolation threshold for a honeycomb lattice is 0.6527 [110], from Eqn. 6.2 we find that $x_c^2 = 0.6527$, which gives $x_c = 0.8079$. This is slightly larger than our result 0.79 for x_c . Equivalently, the latter gives a lower percolation threshold (~ 0.6241) for the DHL. The reason for this is that the bonds on the

DHL are not statistically independent but are correlated instead. The correlation between two adjacent bonds b_{ij} and b_{ik} is found to be:

$$\langle b_{ij}b_{ik} \rangle - \langle b_{ij} \rangle \langle b_{ik} \rangle = x^3(1 - x) \quad (6.3)$$

This correlation is positive and is relatively large near $x \approx 0.75$ ie. if a bond (ij) is open then (ik) has a slightly more probability of being open than when the bonds are randomly open or close. This results in the percolation threshold being smaller by $\sim 4\%$ compared to the random case(0.6527).

The percolation threshold at $x_c = 0.79$ is close to the concentration $x \simeq 0.8$ where one sees a sudden increase in the Ar adsorption experiment. The uncertainty in the experimental x values is much larger than 4% to distinguish between correlated and random bond percolation. However we believe that we have captured the essential microscopic picture underlying the adsorption process in these 2D microporous systems. In the following section we confirm this picture by studying the diffusion of Ar and He atoms using a slightly more realistic model of the MP medium.

6.4.2 Continuum diffusion

Recently, a novel approach has been introduced to study the diffusion and transport properties of physical systems where the true continuum structure is maintained [111]. The random walk algorithm is used to calculate the diffusion constant in this approach and we believe that this is a more realistic approach to probe the microporosity of the pillared lamellar systems which have been studied experimentally. We apply this method to calculate D for the system shown in fig.6.1. We allow a walker to land at a random location on the system. If the walker

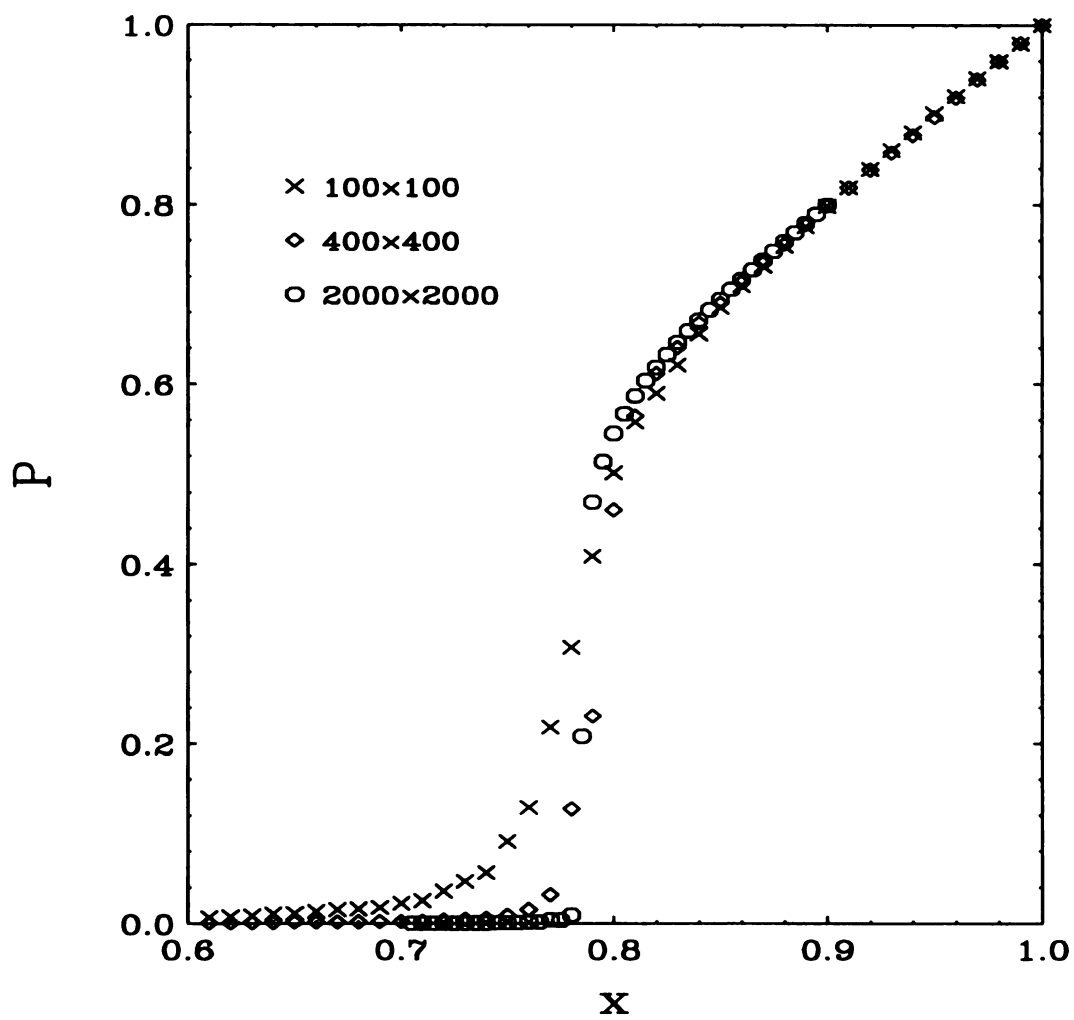


Figure 6.4: The x dependence of the size of the largest cluster of A-A bonds obtained from simulation of 100×100 , 400×400 and 2000×2000 lattices (averaged over 10 different configurations for each lattice).

lands on a pillar, it dies and is removed, if it lands on the remaining part of the system, it begins to diffuse. The effective sizes of the pillars are taken to be either $(d_A + d_C)$ or $(d_B + d_C)$ and the walker is assumed to be a point object. The step length (l) of the walker is fixed to be 0.1 in the unit of the lattice parameter(a), but the direction of the step is picked randomly. The walker moves one step along that direction. If the walker hits a pillar during its diffusive motion, it stays at its original place, but the clock advances one step forward. The diffusion constant D is then obtained from the distance(R) that the walker travels in a time t via the relation

$$R^2 = 4Dt \quad (6.4)$$

The diffusion constant for a particle freely diffusing in 2D in the absence of any pillar is simply

$$D_0 = \frac{1}{4}l^2 \quad (6.5)$$

We have calculated the relative diffusion constant D/D_0 for different $Cr^{3+}(en)_3$ concentrations x in the system $[Cr^{3+}(en)_3]_x[Co^{3+}(en)_2 + (en)]_{1-x} - FHT$ for both Argon and Helium atoms. Because the diameter of He($\sim 2.6 \text{ \AA}$) is much smaller than that of Ar($\sim 4.0 \text{ \AA}$), the diffusion property of He is quite different from that of Ar. We chose a 50×50 triangular lattice, and our results were obtained by averaging over 50 configurations of the $A_xB_{1-x} - FHT$ system for a given x and 20 random walkers in each configuration for Argon and 50 walkers in each configuration for Helium. The number of steps taken was typically $\sim 10^6$. We have taken the diameter of both $Cr^{3+}(en)_3$ and $Co^{3+}(en)_3$ to be $5.4 \text{ \AA}(d_A)$, and the diameter of $Co^{3+}(en)_2 + (en)$ to be $7.2 \text{ \AA}(d_B)$. Since the lattice parameter

of the triangular lattice is $a = 10.22 \text{ \AA}$ [28], Ar atoms can only pass through AA bonds while He atoms can pass through all the bonds as suggested from the measurements of Zhou [28]. Fig. 6.5 shows the typical curves for R^2 and D/D_0 vs. the number of time steps

We obtain the following results from our simulation.

(1). The relation between the relative diffusion constant of Argon atom ($d_{Ar} = 4.0 \text{ \AA}$) and the concentration x of $Cr^{3+}(en)_3$ in $[Cr^{3+}(en)_3]_x[Co^{3+}(en)_2(en)]_{1-x}$ -*FHT*. Note that as the porosity of the system becomes smaller, more paths with narrow necks (such as BB bond) contribute to D and therefore the step length should be chosen smaller to properly access these narrow neck regions. But this will consume enormous computer time. We have checked the dependence of D/D_0 on l and find that D/D_0 increases with decreasing l and saturates for small enough value of l (see fig. 6.6). As a compromise between small l (hence long computer time) and large l (less accuracy of D/D_0), we have chosen $l = 0.1$ (in unit of the lattice parameter). This value of l is sufficient to give accurate information about D/D_0 for He (within 5 ~ 10%) when x is near 1, whereas for Ar and for He near $x \sim 0$ one can make appreciable error. To check this we studied D/D_0 for Ar when $x = 1$ by taking several values of l from 0.1 to 0.01. We find that D/D_0 increases by about 30% as we decrease l from 0.1 to 0.01. Thus we estimate of D/D_0 for Ar is reliable up to 30%. Clearly one needs a more careful calculation of D/D_0 by either choosing a smaller value of l or by using a completely independent method. Fig. 6.7 gives our calculated values of D/D_0 vs. x (expressed in %). We clearly see the percolation threshold near 77% is consistent with the $x_c = 0.78$.

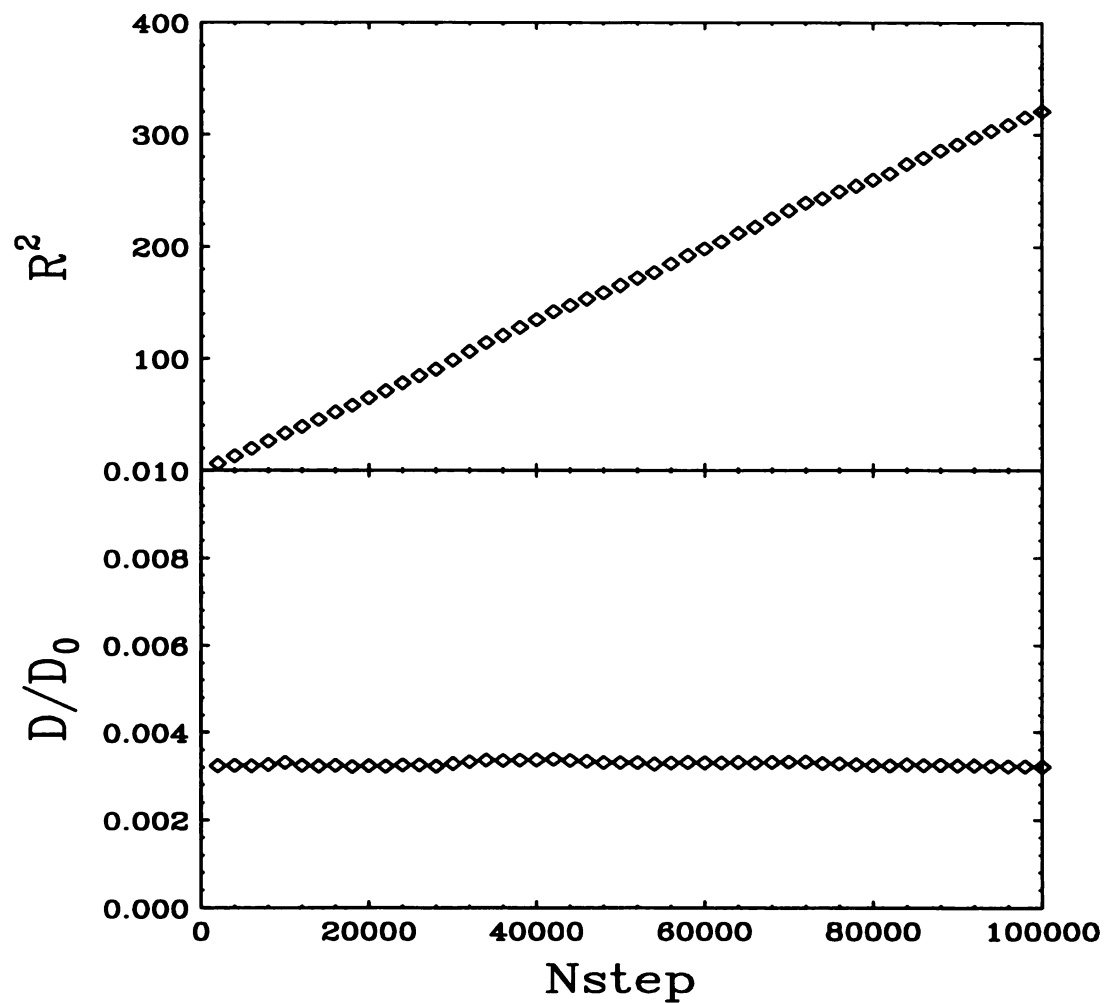


Figure 6.5: Typical curves of R^2 and D/D_0 vs. time steps for Ar atoms diffusing in $50 \times 50 [Cr^{3+}(en)_3]_x [Co^{3+}(en)_2 + (en)]_{1-x}$ - *FHT* lattice. $x = 1$. Step length is 0.1 (in unit of the lattice parameter). Total step is 10^5 . We averaged over 50 configurations and 50 random walkers.

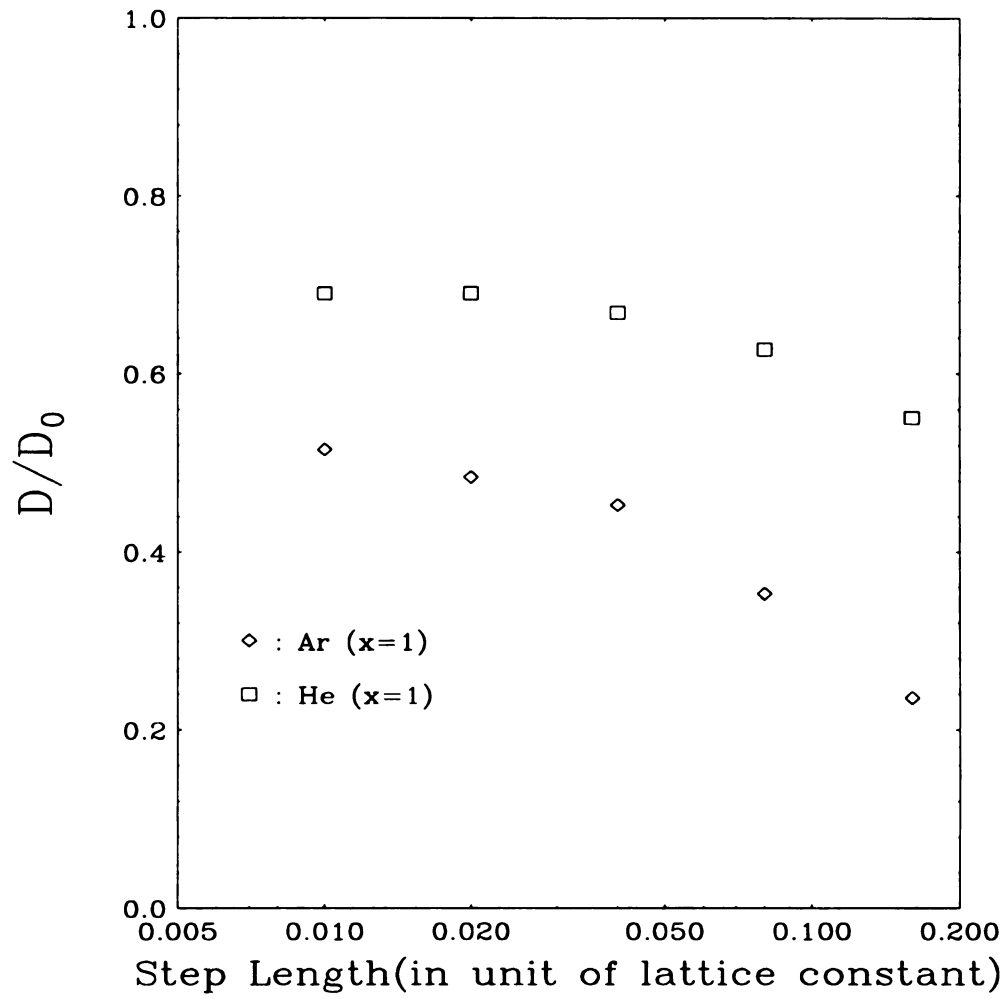


Figure 6.6: D/D_0 vs. step length for Ar($x=1$) and He($x=0,1$)

(2). The relation between the relative diffusion constants of Helium atom ($d_{He} = 2.6 \text{ \AA}$) and the concentration x of $Cr^{3+}(en)_3$ in $[Cr^{3+}(en)_3]_x[Co^{3+}(en)_2 + (en)]_{1-x} - FHT$. This is shown in fig.6.8.

(3). Because the dimension of Helium atom varies a lot from literature to literature, we have also calculated the Helium size dependence of $D^{He}(x=0)/D^{He}(x=1)$. This result is plotted in fig.6.9. As we can see in this figure, for Helium diameter larger than $\sim 3.02 \text{ \AA}$, there is no diffusion in the $x=0$ system and there is a rapid decrease of $D^{He}(x=0)/D^{He}(x=1)$ near this critical diameter.

6.4.3 Comparison with experiment and discussion

From fig.6.7, we see that in order for Argon atoms to pass through the annealed $[Cr^{3+}(en)_3]_x[Co^{3+}(en)_2 + (en)]_{1-x} - FHT$ system, the concentration of $Cr^{3+}(en)_3$ must be greater than 0.78, which is in good agreement with the lattice simulation results ($x_c \sim 0.79$) and experiment (~ 0.8).

The diffusion results shown in fig.6.8 show that for this particular Helium size ($d_{He} = 2.6 \text{ \AA}$), Helium gas can diffuse through this system for all concentrations (x) with $D^{He}(x=0)/D^{He}(x=1) \approx 0.35$. But experimental estimate gives this ratio to be almost $\sim 10^{-2}$. This large discrepancy is difficult to understand. One possibility is because of the large value of D_{He} for $x=1$, the equilibration time is so short that there may be a problem with estimating the experimental value of D accurately for this concentration. Secondly, because of the very small porosity for $x=0$, there may be quantum effects which make the effective size of Helium atom larger than 2.6 \AA , thereby suppressing diffusion near narrow passage ways. Furthermore, the size of the Helium is in fact not a well defined quantity. Thus

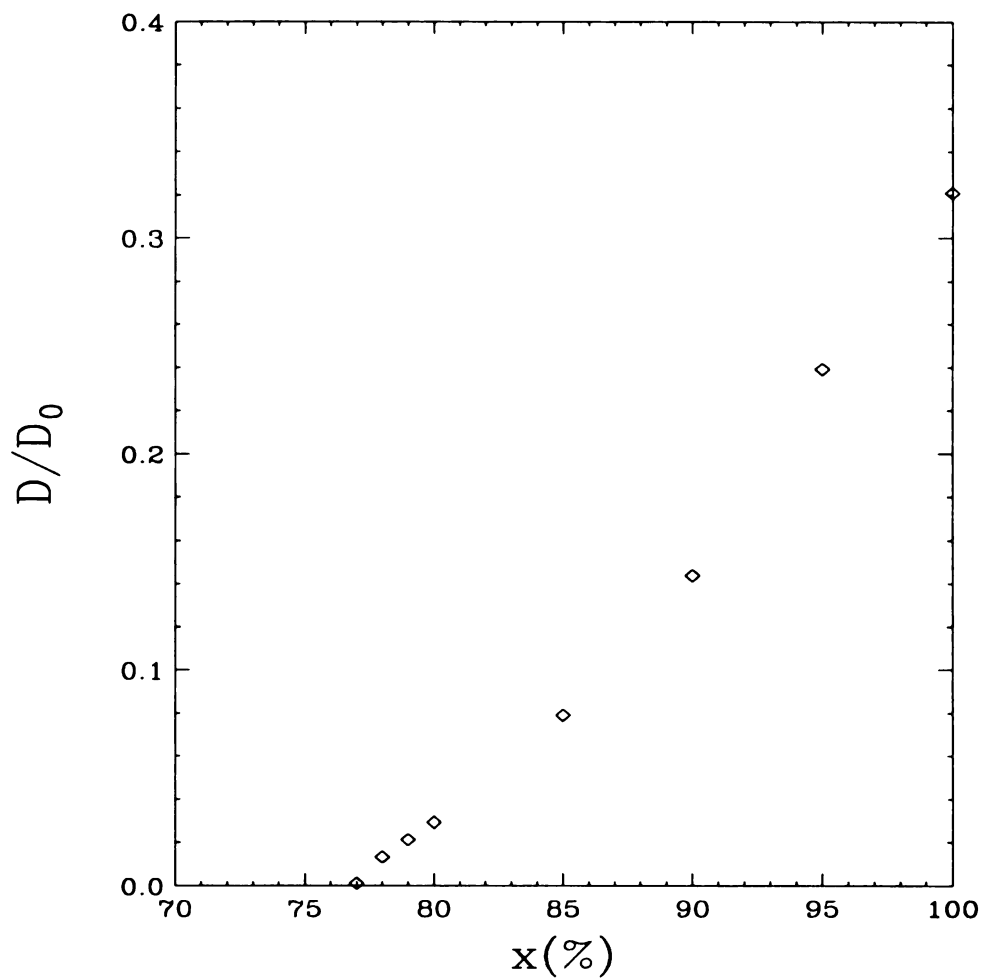


Figure 6.7: The relative diffusion constant of Argon atom ($d_{Ar} = 4.0 \text{ \AA}$) diffusing in $[Cr^{3+}(en)_3]_x[Co^{3+}(en)_2 + (en)]_{1-x} - FHT$ as a function of x , the percolation threshold $x_c \sim 0.78$.

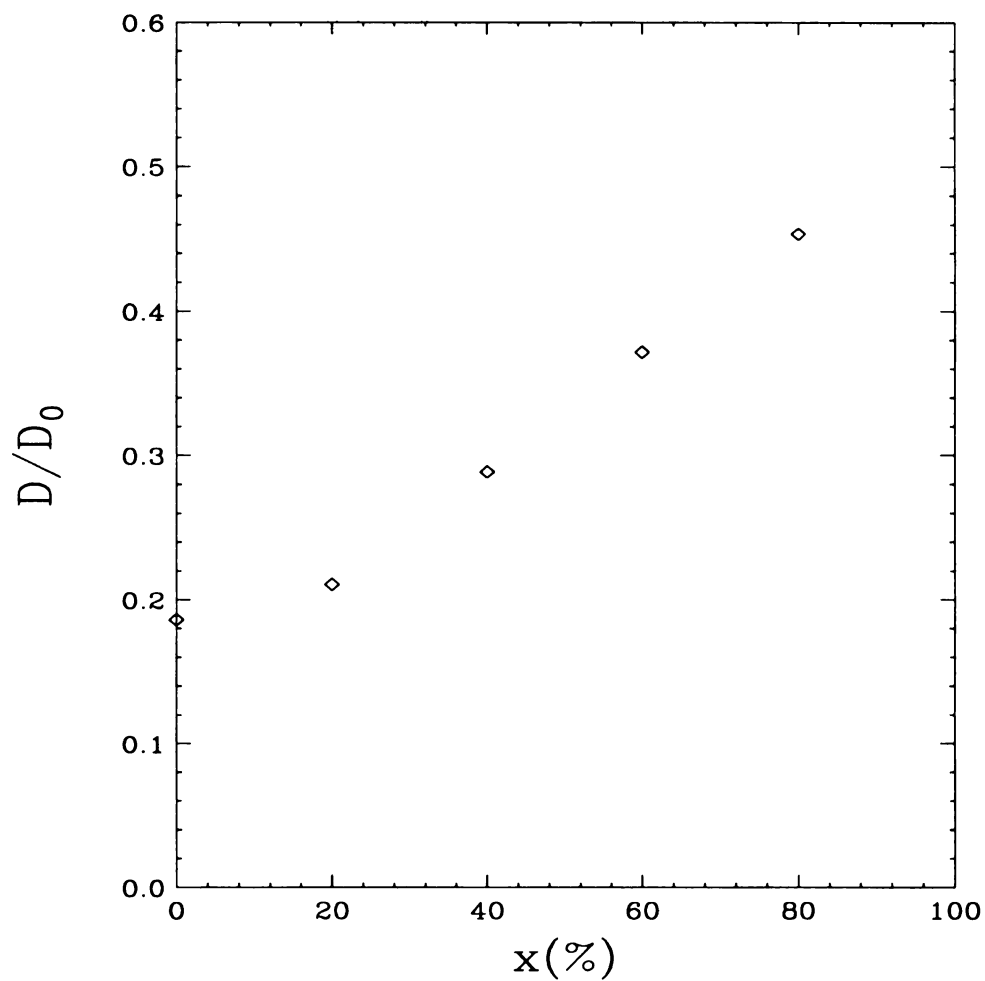


Figure 6.8: The relative diffusion constant of Helium atom ($d_{He} = 2.6 \text{ \AA}$) diffusing in $[Cr^{3+}(en)_3]_x[Co^{3+}(en)_2 + (en)]_{1-x} - FHT$ as a function of x . Helium gas can diffuse through the system for all x .

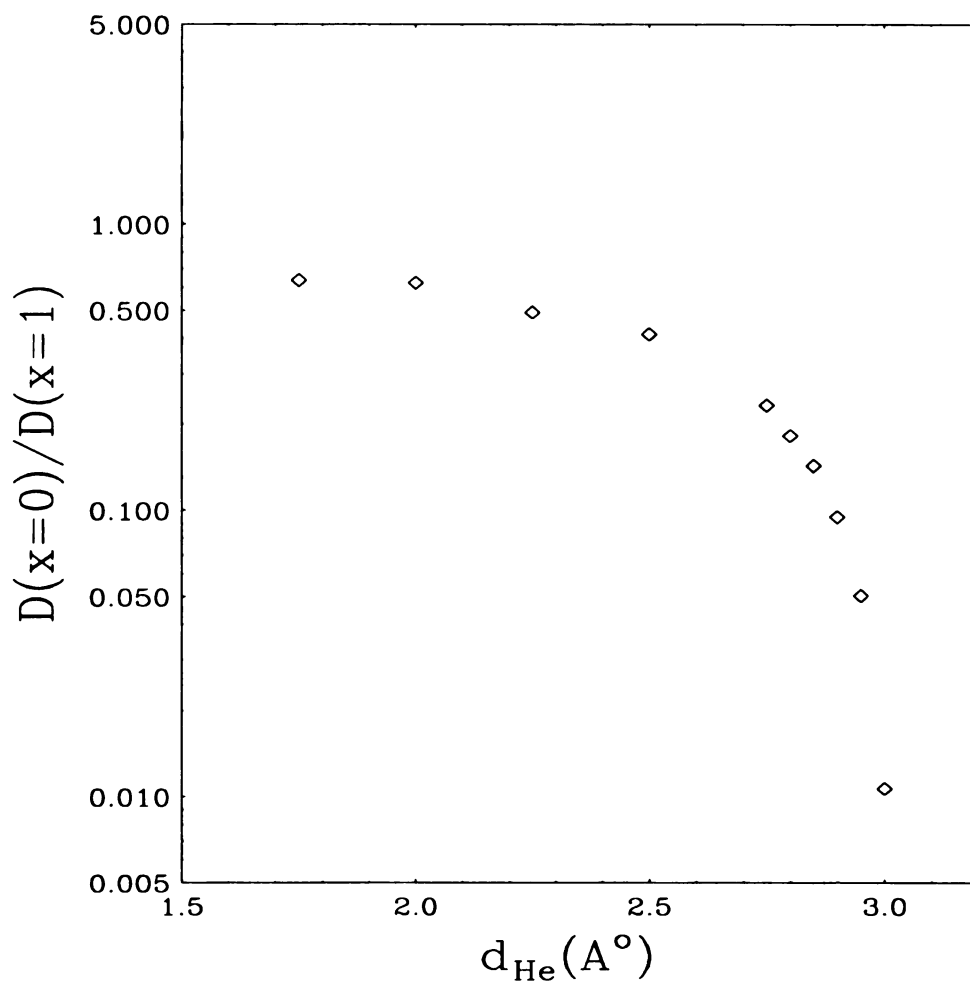


Figure 6.9: The ratio $D^{\text{He}}(x=0)/D^{\text{He}}(x=1)$ as a function of the diameter of Helium atom when Helium gas diffuses in $[\text{Cr}^{3+}(\text{en})_3]_x[\text{Co}^{3+}(\text{en})_2 + (\text{en})]_{1-x}$ - *FHT* system.

there is a possibility that the actual size of Helium atom is larger than what we have used. From fig.6.9, we can see that the value of d_{He} is in the range where the ratio $D^{He}(x=0)/D^{He}(x=1)$ decrease rapidly with d_{He} . Even a small change in d_{He} , or by increasing the size of the big pillars slightly (from 7.2 Å → 7.6 Å), one can cause a very large change in this ratio which can then explain the experimental observation. What it means physically is that the system containing all large pillars is very near the critical threshold for He diffusion.

Finally there is another phenomena which needs to be addressed. It was found experimentally that D_{He} for $x=0$ and D_{Ar} for $x=1$ were of the same order of magnitude and $D_{He}(x=0)$ was slightly larger than $D_{Ar}(x=1)$. However, our simulation gives $D_{He}(x=0)/D_0 \sim 0.19$ which is smaller than $D_{Ar}(x=1)/D_0 (\sim 0.32)$. The experimental observation can be understood by taking into account the mass difference between Argon and Helium atoms i.e. $M_{Ar}/M_{He} \approx 10$. In reality, there is a $1/M^{1/2}$ dependence of D [33] which has not been taken into account in our simulation and its inclusion can explain the experimental observation. This mass dependence can be indirectly incorporated through D_0 which is then different for He and Ar atoms. However the precise mass dependence of D_0 needs further study.

6.5 Summary

In summary, we have used two simulation methods to get some insight into the percolative properties of heteroionic clays. According to the above discussions, we suggest that more detailed experiments should be done for Helium gas diffusing in the annealed $[Cr^{3+}(en)_3]_x[Co^{3+}(en)_2(en)]_{1-x} - FHT$ system for different values

of x . Also an improved method is needed to calculate D , particularly when the porosity of the system is small. It may be necessary to incorporate quantum effects on diffusion because they may possibly be important near narrow constrictions. Finally, we would like to make some remarks on the large background observed in the adsorption measurements. There appears to be a rapid increase in the adsorption near $x = 0.5$ (see ref.[38]) where, as we discussed in sec.IV A, one should have an infinite percolating cluster of A ($Cr^{3+}(en)_3$) atoms. This may open up some gallery space where Ar atoms can get adsorbed although they cannot diffuse through the entire system. A more realistic model of adsorption phenomena is needed to check this idea.

Chapter 7

Conclusion

In the abstract, I have given a detailed summary of my thesis project. Here I briefly discuss the main projects and what further work needs to be done. As summarized in the abstract, I have investigated the thermodynamic and dynamic properties of both quantum and classical rare gas atoms and clusters confined inside microporous media. I have compared my theoretical results with experiments whenever possible and in most cases find a qualitative agreement.

For the mass transport of quantum particles inside K-L zeolite channels, single particle Schrödinger equation has been solved for simplified model of the channel geometry using finite difference iterative method for eigenvalue problems. For a more realistic potential model, this method is not suitable because of the complicated boundary conditions. In this case, quantum Monte Carlo simulation method may be more appropriate.

Extended Mott-Hubbard and Bose-Hubbard models have been used to probe the low temperature thermal excitations of helium clusters (bosons for ^4He and spinless fermions for ^3He) confined inside K-L zeolite cages and the effect of tunnelling disorder has been investigated. However, spinful fermion problem still

needs to be solved more accurately and the effect of disorder in single-site energies on the thermal properties should be explored. Furthermore, the dynamics of confined quantum clusters should be very interesting because they can be probed by inelastic neutron scattering measurements.

To study the 'melting' and dynamics of Xe clusters inside L-zeolite, classical Monte Carlo and MD simulations have been employed. Monte Carlo studies of melting bring out the difference between a single cluster and a cluster assembled material. However, for a better understanding of the dynamics, more extensive simulations have to be carried out. Finally, percolative properties of He and Ar atoms inside a model 2D microporous medium pillared heteroionic silicate clay have been studied using continuum classical MC simulations. It is possible that He atoms even at room temperature can show quantum effects on the diffusion rate because when they go through narrow constrictions, their de Broglie wave length may be comparable to the pore width.

Appendix A

Estimation of nearest neighbor He-He interaction in K-L Zeolite

We use the realistic geometry of the K-L zeolite cage to estimate the interaction energy between two helium atoms trapped inside K-L zeolite. There are nine K^+ ions in a unit cell of K-L zeolite and four of them are believed to be sitting near the wall of the cage while others are located inside the aluminosilicate framework. The four K^+ ions which are near the wall of the cage can interact with helium atoms and contribute to the binding energy of the He atoms in what we refer to as cage states. Experiment suggests that there are eight binding sites per-cage (or cage states) available to helium atoms. The schematic arrangement of the He atoms and K^+ ions is shown in fig. A.1. Fig. A.1(a) is the cross section of cage center in K-L zeolite. Fig. A.1(b) shows the arrangement of two He atoms bound near a K^+ ion.

He-He interaction can be affected by the presence of K^+ ions. The interaction between two helium atoms include two parts: (i) He-He direct L-J interaction: V_1 (ii) He-He indirect interaction through K^+ : V_2 , i.e. one He atom polarize the K^+ ion which then interacts with another He atom. We estimate the two

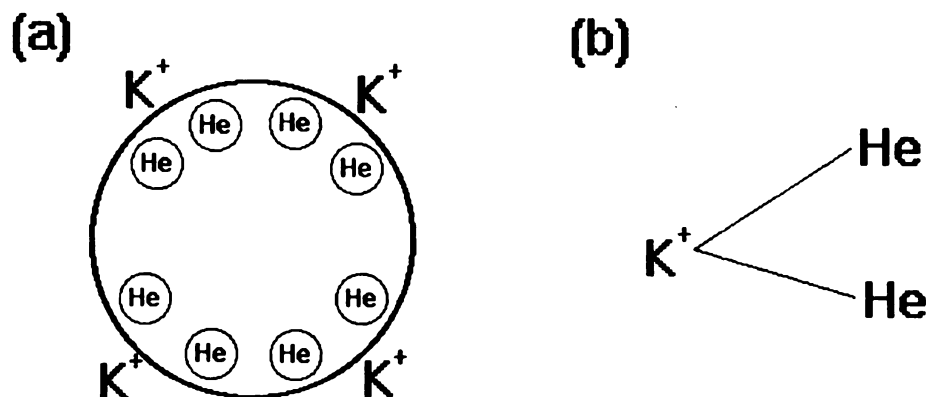


Figure A.1: A view of the geometrical arrangement of Helium atoms and K^+ ions of K-L zeolite cage.

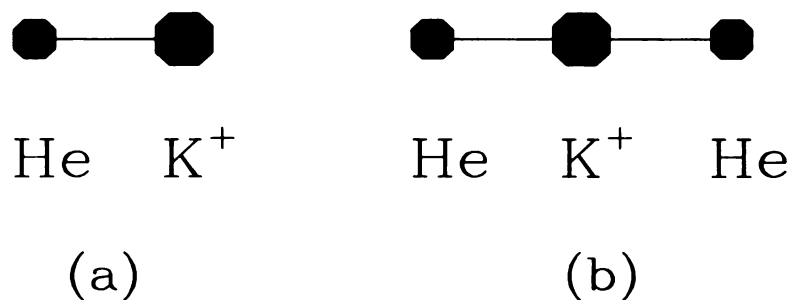


Figure A.2: (a) Shows the interaction between one Helium atom and K^+ ion. (b) shows the interaction between two Helium atoms and K^+ ion.

contributions V_1 , V_2 to the He-He using the following procedure:

(1) Estimation of V_1 :

In K-L zeolite, the diameter of the cage $d \simeq 13 \text{ \AA}$. The diameter of a He atom is $d_{He} \simeq 2.6 \text{ \AA}$. Putting 8 He atoms as show in fig.A.1(a), one estimate the average nearest neighbor separation between the He atoms $d_{He-He} \simeq 2.7 \text{ \AA}$. Also, the L-J parameters for He-He are: $\epsilon = 14e - 16erg$, $\sigma = 2.56 \text{ \AA}$. So, we estimate

$$V_1 = 4\epsilon \left[\left(\frac{\sigma}{d_{He-He}} \right)^{12} - \left(\frac{\sigma}{d_{He-He}} \right)^6 \right] \simeq -9K$$

(2) Estimation of V_2 :

To estimate this potential, we first have to have the He- K^+ effective L-J parameters. This can be estimated using the known results from quantum chemical calculation by Rao et.al. [112] for $He - K^+$ and $He - K^+ - He$ arrangements shown in fig.A.2(a), (b) (Fig. A.2(a) shows one He atom interacting with one K^+ ion. Fig. A.2(b) shows the interaction between two He atoms and one K^+ ion). The known results from quantum chemical calculations of binding energy ϵ_b and equilibrium bond length l_b are:

$$\epsilon_b^{He-K^+} = -12.0\text{mev}$$

$$l_b^{He-K^+} = 3.11\text{\AA}$$

$$\epsilon_b^{He-K^+-He} = -24.9\text{mev}$$

$$l_b^{He-K^+-He} = 3.18\text{\AA}$$

Using the above results for the He- K^+ interaction, we can estimate the effective L-J parameters. The He- K^+ interaction includes two parts. One is the K^+ -He polarization energy and the other is the K^+ -He L-J energy.

$$V^{K^+-He} = -\frac{\alpha_{He}e^2}{2(\tau_b^{He-K^+})^4} + 4\epsilon\left[\left(\frac{\sigma_{He-K^+}}{\tau_b^{He-K^+}}\right)^{12} - \left(\frac{\sigma_{He-K^+}}{\tau_b^{He-K^+}}\right)^6\right],$$

where $\alpha_{He} = 0.205\text{\AA}^3$ is the He atom polarizability. This potential energy V^{K^+-He} should be equal to the known value $\epsilon_b^{He-K^+}$ when $\tau_b^{He-K^+} = l_b^{He-K^+}$ and its derivative should be equal to zero. From these relations, we obtained the parameters

$$\sigma_1 = 4\epsilon\sigma_{He-K^+}^{12} = 8.83e - 17\text{statcoul}^2\text{\AA}^{o11}$$

$$\sigma_2 = 4\epsilon\sigma_{He-K^+}^6 = 4.29e - 20\text{statcoul}^2\text{\AA}^{o11}$$

From these parameters, we can calculate $He - K^+ - He$ interaction energy at $l_b^{He-K^+-He} = 3.18A^o$ which is $V_{He-K^+-He} = -23.7314mev$. This should be the binding energy of this system if there are no three-body effects. But the real binding energy $\epsilon_b^{He-K^+-He} = -24.9mev$ The difference between V_{He-K^+-He} and $\epsilon_b^{He-K^+-He}$ is the indirect He-He interaction through polarizable K^+ ion which is V_2 . Thus we obtain

$$V_2 = \epsilon_b^{He-K^+-He} - V_{He-K^+-He} \simeq -1.17mev \simeq -14K$$

Combining the direct and indirect He-He interactions, we get the total nearest neighbor interaction energy

$$V = V_1 + V_2 \simeq -23K$$

The interaction between He-He atoms in real K-L zeolite is much more complicated. The two contributions we have estimated are perhaps the most significant ones.

Bibliography

- [1] J. M. Drake and J. Klafter, *Phys. Today*, **May**, 46 (1990).
- [2] J. Kärger, G. Seiffert and F. Stallmach, *J. Magnetic Resonance.*, **A102**, 327 (1993).
- [3] H. Pfeifer and J. Kärger, *J. Mol. Liq.* **54**, 253 (1992).
- [4] G. B. Woods, A. Z. Panagiotopoulos and J. S. Rowlinson, *Molecular Physics*, **63**(1), 49 (1988).
- [5] P. T. Callaghan, A. Coy, D. MacGowan and K. J. Packer, *J. Mol. Liq.*, **54**, 239 (1992).
- [6] P. A. Politowicz, *J. Phys. Chem.*, **92**, 6078 (1988).
- [7] P. A. Politowicz, L. B. S. Leung and J. Kozak, *J. Phys. Chem.*, **93**, 923 (1989).
- [8] L. M. Schwartz and D. L. Johnson, *Phys. Rev. B*, **30**, 4302 (1984).
- [9] J. H. Page, J. Liu, B. Abeles, H. W. Deckman and D. A. Weitz, *Phys. Rev. Lett.*, **71**, 1216 (1993).
- [10] B. Abeles, L.F. Chen, J. W. Johnson and J. M. Drake, *Mat. Res. Soc. Extended Abstract (EA-22)*, 83 (1990).

- [11] R. Blumenfeld and D. J. Bergman, *J. Appl. Phys.*, **62**(5), 1616 (1987).
- [12] G. B. Woods and J. S. Rowlinson, *J. Chem. Soc.*, **85**(6), 765 (1989).
- [13] J. M. Shin, K. T. No, and M. S. Jhon, *J. Phys. Chem.*, **92**, 4533 (1988).
- [14] S. D. Pickett, A. K. Nowak, J. M. Thomas, B. K. Peterson, J. F. P. Swift, A. K. Cheetham, C. J. J. den Ouden, B. Smit and M. F. M. Post, *J. Phys. Chem.*, **94**, 1233 (1990).
- [15] S. D. Pickett, A. K. Nowak, J. M. Thomas and A. K. Cheetham, *Zeolite*, **V9**, 123 (1989).
- [16] J. B. Nicholas, F. R. Trouw, J. E. Mertz, L. E. Iton, and A. J. Hopfinger, *J. Phys. Chem.*, **97**, 4149 (1993).
- [17] A. Nakano, L. Bi, R. K. Kalia and P. Vashishta, *Phys. Rev. Lett.*, **71**, 85 (1993).
- [18] I. Bitsanis, J. J. Magda, M. Tirrell and H. T. Davis, *J. Chem. Phys.*, **87**(3), 1733 (1987).
- [19] A. Loriso, M. J. Bojan, A. Vernov and W. A. Steele, *J. Phys. Chem.*, **97**, (1993).
- [20] M. Sahimi, *J. Chem. Phys.*, **92**(8), 5107 (1990).
- [21] W. R. Hammond, B. Y. Chen, Aniket Bhattacharya, and S. D. Mahanti,
To be published.
- [22] A. V. Vernov and W. A. Steele, *J. Phys. Chem.*, **97**, (1993).
- [23] B. P. Feuston and J. B. Higgins, *J. Phys. Chem.*, **98**, 4459 (1994).

- [24] J. Kärger and D. M. Ruthven, *Diffusion in Zeolites and other Microporous Solids*, Wiley, New York, 1993.
- [25] D. W. Breck, *Zeolite Molecular Sieves* (Wiley, New York, 1974), p.636
- [26] Carbon black.
- [27] H. Seong, S. Sen, T. Çağın and S. D. Mahanti, *Phys. Rev. B*, **45**, 8841(1992); *Graphite Intercalation Compounds, V1, Structure and Dynamics*, ed. by H. Zabel and S. A. Solin, Springer Series in Topics in Current Physics, Springer (1990).
- [28] Ping Zhou, Ph.D. Thesis, M.S.U., 1991. Ping Zhou and S. A. Solin (unpublished).
- [29] P. C. Ball and R. Evans, *Langmuir* **5**, 714 (1989).
- [30] R. Evans, *J. Phys. Condensed Matter* **2**, 8989 (1990).
- [31] R. Jullien and R. Botet, *Aggregation and Fractal Aggregates*, World Scientific, Singapore, 1987.
- [32] C. R. A. Catlow, in *Modelling of Structure and Reactivity in Zeolites*, p1, 1992.
- [33] R. M. Barrer, *Zeolites and Clay Minerals as Sorbents and Molecular Sieves*, 1978. T. J. Pinnavaia, *Science*, **220**, 365 (1983).
- [34] R. M. Barrer and H. Villiger, *Zeitschrift für Krystallographies*, Bd, **128**, 352 (1969).

- [35] P. A. Wright, J. M. Thomas, A. K. Cheetham, and A. K. Nowak, *Nature*, **318**, **611** (1985).
- [36] *International Tables for X-ray Crystallography*, Vol 1, The Kynoch Press, Birmingham, England, 1952.
- [37] C. J. B. Mott, *Catalysis Today*, **2**, 199 (1988).
- [38] H. Kim, Ph.D Thesis, Michigan State University (1991)
- [39] M. W. Long, in *Series on Advances in Statistical Mechanics-V7: The Hubbard Model Recent Results* (ed. by M. Rasetti, World Scientific, 1991).
- [40] E. Fradkin, in *Field Theories of condensed Matter Systems* (Addison-Wesley, Redwood, CA, 1991), Chap. 2.
- [41] D. Vollhardt, *Rev. of Mod. Phys.* **56**, 99 (1984).
- [42] M. P. A. Fisher, P. B. Weichman, G. Grinstein, and D. S. Fisher, *Phys. Rev. B* **40**, 546 (1989).
- [43] B. Y. Chen, S. D. Mahanti and M. Yussouff, *Phys. Rev. B* **51**, 5800 (1995).
- [44] B. Y. Chen, S.D. Mahanti and M. Yussouff, *Phys. Rev. Lett.*, **75**, 473 (1995).
- [45] B.Y. Chen, H. Kim, S. D. Mahanti, T. J. Pinnavaia and Z. X. Cai, *J. Chem. Phys.*, **100**(5), 3872 (1994).
- [46] J. G. Dash, *Films on Solid Surfaces* (Academic Press, New York, 1975), Chap.8; F. J. Milford and A. D. Novaco, *Phys. Rev. A*, 1136 (1971).

- [47] J. Yuyama, *J. Low Temp. Phys.* **47**, 1 (1982);
- [48] E.Cheng, M.W.Cole, W.F.Saam, and J. Treiner, *Phys. Rev. Lett.* **67**, 1007 (1991)
- [49] E. Cheng, M. W. Cole, J. Dupont-Roc, W.F. Saam, and J. Treiner, *Rev. Mod. Phys.* **65**, 557 (1993) and references therein.
- [50] R. H. Tait and J. D. Reppy, *Phys. Rev. B* **20**, 997 (1979).
- [51] B. C. Crooker, B. Hebral, E. N. Smith, Y. Takano and J. D. Reppy, *Phys. Rev. Lett.* **51**, 666 (1983).
- [52] N. Wada, T. Ito, and T. Watanabe, *J. Phys. Soc. Japan* **53**, 913 (1984).
- [53] N. Wada, H. Kato, H. Shirataki, S. Takayanagi, T. Ito and T. Watanabe, in proceedings of the 17th International Conference on Low Temp. Phys., U. Eckern, A. Schmid, W. Weber and H. Wühl, eds. (North Holland, Amsterdam, 1984), p. 521.
- [54] H. Kato, N. Wada, T. Ito, S. Takayanagi and T. Watanabe, *J. Phys. Soc. Japan*, **55**, 246 (1986)
- [55] N. Wada, Y. Yamamoto, H. Kato, T. Ito and T. Watanabe, in *New Developments in Zeolite Science and Technology*, Y. Murakami, A. Iijima and J. W. Ward, eds. (Kohdansha, Tokyo, 1986), p. 625.
- [56] N. Wada, K. Ishioh, and T. Watanabe, *J. Phys. Soc. Japan*, **61**, 931 (1992).

- [57] N. Wada, H. Kato, S. Sato, S. Takayanagi, T. Ito and T. Watanabe, in proceedings the 17th International Conference on Low Temp. Phys., U. Eckern a. Schmid, W. Weber and H. W ühl, eds. (North Holland, Amsterdam, 1984), p. 523.
- [58] H. Kato, K. Ishioh, N. Wada, T. Ito and T. Watanabe, J. of Low Temp. Phys. **V68**, 321 (1987).
- [59] H. Deguchi, K. Konishi, K. Takeda and N. Uryu, Physica B, **165&166**, 571 (1990).
- [60] K. Konishi, H. Deguchi and K. Takeda, J. Phys.: Condens. Matter **5**, 1619 (1993).
- [61] C. P. Chen, S. Mehta, L. P. Fu, A. Petrou, F. M. Gasparini, and A. Hebard, Phys. Rev. Lett., **71**, 739 (1993).
- [62] V. C. Farmer, M. J. Adams, A. R. Fraser and F. Palmieri, Clay Minerals, **18**, 459 (1983).
- [63] M.J.Wagner, R.H.Huang, J.L.Eglin, and J.L.Dye, Nature **368**, 726 (1994) and references therein.
- [64] J. L. Dye, M. J. Wagner, G. Overney, R. H. Huang, T. Nagy, and D. Tománek, to be published in J. American Chem. Society.
- [65] C. S. Lent and M. Leng, Appl. Phys. Lett. **58**, 1650 (1991).
- [66] S. E. Koonin, *Computational Physics*, 1986.
- [67] S. B. Kim and M. H. W. Chan, Phys. Rev. Lett. **71**, 2268 (1993).

- [68] A. D. Novaco and F. J. Milford, *Phys. Rev. A* **5**, 783 (1972).
- [69] I. Doi, *J. Phys. Soc. Jpn.* **58**, 1312 (1989).
- [70] T. Minoguchi and Y. Nagaoka, *Prog. Theor. Phys.* **78**, 552 (1987).
- [71] M. P. A. Fisher, P. B. Weichman, G. Grinstein, and D. S. Fisher, *Phys. Rev. B* **40**, 546 (1989).
- [72] D. K. K. Lee and J. M. F. Gunn, *Phys. Rev. B* **46**, 301 (1992).
- [73] Z. Q. Zhang and P. Sheng, *Phys. Rev. E* **49**, 3050 (1994).
- [74] G. Batrouni, R. T. Scalettar, and G. T. Zimanyi, *Phys. Rev. Lett.* **65**, 1765 (1990).
- [75] F. D. M. Haldane, *Phys. Rev. Lett.* **47**, 1840 (1981).
- [76] J. Voit, *J. Phys. (Cond. Matt.)*, **V5**, 8305 (1993).
- [77] For an open chain, when $U \rightarrow \infty$, two particles, whether bosons or fermions, cannot interchange their positions. Therefore they have identical symmetry properties. For closed rings, when n is odd, an even number of permutations is needed to rearrange the many particle states, and as a result bosons and fermions behave identically. For even n , an odd number of permutations is needed instead, leading to the differences between bosons and fermions.
- [78] M. Ogata and H. Shiba, *Phys. Rev. B* **41**, 2326 (1990).
- [79] D. M. Dennison, *Proc. R. Soc. London Sect. A* **115**, 483 (1927).

- [80] R. K. Pathria, *Statistical Mechanics* (Pergamon Press, New York, 1978), p. 167.
- [81] C. Kittel, *Introduction to Solid State Physics*, 5th Edition, John Wiley and Sons, Inc, p454.
- [82] T. A. Kaplan, S. D. Mahanti, and W. M. Hartmann, *Phys. Rev. Lett.* **27**, 1796(1971).
- [83] P. W. Anderson, B. I. Halperin, and C. M. Varma, *Philos. Mag.* **25**, 1 (1972).
- [84] W. A. Phillips, *J. Low Temp. Phys.*, **V7**, 351(1972).
- [85] N. E. Cusack, *The Physics of Structurally Disordered Matter: An Introduction*, IOP Publishing, Ltd: Bristol.
- [86] B. F. Chmelka, D. Raftery, A. V. McCormic, I. C. de Menorval, R. D. Levine, A. Pines, *Phys. Rev. Letters*, **66**, 580 (1991).
- [87] R. L. June, A. T. Bell, and D. N. Theodorou, *J. Phys. Chem.* **94**, 8232 (1990).
- [88] A. V. Vernov, W. A. Steele, and L. Abrams, *J. Phys. Chem.* **97**, 7660, (1993).
- [89] A. Loriso, M. J. Bojan, A. Vernov, and W. A. Steele, *J. Phys. Chem.* **97**, 7665, (1993).
- [90] Feng Yin Li and R. Stephen Berry, *Z. Phys. D* **26**, 394, (1993).
- [91] Feng Yin Li and R. Stephen Berry, *J. Phys. Chem.* **99**, 15557 (1995).

- [92] Feng Yin Li and R. Stephen Berry, *J. Phys. Chem.* **99**, 2459 (1995).
- [93] R. D. Etters and J. Kaelberer, *Phys. Rev. A*, **11**, 1068, (1975).
- [94] J. Kaelberer and R. D. Etters, *J. Chem. Phys.*, **66**, 3233, (1977).
- [95] R. D. Etters and J. Kaelberer, *J. Chem. Phys.*, **66**, 5112, (1977).
- [96] S. Nosé, *Molecular Phys.*, **52**, 255 (1984).
- [97] J. B. Nicholas, F. R. Trow, J. E. Mertz, L. E. Iton, and A. Hopfinger, *J. Phys. Chem.* **97**, 4149, (1993).
- [98] S. J. Gregg and K. S. W. Sing, *Adsorption, Surface Area and Porosity* (Academic, New York, 1982)
- [99] N. J. Wilkinson, M. A. Alam, J. M. Clayton, R. Evans, and S. G. Usmar, *Phys. Rev. Lett.*, **69**, 3535 (1992)
- [100] R. Zallen, *Percolation Structures and Processes*(NY, 1983)
- [101] R. E. Grim, *Clay Mineralogy*, 2nded.,(McGraw-Hill Book, 1968)
- [102] M. S. Whittingham, *Intercalation Chemistry* (Academic Press, NY 1982),p1.
- [103] Z. X. Cai, S. D. Mahanti, S. A. Solin, T. J. Pinnavaia, *Phys. Rev. B***42**, 6636 (1990)
- [104] I. D. Johnson, T. A. Werpy, T. J. Pinnavaia, *J. Am. Chem. Soc.* **110**, 8545 (1988)
- [105] H. Kim, W. Jin, et al, *Phys. Rev. Lett.*, V.**60**, 21, 2168(1988).

- [106] F. Tsvetkov and J. White, *J. Am. Chem. Soc.* **110**, 3183 (1988).
- [107] G. Reiter and S. C. Moss, *Phys. Rev. B* **33**, 7209 (1986).
- [108] Z. X. Cai, Ph.D thesis, 1991.
- [109] The measurements were carried out by putting the diffusing gas on one side of the porous film with a fixed pressure (> 95 torr) and then measuring the time in which the partial pressure on the other side of the film (which is pumped to keep the pressure at $\sim 10^{-7}$ torr) approach its saturation or steady state value.
- [110] D. Stauffer, *Introduction to Percolation Theory*, 1985
- [111] L. M. Schwartz and J. R. Banavar, *Phys. Rev. B* **39**, 11965 (1989).
- [112] Rao et.al, unpublished.

20

LIBRARY
Michigan State
University

MICHIGAN STATE UNIV. LIBRARIES



31293015812211